Manipulation of excited states in organic-inorganic hybrid perovskite optoelectronic devices

A Dissertation Presented for the

Doctor of Philosophy

Degree

The University of Tennessee, Knoxville

Jia Zhang

May 2021

Copyright © 2021 by Jia Zhang

All rights reserved.

Dedication

I dedicate this dissertation to my parents.

Acknowledgements

I would like first to express my sincere acknowledgement to my supervisor, Dr. Bin Hu, for his endless support, guidance and encouragement throughout my research project during the past three years. Especially, I am sincerely thankful for Dr. Bin Hu's knowledge in material and physical science, questions and suggestions to my studies and experiments, education to my exploration and analysis skills, which are the foundation of my doctoral research work. I would also like to devote my acknowledgements to Dr. Haixuan Xu, Dr. Mahshid Ahmadi and Dr. Ilia N Ivanov for severing as my committee members, and their valuable comments and advice help a lot for revising my dissertation.

I am also grateful to my two collaborators Dr. Wanyi Nie and Hsinhan Tsai at Los Alamos National Lab for providing helpful characteristics and analysis with Grazing incidence wide angle X-ray scattering results.

I am particularly thankful to four former colleagues, Dr. Ting Wu, Dr. Jiajun Qin, Dr. Hengxing Xu and Dr. Jeremy Tisdale for sharing their expertise in perovskite device physics and material processing since the beginning of my dissertation work. I would also like to thank all the current colleagues, Miaosheng Wang, Xixiang Zhu, Yixuan Dou, Yongtao Liu and Bogdan Dryzhakov for their great support and friendship.

Finally, I would like to particularly devote my deepest gratitude to my parents, Xianfeng Zhang and Xiaohang Zhang, my younger brother Kun Zhang for their unlimited understanding and support.

Abstract

In recent years, a huge success on photovoltaic and light emitting has been achieved in the field of organic-inorganic hybrid perovskites owing to the superior optoelectronic properties of excited states. Regulating the primary excited states is the foundation of developing multi-functional optoelectronics, including the light-emitting, photovoltaic and lasing actions. By revisiting the photophysical processes of excited states, some new strategies are suggested to further pushing the efficiency of perovskites forward. This thesis focuses on the manipulation of excited states through combining optoelectronic devices, from excited states generation to excited charge carrier transport.

Chapter 1 presents a basic introduction to excited states in semiconductors and some optoelectronic applications of organic inorganic hybrid perovskites. Chapter 2 demonstrates charge-transfer excitons in 2D perovskite heterostructures. In this chapter, we first discover charge-transfer excitons in 2D perovskite heterostructure (PEA_2PbI_4/PEA_2SnI_4), which opens up the potential applications in perovskite LEDs and photodetectors. Chapter 3 reveals doping enhanced orbit-orbit interaction in Sn based perovskites and Chapter 4 introduces long-order orbital interaction through slow hot-carrier cooling. In these two chapters, we explore the possible strategies to increase the population of dark states through orbit-orbit interaction toward highly efficient quasi-2D perovskite solar cells and lead-free perovskite solar cells. Chapter 5 proposes a new strategy (uniform permutation of 2D nanoplates) in quasi-2D perovskite films toward efficient charge collection and Chapter 6 realizes AC electroluminescence in quasi-2D perovskite LEDs. In these two chapters, we propose a new strategy to facilitate bipolar carrier transport in quasi-2D perovskite films toward world record high fill factor in quasi-2D perovskite solar cells and efficient alternating current driven LED. Chapter 7 summarizes the entire studies in this dissertation.

Table of Contents

Chapter 1 Introduction 1

1.1 Excited states in organic-inorganic hybrid perovskites 2

1.1.1 Types of excited states 2

1.1.2 Conversion between bright states and dark states 5

1.1.3 Transport of excited charge carriers 12

1.1.4 Excited states recombination 13

1.2 Perovskite optoelectronic devices 15

1.2.1 Solar cells 15

1.2.2 Light emitting diodes 19

1.2.3 Photodetectors 22

1.3 Dissertation Outline 23

Chapter 2 Establishing charge-transfer excitons in 2D perovskite heterostructures 24

2.1 Abstract 25

2.2 Introduction 25

2.3 Materials and Methods 27

2.3.1 Materials synthesis and device fabrication 27

2.3.2 Fabrications of LED and photodetector. 27

2.3.3 Mechanically preparing heterostructures. 29

2.3.4 Characterizations and measurements 29

2.4 Results and discussion 30

2.4.1 CTEs in heterostructured 2D perovskite thin film 30

2.4.2 CTEs in double-layered 2D perovskite heterostructures 34

2.4.3 Dynamic analysis of CTEs formation. 36

2.4.4 Heterostructured 2D perovskite photodetectors and LEDs. 38
2.5 Summary 40
Chapter 3 Doping Induced Orbit-orbit Interaction between Excitons while Enhancing Photovoltaic Performance in Tin Perovskite Solar Cells 42
3.1 Abstract 43
3.2 Introduction 43
3.3 Materials and Methods 45
3.3.1 Materials and Device fabrication 45
3.3.2 Characterizations and Measurements 45
3.4 Results and Discussion 46
3.5 Summary 59
Chapter 4 Slow hot-carrier cooling and long-order orbital interaction enabled by uniformly arranging different-n-value nanoplates in quasi-2D perovskites 61
4.1 Abstract 62
4.2 Introduction 62
4.3 Materials and Methods 63
4.3.1 Materials Processing and Device Fabrication 63
4.3.2 Characterizations and Measurements 64
4.4 Results and Discussion 64
4.5 Summary 71
Chapter 5 Uniform permutation of quasi-2D perovskites by vacuum poling for efficient, high-fill-factor solar cells 74
5.1 Abstract 75
5.2 Introduction 75
5.3 Materials and Methods 76

5.3.1 Materials Processing and Device Fabrication 76
5.3.2 Characterizations and Measurements 77
5.4 Results and Discussion 78
5.5 Summary 87
Chapter 6 Enabling AC electroluminescence in quasi-2D perovskites by uniformly arranging different-n-value nanoplates to allow bidirectional charge transport 89
6.1 Abstract 90
6.2 Introduction 90
6.3 Materials and Methods 91
6.3.1 Materials Processing and Device Fabrication 91
6.3.2 Characterizations and measurements 92
6.4 Results and Discussion 93
6.5 Summary 100
Chapter 7 Conclusion 101
References……...104
Appendix……126
List of Publications 127
Vita……..129

List of Figures

Figure 1- 1 Schematic diagram of organic inorganic hybrid perovskite with formula of ABX_3... 3

Figure 1- 2 Schematic diagram of threefold degenerate triplet states and a singlet state. 7

Figure 1- 3 Schematic diagram to show the orbit-orbit interaction between excitons upon switching the photoexcitation between linear and circular polarizations. 9

Figure 1- 4 SOC induced conversion between triplets ***J***=1 (J_z= +1, 0, -1, allowed to recombine) and singlets ***J***=0 (J_z= 0, forbidden to recombine), which is reflected by the magnetic field effects. 11

Figure 1- 5 Schematic layered structures of 2D perovskite nanoplates with different n values (n=1, 3, 5 and infinite). 14

Figure 1- 6 (a) Schematic device structure of a solar cell. (b) The energy level diagram of a solar cell and the arrows indicate the transportation of photogenerated carriers. (c) Current-voltage curve for a solar cell at one sun condition. MMP is maximum power point. 16

Figure 1- 7 The efficiency evolution of perovskite solar cells. Data is replotted from ref. [55] 18

Figure 1- 8 Energy levels for 2D perovskite with different n values, and the arrows indicates the direction of charge transfer between different-n-value nanoplates. Figure is adapted from ref. . 20

Figure 1- 9 (a) Schematic device structure of a light emitting diode (LED). (b) The energy level diagram of a LED device and the arrows indicate the transportation of injected charge carriers. 21

Figure 2- 1 Schematic diagram of perovskite film fabrication procedure through one-step spin-coating method. 28

Figure 2-2 Optical characteristics of CTEs formation in 2D perovskite heterostructures. (a) Absorption and PL spectra are shown for 2D perovskite heterostructured $[(PEA_2PbI_4)_{0.999}:(PEA_2SnI_4)_{0.001}]$ film. The absorption spectrum indicates that the bandgap is governed by the host (PEA_2PbI_4) component in the heterostructures. The PL spectrum is dominated by a broad emission peaked at 669 nm with a spectral shoulder at 614 nm from the guest (PEA_2SnI_4) and the intrinsic emission (peaked at 531 nm) from the host (PEA_2PbI_4). (b)

Normalized PL spectra to show broad light emission peaked at 669 nm for heterostructured [$(PEA_2PbI_4)_{1-x}$:$(PEA_2SnI_4)_x$] films. (c) PL spectrum is shown for 2D perovskite heterostructured [$(PEA_2SnI_4)_{0.999}$:$(PEA_2PbI_4)_{0.001}$] film after switching host and guest components. The broad emission is observed with the peak position at 697 nm, in addition to intrinsic emission (peaked at 524 nm and 627 nm) from host (PEA_2PbI_4) and guest (PEA_2SnI_4) components. The PL spectra for pristine PEA_2PbI_4 and PEA_2SnI_4 films are also shown as reference. (d) Schematic diagram illustrates the formation of CTEs at the interfaces between PEA_2PbI_4 and PEA_2SnI_4 components in 2D perovskite heterostructures [$(PEA_2PbI_4)_{1-x}$:$(PEA_2SnI_4)_x$]..... 31

Figure 2- 3 PL characteristics for 2D perovskite heterostructured [$(PEA_2PbI_4)_{0.999}$:$(PEA_2SnI_4)_{0.001}$] film. (a) Normalized PL spectra at different excitation intensities ranging from 5 $\mu W/cm^2$ to 94 mW/cm^2. (b) PL-excitation intensity dependences for broad emission (peaked at 669 nm) as compared to intrinsic emission (524 nm) from host (PEA_2PbI_4). (c) PL lifetime results for broad emission (peaked at 669 nm) in 2D perovskite heterostructures and intrinsic emission (peaked at 524 nm, and 621 nm) from host (PEA_2PbI_4) and guest (PEA_2SnI_4)..... 33

Figure 2- 4 Hand-finger pressing method to confirm CTEs formation in 2D perovskite heterostructures. (a) Schematic diagram illustrates that show PEA_2SnI_4 film is shearing-away on PEA_2PbI_4 film surface to prepare double-layered [PEA_2PbI_4/PEA_2SnI_4] heterointerfaces. (b) PL spectrum was measured for double-layered [PEA_2PbI_4/PEA_2SnI_4] heterointerfaces. The broad emission is shown as an extended spectral tail in addition to intrinsic emission (530 nm and 637.5 nm) from PEA_2PbI_4 and PEA_2SnI_4 components. The dashed lines are shown for three spectral components from PEA_2PbI_4 component, PEA_2SnI_4 component, and [PEA_2PbI_4/PEA_2SnI_4] heterointerfaces..... 35

Figure 2- 5 Transient absorption (TA) characteristics for 2D perovskite heterostructures and PEA_2PbI_4. (a) TA spectra for 2D perovskite heterostructured [$(PEA_2PbI_4)_{0.95}$:$(PEA_2SnI_4)_{0.05}$] film. (b) TA spectra for pristine PEA_2PbI_4 film. (c) TA dynamics plotted for band-to-band transition (513.8 nm), surface excitons (537.5 nm) and broad emission (657.3 nm) in 2D perovskite heterostructures. 37

Figure 2- 6 Device performance of photodetectors and LEDs for 2D perovskite heterostructures. (a) The ON-OFF behaviors of heterostructured 2D perovskite [$(PEA_2PbI_4)_{0.95}$:$(PEA_2SnI_4)_{0.05}$]

photodetector (red) as compared to pure PEA_2PbI_4 (black) and PEA_2SnI_4 (blue) devices when exciting at 640 nm (1000 mW/cm^2). (b) Absorption spectra of two films. (c) EL spectrum containing broad CTEs emission and host emission. (d) Current density-voltage-EL curve of doped device. The device structure is shown as the inset. 39

Figure 3- 1 Orbit-orbit interaction in $FASnI_2Br$ perovskites. (a) Schematic diagram to show the orbit-orbit interaction between excitons upon switching the photoexcitation between linear and circular polarizations (b) Photocurrent change of devices without and with SnF_2 doping by switching between linear and circular polarized photoexcitations (405 nm) at identical intensity (148 mW/cm^2). 47

Figure 3- 2 Normalized magneto-photocurrents curves. The internal magnetic parameter B_0 was derived from Lorentizan function in Sn based perovskite solar cells with or without doping. 50

Figure 3- 3 Current-voltage characteristics measured under 1 sun condition $FASnI_2Br$ perovskite solar cells ([ITO/PEDOT:PSS/$FASnI_2Br$/$PC_{61}BM$/PEI/Ag]) with different doping concentration of SnF_2. 51

Figure 3- 4 Photovoltaic performance of Sn perovskites with and without SnF_2 doping. (a) Current-voltage characteristics measured under 1 sun condition for Sn solar cell [ITO/PEDOT:PSS/$FASnI_2Br$/$PC_{61}BM$/PEI/Ag]. (b) EQE spectra. 53

Figure 3- 5 Reduced defect density through SnF_2 doping. (a) Density of trap states (tDOS) deduced from C-f and C-V data at room temperature for doped and undoped devices. (b) Time-resolved photoluminescence characteristics of $FASnI_2Br$ films with and without SnF_2 doping and the solid lines are obtained by fitting the decay traces with a bi-exponential law. The fitted data are shown in **Table 3-3**. 56

Figure 3- 6 Schematic drawing to show the doping effects on orbit-orbit interaction. 58

Figure 4- 1 Schematic diagram and optical characteristics of quasi-2D perovskite solar cells with uniformly dispersed nanoplates. (a) Spatial arrangement of uniform dispersed nanoplates. (b) Current-voltage characteristics for device with uniformly distributed nanoplates. 65

Figure 4- 2 Transient absorption (TA) spectra for quasi-2D perovskite ($PEA_2MA_4Pb_5I_{16}$) films with ordered and uniform distributed nanoplates. (a) TA spectra with delay time between 0.5-10 ps for films with uniformly distributed nanoplates. (b) TA spectra with delay time between 10-

1000 ps for films with uniformly distributed nanoplates. (c) Dynamical changes of photoexcited carrier energy as a function of delay time for films of perovskite only (black), perovskite/PTAA (red) and perovskite/$PC_{61}BM$ (blue). 67

Figure 4- 3 Polarons enable slow cooling with lower transport barriers due to spatially extended wavefunctions within local lattice as compared to electrons with fast cooling and higher transport barriers due to localized wavefunctions. 69

Figure 4- 4 Photocurrent change (ΔJsc) measured by switching photoexcitation from linear to circular polarization and principle diagrams to show long-order orbital interaction. (a) -ΔJsc observed from device prepared with uniformly distributed nanoplates to indicate long-order orbit-orbit Coulomb interaction. (b) Short-order orbital interactions between magnetic dipoles under circular photoexcitation. (c) Long-order orbital interactions between polarizations under linear photoexcitation. 70

Figure 4- 5 J-V curves at different light illumination intensities from 1 sun to 0.1 Sun conditions for devices with uniform dispersion. 72

Figure 5- 1 Schematic diagram of film fabrication procedure and tape peeling-based photoluminescence (PL) characterizations of quasi-2D perovskite films prepared with and without vacuum poling treatment. (a) Schematic diagram to show processing methods with and without vacuum poling treatment to prepare quasi-2D perovskite films. (b) Schematic drawing to illustrate our tape-peeling method, to mechanically detach monolayers from quasi-2D perovskite films, while subsequently measuring PL spectra. (c) PL spectra measured before and after peeling for <n>=5 quasi-2D perovskite films prepared with and without vacuum poling treatment. (d), (e) Schematic diagram to indicate uniform (d) and ordered (e) formation of different-n-value nanoplates in quasi-2D perovskite films prepared with and without vacuum poling treatment. 79

Figure 5- 2 Absorption and photoluminescence (PL) results of films (<n>=5) right after different vacuum-poling-treated times before thermal annealing. (a) Absorption evolution induced by vacuum poling treatment and thermal annealing. With nucleation prior to full crystallization, the absorbance remains very low before annealing. After annealing, absorption become increased, showing full crystallization. (b) Normalized PL spectra of films after different vacuum-poling-treated times. There is a red shift as vacuum-poling-treatment time increases, indicating the

further formation of large-n-value nanoplates. (c) Spectral width (FWHM) of films as a function of vacuum-poling-treated time. All the vacuum-poling-treated films without annealing show broader spectral width than annealed film due to inhomogeneous disorder from insufficient crystallization. (d) Transient PL results of perovskite films before (black curve) and after (red curve) annealing. After fully crystallization, the annealed film (red recurve) shows much longer lifetime. 80

Figure 5- 3 Transient absorption (TA) spectra at different delay times (-10 ps, 1 ps, 2ps, 5ps, 10 ps, 20 ps, 50 ps, 100 ps) and dynamics of quasi-2D perovskite (<n>=5) films when exciting through top (upper figures of a and b) and bottom (down figures of a and b). The wavelengths at 534 nm, 567 nm, 609 nm and 724 nm (750 nm) Correspond to Signals from Small-n-value to Largest-n-value Nanoplates. (a) With vacuum poling treatment. TA spectra are similar when exciting through top (upper figure) and bottom (down figure), indicating the uniform distribution of nanoplates. (b) Without vacuum poling treatment. TA spectra are quite different when exciting through top (upper figure) and bottom (down figure), indicating order dispersion of nanoplates. (c) <n>=5 film with vacuum poling treatment shows positive transient absorption signals at small-n-value nanoplates and fast (within 10 ps) increased negative signal at 724 nm (corresponding to largest-n-value nanoplates). (d) <n>=5 film without vacuum poling treatment shows both positive (at 534 nm) and negative (at 567 nm and 609 nm) transient absorption signals at small-n-value nanoplates and slow (~ 600 ps) negative signal at 750 nm (corresponding to largest-n-value nanoplates). 82

Figure 5- 4 PL Characterizations and dynamics for quasi-2D perovskite films prepared with and without vacuum poling treatment. (a), (b) PL spectra for quasi-2D perovskite films prepared with and without vacuum poling treatment. (c) PL-excitation intensity dependences for emission peaks ≤ 710 nm related to small n-value nanoplates prepared with and without vacuum poling treatment. (d) PL-excitation intensity dependences (at 750 nm) for largest n-value nanoplates prepared with and without vacuum poling treatment. (e), (f) PL dynamics for quasi-2D perovskite films prepared with and without vacuum poling treatment. Sample structure: ITO/PEDOT:PSS/Perovskite. Excitation: 346 nm pulse laser (pulse width of 290 fs) with Intensity of 5 μW. 84

Figure 5- 5 Characterizations and schematic diagram of quasi-2D perovskite solar cells prepared with/without vacuum poling treatment. (a) I-V characteristics measured under 1 Sun illumination in quasi-2D perovskite solar cells prepared with vacuum poling treatment (PTAA used as hole transport layer (HTL)). (b) Photovoltaic performance (FF and PCE) of our device as compared with published PEA^+ and BA^+ based quasi-2D perovskite solar cells. Our vacuum poling treatment leads to extremely high FF and PCE. (c) Device stability test of quasi-2D perovskite device prepared with vacuum poling treatment (HTL: PTAA) under various conditions. Upper figure: operational stability under continuous one-sun illumination; Middle figure: thermal stability at 80 ^oC; Down figure: Over half a year long term stability in glovebox. (d) Statistics data of photovoltaic performance of quasi-2D perovskite solar cells with three different designs: without vacuum poling on PEDOT:PSS, with vacuum poling on PEDOT:PSS and with vacuum poling on PTAA. (e) Schematic diagram to show isotropic carrier extraction from small-n-value nanoplates directly to largest-n-value nanoplates functioning as transport high-way (shown in brown color) under uniform dispersion of different-n-value nanoplates. (f) Schematic diagram to show less efficient and prolonged carrier extraction length from n=1 to n=2, n=3, n=4, n=5 nanoplates through cascade process under ordered dispersion of different-n-value nanoplates. Blue and green area: small-n-value nanoplates, yellow and orange area: medium-n-value nanoplates, brown area: largest-n-value nanoplates. 86

Figure 6- 1 Quasi-2D perovskite LEDs towards realizing both forward and reverse EL. (a) Quasi-2D perovskite LEDs based on device architecture of ITO/PEI/PEDOT:PSS/$PEA_2MA_{n-1}Pb_nI_{3n+1}$/P3HT/PEI/Ag. (b) GIWAXS map for uniformly dispersed quasi-2D perovskite film of <n>=5. (c) TA spectra for uniformly dispersed film of <n>=5 at different delay times with feature peaks corresponding to different-n-value nanoplates marked with dashed black lines: 530 nm (n=1), 564.6 nm (n=2), 603.8 nm (n=3), 639.3 nm (n =4), 668.8 nm and 726.7 nm (n ≥ 5). (d) PL spectra for uniformly dispersed film of <n>=5 (with 405 nm laser excitation at power intensity of 68 mW/cm^2). Feature peaks corresponding to different-n-value nanoplates are observed: 527 nm (n=1), 568.8 nm (n=2), 613.7 (n=3), 645 (n=4) and 744.1 nm (n ≥ 5). (e) TA spectra of uniformly dispersed film of <n>=5 at delay time from 0 to 10 ps. 94

Figure 6- 2 Band diagram to enable AC EL in quasi-2D perovskite LEDs with uniform dispersion of different-n-value nanoplates. (a) Before contact. (b) Forward bias. (c) Reverse bias. 96

Figure 6- 3 EL Characteristics in quasi-2D perovskite LEDs under forward and reverse biases. (a) Current-voltage-EL characteristics. (b) EL spectra under forward (+1.8 V) and reverse (-1.8 V) biases. Dashed line: PL spectrum. Inset: photograph of device operated under -1.8 V to show strong EL. (c) EQE characteristics at forward and reverse injection currents. (d) Operational stability is shown with T_{50} = 11 hours for AC bias (+2 V/-2 V at 50 Hz, red curve) and T_{50} = 3.9 hours for DC bias (+2 V at 50 Hz, blue curve). 98

Figure 6- 4 EL profile of quasi-2D perovskite LEDs under forward (4.5V) and reverse (-3.5V) square-wave biases at different frequencies. (a) f = 1 Hz. (b) f = 20 Hz. (c) f = 50 Hz. (d) f = 100 Hz. 99

Chapter 1 Introduction

1.1 Excited states in organic-inorganic hybrid perovskites

An excited state is a quantum state in which the energy of the system is higher than that of the ground state. It can be generated through optical excitation, electrical injection and thermal activation. In view of semiconductor materials, the optoelectronic behaviors of excited states are attributed to the behaviors of excited charge carriers and electron-hole pairs. Here, excited charge carriers can lead to electrical current and the recombination of electron-hole pairs can lead to luminescence. Therefore, regulating the primary excited states is the foundation of developing multi-functional optoelectronics, including the light-emitting, photovoltaic and lasing actions in both organic and inorganic semiconductors.

The behaviors of excited states are determined by various optoelectronic properties of the material, such as absorption coefficient, exciton binding energy, carrier lifetime and carrier mobility. These parameters are the basis in the material's evaluation for potential optoelectronic applications. Among the various materials toward advanced optoelectronic devices, the organic inorganic hybrid perovskites have exhibited great advantages including tunable bandgap from 1.2 to over 3 eV [1-4], adjustable exciton binding energy [5,6], long carrier diffusion length over 1 μm [7,8], large light absorption coefficient ~10^5 cm^{-1} [9,10]. To note that, organic inorganic hybrid perovskites refer to a large family of crystalline materials with structures similar to that of the natural mineral calcium titanate, which was discovered by Gustav Rose in 1839 and named after Russian mineralogist Lev Perovski. As shown in **Figure 1-1**, the organic-inorganic hybrid three-dimensional (3D) perovskites can be described with a formula of ABX_3 [11], where A is a monovalent cation, B is a divalent metal cation, and X is a halogen anion that bonds with metal cations, forming corner-sharing $[BX_6]^{4-}$ octahedra cavities embedding the A cations. Through compositional engineering, low-dimensional perovskites [12, 13] are accessible, which largely broadens the superior optoelectronic properties and results in interesting phenomena regarding excited states such as categories, conversion, transport and recombination.

1.1.1 Types of excited states

The excited states in semiconductors can be generated in various forms including bound electron-hole pair (exciton), charge transfer state, exciplex and polaron pair. In semiconductors, light absorption or electrically injection can excite the ground state electron in the valance band

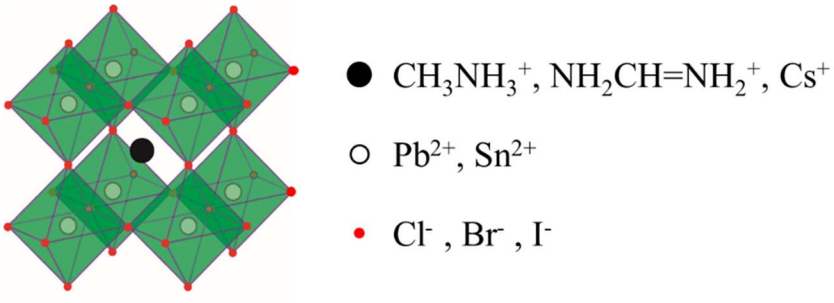


Figure 1- 1 Schematic diagram of organic inorganic hybrid perovskite with formula of ABX_3.

maximum (VBM) or highest occupied molecular orbital (HOMO) into a high energy state in conduction band minimum (CBM) or lowest unoccupied molecular orbital (LUMO), then a hole is left in the VBM or HOMO, resulting in a Coulomb-bound electron-hole pair (exciton). According to their binding energy and radius, excitons can be divided into two types: Wannier-Mott excitons and Frenkel excitons. Wannier-Mott excitons has a typical binding energy on the order of 0.01 V and a Bohr radius larger than the lattice spacing, thus they are known as large excitons of loosely bound electron-hole pairs, which usually form in semiconductors with large dielectric constants. The weakly bound Wannier-Mott excitons can easily dissociate into excited charge carriers for conduction. Whereas, Frenkel exciton has a typical binding energy on the order of 0.1 to 1 eV and a Bohr radius on the order of lattice size, thus they known as highly localized excitons of tightly bound electron-hole pairs, which usually form in organic semiconductors having small dielectric constants.

Charge transfer state is formed when a charge transfer process is occurred with the consequence of forming electron-hole pairs between two adjacent structures with different electron negativities and local energies. Charge transfer state is an intermediate case between Wannier-Mott excitons and Frenkel excitons, and it can be classified as intermolecular charge transfer state when the electron and hole separately occupy two adjacent molecules, and as intramolecular charge transfer state when electron and hole occupy a single molecule. In organic solar cells, charge transfer states play essential roles as they can easily dissociate at the p-n junction toward photocurrent generation. Besides, when the charge transfer at the interface is enhanced by orbital overlap, charge transfer state can also be observed in heterojunctions between 2D perovskite (BA_2PbI_4) and organic semiconductor 1,4,5,8,9,11-hexaazatriphenylenehexacarbonitrile (HTCN) with strong electron negativity [14]. According to their ability to dissociate electron-hole pairs, the establishment of charge transfer state in perovskite: perovskite heterostructure is the vital key to explore the new opportunities of optoelectronics.

Exciplex is simply an intermolecular exciton that sits at the interface of donor: acceptor complexes. The formation of exciplex is a bimolecular process where a ground state is first electronically excited, then the excited species undergoes complex formation through Columbic attraction with another ground state molecule, leading to a partial charge transfer from the donor-based orbital to the acceptor-based orbital. The exciplex has a minimum in the potential energy

surface as compared with the exciton the bulk. Therefore, the radiative emission of exciplex has relatively lower energy or is slightly redshifted. The exciplex can also be stabilized by the surface states, leading to a prolonged lifetime comparing with the bulk exciton [15].

Owing to the less rigid nature of organic materials than inorganics, the charge carrier (electron or hole) onto certain molecular chain can deform the whole molecule, which results in a quasi-particle (carrier together with distortion of its surroundings) called a polaron. Hence, charge transport through polaron becomes more difficult due to the distortion. When an electron polaron and a hole polaron are bounded on two adjacent chains, a polaron pair can be formed with relatively weak Coulomb attraction. Usually, polaron pair can either relax to form tightly bounded state with lower energy called an exciplex or dissociate into a pair of free polarons.

1.1.2 Conversion between bright states and dark states

In organics, the total angular momentum (**J**) is equal to the spin angular momentum (**S**) as the attribution from orbital momentum (**L**) is very weak. According to the spin configuration, the excited states in organic materials can be categorized into spin singlet (**S = 0**, $m_s = 0$) and spin triplet (**S = 1**, $m_s = 1, -1, 0$), where **S** is the spin angular momentum and m_s is the z projection of spin angular momentum. With optical excitation, only spin singlet can be formed due to the spin conservation. With electrical excitation, the electrons and holes are injected with random spins, and through random capture process based on the spin statistics [16,17], the spin singlet and spin triplet are formed with a ratio of 1:3 as shown in equation (1).

$$
\begin{aligned}
e\uparrow e\downarrow + h\uparrow h\downarrow &\rightarrow \frac{1}{4}e\uparrow h\downarrow + \frac{1}{4}e\downarrow h\uparrow + \frac{1}{4}e\uparrow h\uparrow + \frac{1}{4}e\downarrow h\downarrow \\
&\rightarrow \frac{1}{4}\left(\left|e\downarrow h\uparrow\right\rangle - \left|e\uparrow h\downarrow\right\rangle\right) + \frac{1}{4}\left(\left|e\downarrow h\uparrow\right\rangle + \left|e\uparrow h\downarrow\right\rangle\right) + \frac{1}{4}\left|e\uparrow h\uparrow\right\rangle + \frac{1}{4}\left|e\downarrow h\downarrow\right\rangle \\
&\rightarrow \tfrac{1}{4}S_{m=0} + \tfrac{1}{4}T_{m=0} + \tfrac{1}{4}T_{m=1} + \tfrac{1}{4}T_{m=-1} \qquad (1)
\end{aligned}
$$

Conversely, different from organic materials, organic inorganic hybrid perovskites possess both nonnegligible orbital (***L***) and spin (***S***) angular momentums, thus the total momentum $\boldsymbol{J = L + S}$, and the total momentum J becomes the critical quantum number to describe the multiple states. For a single electron, its orbital angular momentum is $\boldsymbol{l_e = 1}$ and its spin angular momentum is $\boldsymbol{s_e}$

= 1/2, leading to a total angular momentum $\boldsymbol{j_e} = \boldsymbol{l_e} + \boldsymbol{s_e}$. The $\boldsymbol{j_e}$ can have the value of **1/2** or **3/2**, as the $\boldsymbol{j_e}$ **= 3/2** is on high energy level and out of reach, thus the total angular momentum for a single electron is $\boldsymbol{j_e}$ **= 1/2**. Similarly, the total angular momentum for a single hole is $\boldsymbol{j_h}$ **= 1/2**. In terms of total angular momentum J for an exciton in hybrid perovskite $\boldsymbol{J} = \boldsymbol{j_e} + \boldsymbol{j_h}$.

Therefore, the exciton in organic inorganic hybrid perovskite can be classified as singlet state $\boldsymbol{J} = \mathbf{0}$ **(**J_z = 0**)** and triplet state $\boldsymbol{J} = \mathbf{1}$ (J_z = -1, 1, 0), as shown in the equation (2) and (3) [18]:

Triplet $\boldsymbol{J} = \mathbf{1}$ states ($\boldsymbol{J_z}$ = -1, 0, +1)

$$|\Psi_{1,-1}\rangle = |\Downarrow\rangle_e|\downarrow\rangle_h$$

$$|\Psi_{1,0}\rangle = \frac{1}{\sqrt{2}}[|\Downarrow\rangle_e|\uparrow\rangle_h + |\Uparrow\rangle_e|\downarrow\rangle_h]$$

$$|\Psi_{1,+1}\rangle = |\Uparrow\rangle_e|\uparrow\rangle_h \quad (2)$$

Singlet $\boldsymbol{J}$**=0** state ($\boldsymbol{J_z}$= 0)

$$|\Psi_{0,0}\rangle = \frac{1}{\sqrt{2}}[|\Downarrow\rangle_e|\uparrow\rangle_h - |\Uparrow\rangle_e|\downarrow\rangle_h] \quad (3)$$

The schematic diagram of threefold degenerate triplet states and a singlet state is shown in **Figure 1-2**. Due to spin selection rule, the triplet states $\boldsymbol{J}$**=1** (J_z= +1, 0, -1) are allowed to recombine, and the singlet state $\boldsymbol{J}$**= 0** ($\boldsymbol{J_z}$= 0) is forbidden to recombine [18]. Therefore, triplets and singlets become bright and dark states, respectively. It is proven that the population between bright and dark states can be tuned through exciton-exciton interaction or spin-orbital coupling, which may cause a change on photocurrent in perovskite solar cells [19,20].

Specifically, the exciton-exciton interaction can occur through the interaction between orbital magnetic dipoles, leading to more optically generated bright states (spin-allowed to recombine) converted to dark states (spin-forbidden to recombine). Therefore, stronger exciton-exciton interaction will lead to more dark states, resulting in increased Jsc. On the other hand, the hybrid perovskites possess a strong interaction between electrical and spin polarizations to demonstrate an electrical-magnetic coupling phenomenon [21-25]. Essentially, the orbit-orbit interaction between excitons can occur through orbital magnetic dipoles or orbital polarizations, forming short-range and long-range orbit-orbit interactions between excitons [26]. Tuning the orbit-orbit interaction plays an important role in determining the conversion from bright states to dark

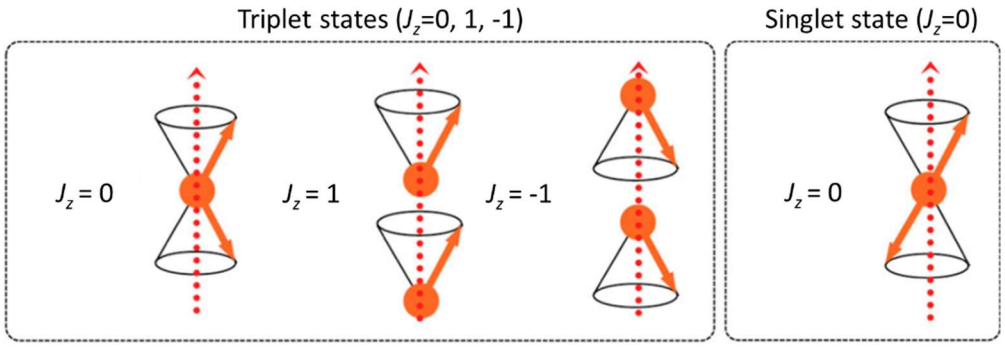


Figure 1- 2 Schematic diagram of threefold degenerate triplet states and a singlet state.

states, which is available to develop photovoltaic actions. The orbit-orbit interaction between excitons can be identified by monitoring the change of photocurrent (ΔJsc) while switching the photoexcitation between linear and circular polarizations. **Figure 1-3** shows the experimental principle to identify the orbit-orbit interaction between excitons upon switching the photoexcitation between linear and circular polarizations. Circularly and linearly polarized photoexciations generate excitons with same-directional and opposite-directional orbital magnetic dipoles, respectively. If the exciton-exciton interaction is not occurred through orbit-orbit interaction, linearly and circularly polarized photoexcitations with identical intensity would generate same photocurrents because of same density of optically generated excitons. If the exciton-exciton interaction is occurred through orbit-orbit interaction, linearly and circularly polarized photoexcitations with identical intensity can then generate different photocurrents, leading to a ΔJsc phenomenon.

We should note that the orbit-orbit interaction between excitons can occur through orbital magnetic dipoles (upward pixel in **Figure 1-3**) or orbital polarizations (downward pixel in **Figure 1-3**). When orbital magnetic dipoles dominate the orbit-orbit interaction between excitons, same-directional and opposite directional orbital magnetic dipoles generated by circularly and linearly polarized photoexcitations correspond to stronger and weaker spin-orbital coupling, respectively. Because spin-orbital coupling can serve as the underlying mechanism to flip spins to convert optically generate bright states into dark states [20,27]. Circularly/linearly polarized photoexcitation can then generate larger/smaller photocurrent, presenting a +ΔJsc when switching the photoexcitation from linear to circular polarization. When orbital polarizations dominate the orbit-orbit interaction between excitons, the parallel and antiparallel orbital polarizations can be established by the same-directional and opposite-directional orbital magnetic dipoles, causing less and more dissociation due to dipole-dipole interaction. This leads to a -ΔJsc when switching the photoexcitation from linear to circular polarization at the situation where orbital polarizations dominate the orbit-orbit interaction between excitons. Therefore, monitoring the ΔJsc provides a unique experimental method to explore the orbit-orbit interaction between excitons in hybrid perovskites. We should point out that the ΔJsc phenomenon[19,28] is established when the optically-induced orbit-orbit interaction can compete with the intrinsic orbit-orbit interaction already-existed before photoexcitation. If the optically-induced orbit-orbit interaction is much weaker than

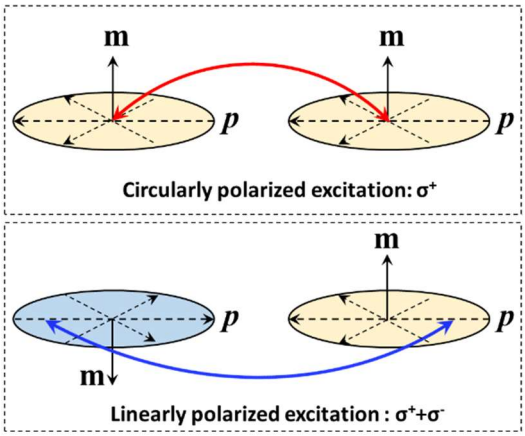


Figure 1- 3 Schematic diagram to show the orbit-orbit interaction between excitons upon switching the photoexcitation between linear and circular polarizations.

intrinsic orbit-orbit interaction, ΔJsc become negligible. Clearly, larger/smaller ΔJsc corresponds to weaker/stronger intrinsic orbit-orbit interaction.

Magnetic field effects are measured by monitoring the signal intensity such as photocurrent or photoluminescence as a function of magnetic field, leading to magneto-photocurrent or magneto-photoluminescence phenomenon. The amplitude of magnetic field effects is given by the relative change in signal amplitude:

$$MFE = \frac{S_B - S_0}{S_0} \times 100\% \quad (4)$$

where S_B and S_0 are the signal intensities with and without an applied magnetic field. Essentially, magnetic field effects are established when an external magnetic field competes intrinsic spin-orbital coupling toward controlling intersystem crossing between optically generated bright states to dark states [29], as schematically illustrated in **Figure 1-4**. If an external magnetic field is not able to compete with intrinsic spin-orbital coupling, it is difficult to change the population between bright states and dark states thus the magnetic field effects become negligible. If an external magnetic field is able to compete with intrinsic spin-orbital coupling, it is possible to change the ratio of bright states and dark states, leading to a magnetic field effect. Therefore, magnetic field effect can reflect intrinsic spin-orbital coupling characteristics. Here, the line-shape of magneto-Jsc characterized by internal magnetic parameter (B_0) can be used to estimate the intrinsic spin-orbital coupling. Large/small internal magnetic parameter provides high/low resistance for magnetic field to change the intersystem crossing. Therefore, when the intersystem crossing becomes higher/lower, it is more difficult/easier to disturb the equilibrium between optically generated bright states to dark states, broadening/narrowing the line-shape in magnetic field effect characteristics.

Regulating the conversion between dark and bright states is a vital key to directly influence the dynamics of excited states, as dark states are spin forbidden to recombine toward develop photocurrent actions whereas the bright states are spin allowed to recombine toward develop photoluminescence action. The conversion can occur between dark and bright states under the influence of exciton-exciton interaction through orbitals and spin-orbital coupling, leading to conversion-dependent optoelectronic functionalities. Therefore, understanding the exciton orbital-orbital interactions and spin-orbital coupling is a fundamentally important issue towards

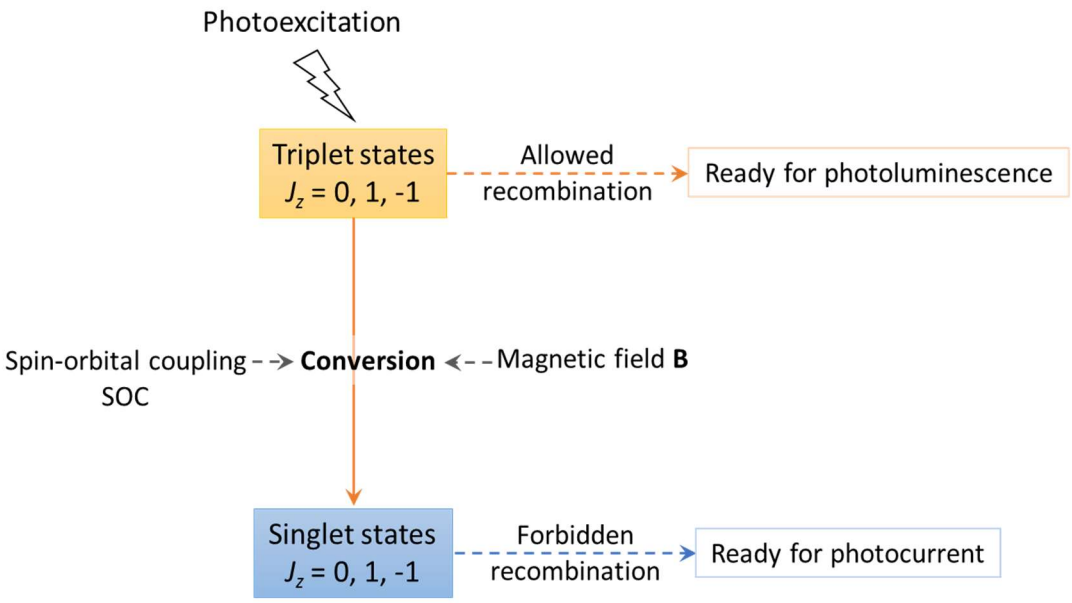


Figure 1- 4 SOC induced conversion between triplets ***J***=1 (J_z= +1, 0, -1, allowed to recombine) and singlets ***J***=0 (J_z= 0, forbidden to recombine), which is reflected by the magnetic field effects.

controlling the optoelectronic performance such as photovoltaics and light emission in perovskite devices.

1.1.3 Transport of excited charge carriers

In semiconductors, the optically generated excitons can dissociate into excited charge carriers, where the excited electrons locate at the conduction band minimum or lowest unoccupied molecular orbital and the excited holes locate at the valance band maximum or highest occupied molecular orbital. These excited charge carriers (excited electrons and holes) are free to move, resulting in electrical conducting current. Besides, the free excited carries can also be directly generated through electrical injection from the electrodes. The motion of the excited charge carriers through drift driven by electrical field and diffusion driven by the gradient of carrier concentration is the basis of transport of excited charge carriers. In solid state physics, carrier mobility is used to evaluate how quickly a charge carrier can move within the material under an electric field. The magnitude of carrier mobility is the intrinsic property of materials, which can be influenced by defects, phonons and impurities induced scatterings.

Specially, owing to the exceptional defect-tolerance nature, three dimensional (3D) organic inorganic hybrid perovskite has very high carrier mobility (5-75 $cm^2V^{-1}s^{-1}$) [30-32]. As reported, the excited charge carrier lifetime and diffusion length of 3D perovskite can be as long as 2.2 μs and 19 μm, respectively [7]. However, 3D halide perovskite has intrinsically environmental instability due to the hydroscopic nature of the organic cations and their low formation energies [33]. By incorporating hydrophobic large organic cations into 3D hybrid perovskite, much improved stability was obtained in 2D, 1D and 0D perovskites. Due to the strong quantum confinement, the transport of excited charge carrier in 0D and 1D perovskites are severely inhibited, which greatly limits the application of 0D and 1D perovskites in optoelectronics. Whereas, the 2D hybrid perovskites are naturally formed quantum well structures, where metal-halide octahedron cages are separated by bulky organic spacers forming 2D structures with the formula of $A'_2A_{n-1}M_nX_{3n+1}$, where n refers to the number of planes of the corner-sharing $[MX_6]^{4-}$ octahedral, and A, M, X refer to the monovalent cations, divalent metal cations and halide anions, respectively [12,13]. The value of n represents the metal-halide octahedron layer confined by the bulky organic spacer layers (see **Figure 1-5**), where the larger the n value is, the weaker the quantum confinement will be. As different-n-value 2D nanoplates coexist, forming a quasi-2D perovskite film, the carrier transport

is also limited by the insulating nature of the bulky organic spacers. More detailed discussion is included in Section **1.2.1**.

1.1.4 Excited states recombination

The recombination of excited states leads to two consequences: (1) radiative emission by generating a photon or (2) nonradiative recombination by releasing the energy to phonon(s). In semiconductors, the overall recombination processes can be described with the equation as follows [34,35]:

$$-\frac{dN}{dt} = AN + BN^2 + CN^3 \quad (5)$$

Here, N refers to the density of excited charge carriers, A, B and C refer to first-order, second-order and third-order recombination coefficients. In organic inorganic hybrid perovskites, the first-order term AN can be either radiative recombination (excitonic emission) or nonradiative recombination (Shockley–Read–Hall recombination). The excitonic feature is usually observed in materials with large exciton binding energy. Specifically, the Shockley–Read–Hall recombination is a trap assisted nonradiative recombination, where the deep traps within the band gap serve as the recombination centers. The second-order term BN^2 is the free electron-hole recombination (or the bimolecular recombination). The third-order term CN^3 is the Auger recombination, which is a three-particle process (ehh or eeh). Considering a system with two electrons and one hole (eeh), recombination of an electron and a hole will not lead to emission of a photon during Auger recombination. Instead, the excess energy is absorbed by the rest electron, subsequently exciting it to higher energy level.

In organic inorganic hybrid perovskites, the radiative recombination can be either from first-order excitonic emission in quantum confined systems like low dimensional perovskites and perovskite nanocrystals [36,37], and second-order bimolecular recombination in 3D perovskites [38,39]. At low carrier density, the Auger recombination is negligible owing to the relatively low Auger recombination coefficient C. Therefore, the quantum efficiency of perovskites is only related to the ratio of trap assisted nonradiative recombination. Toward efficient functional devices with low nonradiative loss, defects passivation engineering plays an important role in organic inorganic hybrid perovskites.

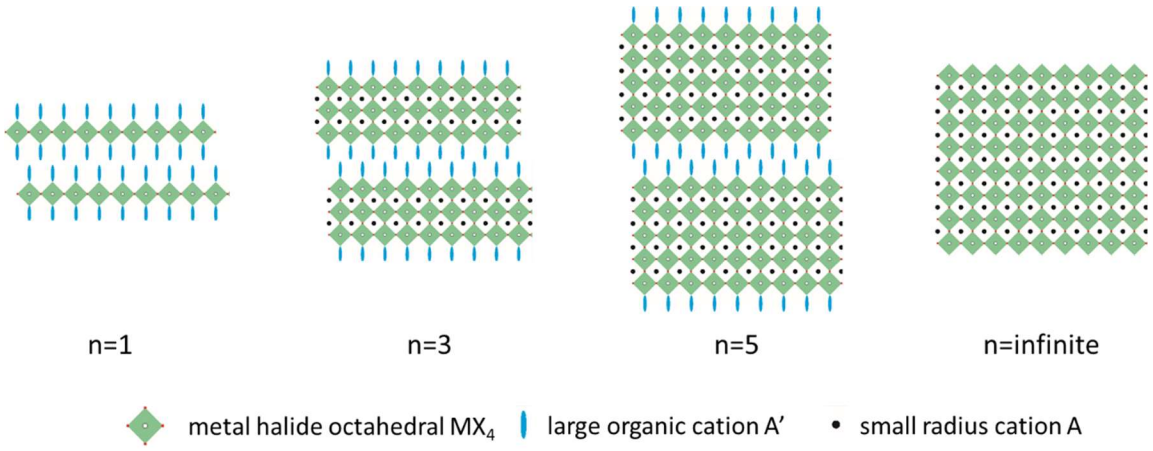


Figure 1- 5 Schematic layered structures of 2D perovskite nanoplates with different n values (n=1, 3, 5 and infinite).

1.2 Perovskite optoelectronic devices

Outstanding properties such as co-existed superior semiconducting properties[8,40], electrical polarization [41-43], non-degenerate spin states [44,45] and low-temperature processabilities [46-49] have been demonstrated in organic-inorganic hybrid perovskites, making it a promising candidate for optoelectronic devices, such as solar cells, light emitting diodes and photodetectors.

1.2.1 Solar cells

Figure 1-6a shows a typical solar cell device structure where the photoactive layer is sandwiched by a hole transport layer and an electron transport layer. In addition, the anode and cathode are attached to hole transport layer and electron transport layer respectively. As schematic shown in **Figure 1-6b**, the photoactive semiconductors can absorb photons with energy higher than the materials' bandgap, leading to the electrons in the valance band to be excited to conduction band and leaving electron vacancies (excited holes) at the valance band. The primary photogenerated electron-hole pairs can be dissociate into free electrons and holes, which will be transferred into electron transport layer and hole transport layer separately, and eventually extracted by cathode and anode.

Therefore, the energy of photons (solar energy) is converted to electrical energy, which is the essence of solar cells. In order to quantify the power conversion efficiency (PCE: the ratio of electrical energy to solar energy) of the solar cells, current-voltage curve under one sun illumination is plotted (as exampled in **Figure 1-6c**). As shown in **Figure 1-6c**, the PCE is determined by three key parameters: Voc, Jsc and FF. Specifically, Voc is called the open circuit voltage, which equals to the magnitude of applied bias when the current density is zero (i.e. the open circuit condition). Jsc is called the short circuit current, which equals to the magnitude of current density when the applied bias is zero (short circuit condition). FF is called the fill factor, which equals to the ratio of maximal output power (product of current and voltage) to the product of the open circuit voltage and short circuit current.

Compared with the traditional solar cells such as inorganic solar cells based on silicon or gallium arsenide and organic solar cells, the organic inorganic hybrid perovskite solar cells are of great advantages due to their coexisted properties like exceptionally high defect tolerance, high absorption coefficient, high carrier mobility, tunable bandgap and low-cost processing method. To

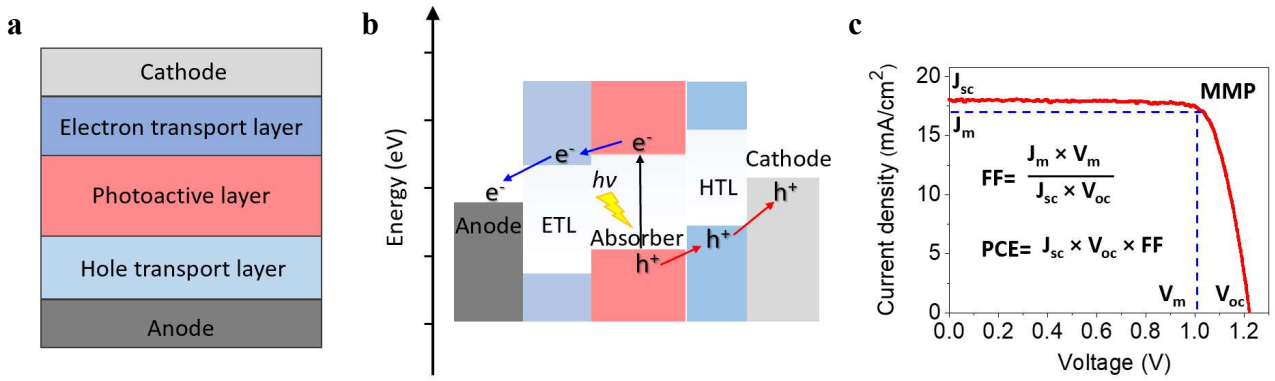


Figure 1- 6 (a) Schematic device structure of a solar cell. (b) The energy level diagram of a solar cell and the arrows indicate the transportation of photogenerated carriers. (c) Current-voltage curve for a solar cell at one sun condition. MMP is maximum power point.

date, the efficiency of 3D lead based perovskite solar cells is boosted from 3.8% to 25.2% within a few years [50-55], as shown in **Figure 1-7**.

Toward reducing the toxicity, lead-free tin based perovskite solar cells are developed, while highly concentrated tin vacancies are formed owing to the instability of the oxidation state of tin (Sn^{2+}). This largely suppresses the efficiency of tin based perovskite solar cells [56-62], requiring further material engineering to improve the quality of tin based perovskites. At the same time, replacing high-atomic-number element lead (n=82) with low-atomic-number element tin (n=50), the spin-orbital coupling of perovskite is reduced. This leads to a weak conversion from optically generated bright states to dark states, requiring new strategies to facilitate the conversion toward photovoltaic actions.

Toward improving the stability, hydrophobic large organic cations are incorporated into 3D perovskite, resulting in 2D perovskite nanoplates. As the large organic cation can not only prevent metal-halide octahedron from exposing to moisture and oxygen, but also suppress the ion migration, thus solar cells based on 2D perovskites have shown significantly enhanced environmental and operational stabilities [63-65]. However, the insulating nature of the large organic cation such as n-butylammonium (BA) or 2-phenylethylammonium (PEA) severely hinders the carriers transport in 2D perovskite solar cells, leading to low short-circuit photocurrent (Jsc) and fill factor (FF). The 2D perovskite nanoplates actually are lead-halide octahedral sheet sandwiched by two large organic layers. Thus, electrical conductivity of 2D perovskite nanoplates is much higher in the in-plane direction than in the out-of-plane direction. With respect to the electrode contacts in planar solar cells, preferential out-of-plane crystallization alignment of 2D perovskite nanoplates can facilitate the carrier transport. This can be accomplished by hot casting technology [66], doping [67] and solvent engineering [68].

In addition, the formula of 2D perovskites is $A'_2A_{n-1}B_nX_{3n+1}$, where n refers to the number of planes of the corner-sharing $[BX_6]^{4-}$ octahedral, and A', A, B, X refer to the large organic cations, small radius cations, divalent metal cations and halide anions, respectively. During the fabrication process of the target pure-n-value 2D perovskite nanoplates, multiple phases with a mixture of different-n-value nanoplates, namely quasi-2D perovskites will be formed instead of pure-n-value 2D nanoplates, which is caused by the large solubility difference between large organic cation A' and cation A with small radius. For example, n value of the precursor solution

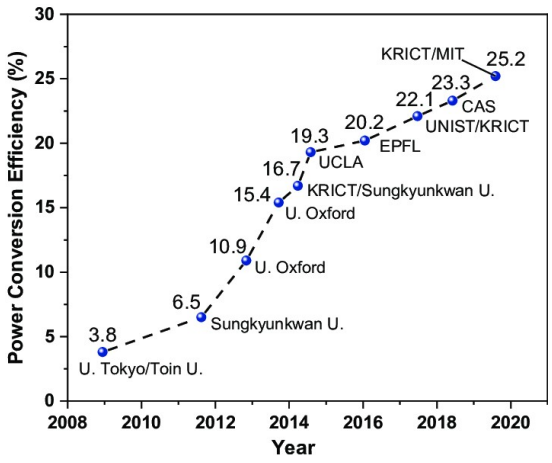


Figure 1- 7 The efficiency evolution of perovskite solar cells. Data is replotted from ref. [55]

prepared for 2D perovskite $PEA_2MA_4Pb_5I_{16}$ is set to be 5, however the obtained film will contains nanoplates with different-n-values such as n=1 (PEA_2PbI_4), n=2 ($PEA_2MAPb_2I_7$), n=3 ($PEA_2MA_2Pb_3I_{10}$), n=4 ($PEA_2MA_3Pb_4I_{13}$), n=5 ($PEA_2MA_4Pb_5I_{16}$), ···, n=10 ($PEA_2MA_9Pb_{10}I_{31}$) ···, and n=infinity ($MAPbI_3$). The nanoplates with lower n value have wider optical bandgap, larger exciton binding energy and poorer electrical conductivity, whereas the large-n-value nanoplates have narrower optical bandgap, reduced exciton binding and better electrical conductivity. Due to band diagram between different-n-value nanoplates (**Figure 1-8**), charge transfer occurs from small-n-value nanoplates to large-n-value nanoplates. Thus, controlling the spatial distribution of different-n-value nanoplates plays an important role to enhance the charge transfer from small to large-n-value nanoplates toward enhancing the carrier transport, thereby improving the photovoltaic performance of quasi-2D perovskite solar cells.

1.2.2 Light emitting diodes

Figure 1-9a shows a typical light emitting diodes structure of anode/hole buffer layer/hole transport layer/light emitting layer/electron transport layer/electron buffer layer/cathode. At working condition, holes and electrons are injected through anode and cathode, respectively. These injected holes and electrons can meet within the light emitting layer and form excited light emitting states ready for radiative recombination (**Figure 1-9b**). As a reverse process of solar cells, the light emitting diodes are designed to convert electrical energy to photon energy. The conversion efficiency is described as the external quantum efficiency (EQE), which equals to the ratio of emitted photon number to the injected charge number.

Organic-inorganic hybrid perovskites have recently demonstrated remarkable electroluminescence (EL) actions with solution processing and spectral tuning properties based on the effort from materials synthesis and device interface engineering [69-72]. Toward highly efficient perovskite LEDs, it requires various advanced engineering strategies such as increasing quantum confinement, minimizing trap assisted recombination and enhancing light outcoupling. Regarding the quantum confinement, low dimensional perovskite structures or perovskite nanocrystals are designed via various proposed strategies such as elemental substitution and ligand incorporation, which enables a very high PL quantum efficiency (PLQY) [73-75] ready for perovskite LED fabrication. Regarding the reduction of trap assisted nonradiative recombination, additive engineering and post treatment are applied to decrease defects within the perovskite films.

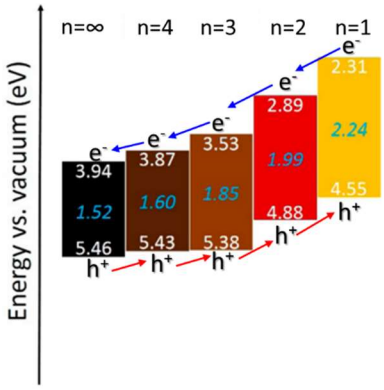


Figure 1- 8 Energy levels for 2D perovskite with different n values, and the arrows indicates the direction of charge transfer between different-n-value nanoplates. Figure is adapted from ref. [76]

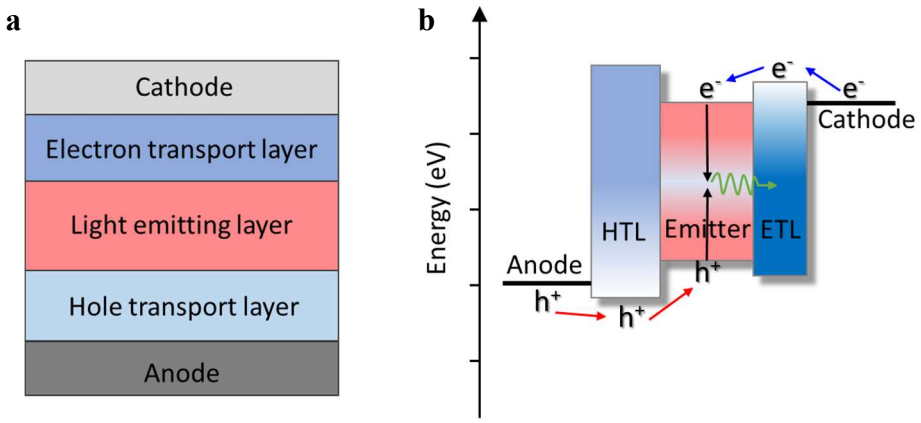


Figure 1- 9 (a) Schematic device structure of a light emitting diode (LED). (b) The energy level diagram of a LED device and the arrows indicate the transportation of injected charge carriers.

Regarding the light outcoupling enhancement, optimizing film thickness and realizing isolated nanostructured perovskite grains are the commonly used strategies [77]. With these overall efforts, the EQE of perovskite LED has been pushed to over 20% in near infrared and green region and over 10% in blue region [77].

1.2.3 Photodetectors

The photodetectors, or photosensors, are sensors to detect photons with the detection signal usually revealed via photocurrent. In view of achieving high current upon light illumination in photodetectors, two strategies are applied: i) making use of photogenerated excited carriers' collection toward high current, and ii) enhancing the charge injection from electrodes toward current amplification [78]. The working principle of the first strategy is nearly the same as the solar cells. Specifically, when a photon is absorbed to generate an excited electron-hole pair, an external bias is usually required to assist the dissociation of electron-hole pair as well as the charge carrier transport and collection. In the second strategy, charge injection enhancement is usually realized through de-trapping defects within the device and/or decreasing the injection barrier at interface between transport layer and electrode.

In the evaluation of the photodetector performance, the ON-OFF ratio, detectivity and responsivity are the key parameters. Here, the ON-OFF ratio refers to the ratio of current upon light illumination to current at dark condition. Therefore, decreasing dark current together with increasing light current is essential to improve the performance of photodetectors. The detectivity determines how weak the light can be detected, which is defined as the inverse of the noise-equivalent power (NEP). Hence, the larger the detectivity is, the more accurate it is to detect week signals which compete with the noise. Another parameter responsivity reflects the efficiency of a detector, which is defined as the ratio of photocurrent to detected light intensity.

Organic inorganic hybrid perovskites have recently emerged as a promising candidate for commercial photodetectors, owing to the superior optoelectronic properties such as broad and tunable light absorption with large absorption coefficient, efficient charge carrier generation and excellent charge transport. To date, various perovskite based photodetectors [78, 79] have been demonstrated such as using different perovskite sources with single crystals, 3D polycrystalline

films or even nanowires, using different device structures with vertical design or planar design and combining perovskite layer with other two-dimensional layers (e.g. graphene).

1.3 Dissertation Outline

Behaviors of excited states form the foundation of optoelectronics, such as light emitting diodes, solar cells and lasers. Thoroughly understanding the photophysical processes of excited states are suggested to further pushing the optoelectronic efficiency forward, including the perovskite-based devices. The research in this thesis mainly focuses on the manipulation of excited states through combining optoelectronic devices, from excited states generation to excited charge carrier transport. We will also introduce several different perovskite films (2D, quasi-2D and 3D) together with the corresponding solar cells or LEDs. The related underlying mechanism is explored. The outline of this thesis is briefly introduced as follows.

Chapter 2 establishes charge-transfer excitons in 2D perovskite heterostructures (PEA_2PbI_4/PEA_2SnI_4). It can lead to bright broad emission, which brings about new opportunity to develop high-performance perovskite LEDs and solar cells. Chapter 3 explores the orbit-orbit interaction between excitons when doping is used to improve the photovoltaic efficiency in lead-free Sn perovskite solar cells. This study reveals orbit-orbit interaction is enhanced through SnF_2 doping in $FASnI_2Br$ based perovskites. Chapter 4 introduces long-order orbital interaction through slow hot-carrier cooling in quasi-2D perovskite films. This work explores the possible strategies to increase the population of dark states through long-order orbit-orbit interaction toward highly efficient quasi-2D perovskite solar cells. Chapter 5 proposes a new strategy (uniform permutation of 2D nanoplates) in quasi-2D perovskite films toward efficient charge collection. This work develops a vacuum poling treatment to enable uniform permutation of 2D nanoplates, leading to a champion high fill factor in quasi-2D perovskite solar cells. Chapter 6 realizes alternating current (AC) electroluminescence in quasi-2D perovskite LEDs. This work proposes a new strategy to facilitate bipolar carrier transport toward efficient AC driven LED. Chapter 7 concludes the entire studies in this thesis and provides an outlook for future works.

Chapter 2 Establishing charge-transfer excitons in 2D perovskite heterostructures

2.1 Abstract

Charge-transfer excitons (CTEs) immensely enrich property-tuning capabilities of semiconducting materials. However, such concept has been remaining as unexplored topic within halide perovskite structures. Here, we report that CTEs can be effectively formed in heterostructured 2D perovskites prepared by mixing PEA_2PbI_4:PEA_2SnI_4, functioning as host and guest components. Remarkably, a broad emission can be demonstrated with quick formation of 3 ps but prolonged lifetime of ~ 0.5 μs. This broad PL presents the hypothesis of CTEs, verified by the exclusion of lattice distortion and doping effects through demonstrating double-layered PEA_2PbI_4/PEA_2SnI_4 heterostructure when shearing-away PEA_2SnI_4 film onto the surface of PEA_2PbI_4 film by using hand-finger pressing method. The below-bandgap photocurrent indicates that CTEs are vital states formed at PEA_2PbI_4:PEA_2SnI_4 interfaces in 2D perovskite heterostructures. Electroluminescence shows that CTEs can be directly formed with electrically injected carriers in perovskite LEDs. Clearly, the CTEs presents a new mechanism to advance the multifunctionalities in 2D perovskites.

2.2 Introduction

Initiated by fast developing thin-film photovoltaic functionalities[80-83], organic-inorganic hybrid metal halide perovskites have emerged as interesting light-emitting materials with high photoluminescence quantum yields[84-86], large color tuning capabilities[2-4], domain-size controllable exciton binding energies[87, 88], and bandgap engineering properties[89-91]. With these attractive optical characteristics, the hybrid perovskites have demonstrated high-performance LEDs[85,92-94] based on solution-processed thin-film formation procedures. Undoubtedly, the excitons formed within intrinsic perovskite structures are solely responsible for developing high-performance light-emitting properties. Because the excitons are generated by electron-hole capture within band structures in such hybrid perovskites, tuning excitonic properties requires substantial engineering on band structures through materials design. This often leads to complex experimental procedures to tune light-emitting properties in hybrid metal halide perovskites. Interestingly, charge-transfer excitons have been introduced as artificial excitons with spatially extended wavefunctions, widely observed in low dielectric-constant organic materials through donor-acceptor design, to develop high-efficiency optoelectronic functionalities [95, 96]. It has been recognized as an intriguing nature that charge-transfer excitons can be conveniently tuned on energy, polarization, and spin

parameters by physically changing the formulation of heterostructures [97]. This leads to unique tuning capabilities to control optic, electric, and magnetic functionalities where charge-transfer excitons are utilized [98].

In general, charge-transfer excitons can be formed at heterostructures where charge transfer occurs at heterointerfaces to form electron-hole pairs. The heterostructures can be both chemically and physically prepared by using two molecular structures where different electron negativities exist [99, 100]. In general, the heterostructures can be naturally formed between donor-type and acceptor-type structures, leading to exciplexes [101-103]. On the other hand, the heterostructures can be partially formed between two same-type molecular structures where local energy disorders exist, forming excimers [104, 105]. In the past, the charge-transfer excitons have been extensively explored in organic heterostructures prepared by chemical synthesis, physical mixing, and mechanical formation of film-interfaces towards light-emitting, lasing, photovoltaic, sensing and magneto-optical applications [106 - 108]. Recently, it has been shown that the perovskite-polymer bulk heterostructure, prepared by mixing quasi-2D/3D perovskite with wide-bandgap polymer, demonstrates a broad transient absorption (TA) signal which is quickly appeared in 1 ps and slowly relaxed in nanoseconds [93]. This presents the possibility to form CTEs between perovskite and organic polymer, known as high and low-dielectric materials. Essentially, the CTEs can be formed when a charge transfer process is occurred with the consequence of forming electron-hole pairs between two adjacent structures with different electron negativities and local energies. It has also been observed that CTEs can be formed between 2D perovskite (BA_2PbI_4) and organic molecule [1,4,5,8,9,11-hexaazatriphenylenehexacarbonitrile (HATCN)] when the charge transfer at the interface is enhanced by orbital overlap[14]. Clearly, these published results provide the necessary condition to explore the CTEs within perovskite heterostructures.

In this work, we initially utilized the chemical method to prepare 2D perovskite heterostructures [$(PEA_2PbI_4)_x$:$(PEA_2SnI_4)_{1-x}$] by alternatively selecting the host and guest components when mixing two precursor (Pb and Sn perovskites) solutions with distinctly high and low concentrations. The heterostructures with alternatively switched host and guest components are both demonstrated with similar broad emission spectra and prolonged lifetime (~ microseconds). This observation provides the first indication that the CTEs are formed at the [PEA_2PbI_4:PEA_2SnI_4] interfaces within heterostructures [$(PEA_2PbI_4)_{0.999}$:$(PEA_2SnI_4)_{0.001}$] and

[$(PEA_2SnI_4)_{0.999}$:$(PEA_2PbI_4)_{0.001}$] to generate a broad emission in 2D perovskites. Remarkably, the broad emission can be reproduced when using hand-finger pressing method to mechanically shearing-away the PEA_2SnI_4 film onto the PEA_2PbI_4 film surface to uniquely prepare the double-layered heterostructures without lattice distortion and doping effects. This hand-finger pressing method confirms that the broad emission represents the signature for CTEs formed in 2D perovskite heterostructures. The pump-probe TA studies present that the CTEs are quickly formed and essentially become metastable states, as compared to surface-trapped and intrinsic excitons in 2D perovskites. This work has been published (*Nature Communications 11*, 2618, 2020).

2.3 Materials and Methods

2.3.1 Materials synthesis and device fabrication

Lead iodide (PbI_2), tin iodide (SnI_2), Poly(9-vinylcarbazole) (PVK), 2,2',2''-(1,3,5-Benzinetriyl)-tris(1-phenyl-1-H-benzimidazole) (TPBi), lithium fluoride (LiF), chlorobenzene (CB), Isopropyl Alcohol (IPA) and dimethyl sulfoxide (DMSO) were purchased from Sigma-Aldrich. Phenethylammonium iodide (PEAI) was purchased from Greatcell Solar. Phenyl-C_{61}-butyric acid methyl ($PC_{61}BM$) was purchased from 1-Materials. Poly (3,4-ethylenedioxythiophene) polystyrene sulfonate (PEDOT: PSS) was purchased from Clevios. All chemicals are used as received without further purification. The precursor solution of PEA_2PbI_4 was prepared by mixing PEAI (0.8 M) and PbI_2 (0.4 M) in DMSO (1 mL). The precursor solution of PEA_2SnI_4 was made in the same way by replacing PbI_2 with SnI_2. Heterostructures of [$(PEA_2PbI_4)_{1-x}$:$(PEA_2SnI_4)_x$] were designed by mixing two precursor (PEA_2PbI_4 and PEA_2SnI_4) solutions with alternatively selected high and low volume ratios. All the perovskite films were fabricated by spin-coating the precursor solutions on glass slides (1.5×1.5 cm^2) at 3000 rpm for 30 s, then annealing at 100 ˚C for 10 minutes (**Figure 2-1**).

2.3.2 Fabrications of LED and photodetector.

The patterned ITO substrates were first cleaned by ultrasonic treatments with detergent, deionized water, acetone and isopropanol respectively, for 20 minutes in each step and dried with nitrogen gas, then followed by UV treatment for 30 minutes. After that, the PEDOT:PSS hole-transport layer of 40 nm was spin-coated on the precleaned ITO substrates at 4000 rpm for 60

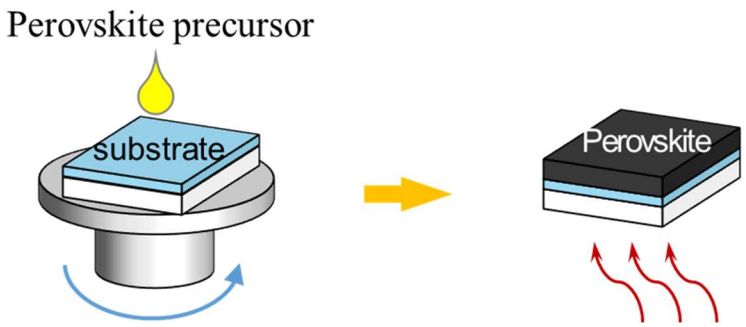


Figure 2- 1 Schematic diagram of perovskite film fabrication procedure through one-step spin-coating method.

seconds, and annealed at 150 ℃ for 30 minutes. For LED devices, a thin layer of polyvinylcarbarzole (PVK) (16 mg/ml dissolved in chlorobenzene) was spin-coated on the PEDOT:PSS layers with a speed of 5000 rpm for 60 seconds, and treated with the thermal annealing at 120 ℃ for 20 minutes. The 2D perovskite precursor solutions were spin-coated as described above. The TPBi was vacuum-deposited with the thickness of 50 nm. 2 nm LiF and 90 nm silver were evaporated to prepare the perovskite LEDs with the architecture of ITO/PEDOT:PSS/PVK/perovskite/TPBi/LiF/Ag. For the fabrication of photodetector devices, the $PC_{61}BM$ (25 mg/ml dissolved in chlorobenzene) was spin coated at 2000 rpm for 50 seconds, without thermal annealing, serving as an electron-transport layer, then an interface modification layer of PEI (0.5 mg/ml, IPA) was spin coated at 5000 rpm for 60 seconds, and followed by the evaporation of silver electrode of 90 nm. This leads to the photodetector device architecture of ITO/PEDOT:PSS/perovskite/$PC_{61}BM$/PEI/Ag. The active area for both LED and photodetector devices is 0.06 cm^2.

2.3.3 Mechanically preparing heterostructures.

The double-layer 2D perovskite heterostructures were prepared by using hand-finger pressing method to avoid lattice distortion and doping effect. Specifically, the PEA_2SnI_4 film coated on glass substrate was held on the PEA_2PbI_4 film with the face-to-face contact by using hand-finger pressing method. Then, the PEA_2SnI_4 film was shearing on the surface of PEA_2PbI_4 film. This leaves the PEA_2SnI_4 film-islands on the PEA_2PbI_4 film, leading to double-layer heterointerfaces (PEA_2SnI_4/PEA_2PbI_4). The PEA_2SnI_4 film-islands can be visible as pale-yellow color on the PEA_2PbI_4 film. Therefore, our hand-finger pressing method can prepare the heterostructures without lattice distortion and doping effects to confirm the charge-transfer excitons responsible for broad emission observed in 2D perovskite heterostructures.

2.3.4 Characterizations and measurements

The steady-state and time-resolved PL characteristics were measured with Flouro Log III spectrometer. The absorption spectrum was measured with UV3600 (Shimadzu, Japan). Transient absorption spectra were collected by using a Helios fire spectrometer (Ultrafast Systems LLC). The pump beam (346 nm, 5μW) was generated through a harmonic generator (Ultrafast Systems LLC, third harmonic) pumped by a Pharos laser (Light Conversion, 1kHz, 1030nm, 290fs). The

probe beam was selected from the broad light emission generated by CaF_2 crystal excited by 1030 nm fs primary beam.

2.4 Results and discussion

2.4.1 CTEs in heterostructured 2D perovskite thin film

The 2D perovskite films were prepared by spin coating from mixed two precursor solutions (PEA_2PbI_4 and PEA_2SnI_4) and followed with thermal annealing at 100˚C for 10 minutes. The two precursor solutions were initially mixed with the volume ratio of 99.9:0.1 to formulate the heterostructures $[(PEA_2PbI_4)_{0.999}:(PEA_2SnI_4)_{0.001}]$ in 2D perovskite films where the PEA_2PbI_4 and PEA_2SnI_4 act as host and guest components, respectively. Furthermore, the PEA_2PbI_4 and PEA_2SnI_4 were alternatively switched with distinctly low and high concentrations, serving as guest and host components, to formulate the heterostructures $[(PEA_2SnI_4)_{0.999}:(PEA_2PbI_4)_{0.001}]$ in 2D perovskite films.

Figure 2-2a shows that mixing 0.1 % PEA_2SnI_4 into 99.9 % PEA_2PbI_4 has little effect on the absorption characteristics in the heterostructures $[(PEA_2PbI_4)_{0.999}:(PEA_2SnI_4)_{0.001}]$ where the bandgap is governed by the host (PEA_2PbI_4) component. Interestingly, a very broad PL spectrum is observed between 575 nm and 800 nm with the peak position located at 669 nm. When we further increase the guest Sn perovskite concentration to 1% or even 5%, broad emission can always be observed at same wavelength (**Figure 2-2b**). As a comparison, the PEA_2PbI_4 and PEA_2SnI_4 perovskites give rise to their intrinsic photoluminescence (PL) at 524 nm and 621 nm, shown as spectral shoulders on the broad emission spectrum. The broad PL demonstrates a very broad spectral width of 127 nm while the intrinsic emission from the PEA_2PbI_4 and PEA_2SnI_4 components give rise to much narrower spectral widths (15 nm and 37 nm). Remarkably, when the host and guest components are alternatively switched to shift the bandgap (derived from optical absorption) largely from 2.33 eV in the $[(PEA_2PbI_4)_{0.999}:(PEA_2SnI_4)_{0.001}]$ to 1.95 eV in the $[(PEA_2SnI_4)_{0.999}:(PEA_2PbI_4)_{0.001}]$, the broad emission spectrum is only slightly changed from 669 nm (1.85 eV) to 697 nm (1.78 eV) in peak position, leading to similar broad emission spectra between $[(PEA_2PbI_4)_{0.999}:(PEA_2SnI_4)_{0.001}]$ and $[(PEA_2SnI_4)_{0.999}:(PEA_2PbI_4)_{0.001}]$ heterostructures, as indicated in **Figure 2-2c**. The similar broad emission observed by alternatively switching the host and guest components in 2D perovskite heterostructures $[(PEA_2PbI_4)_{0.999}:(PEA_2SnI_4)_{0.001}]$ and

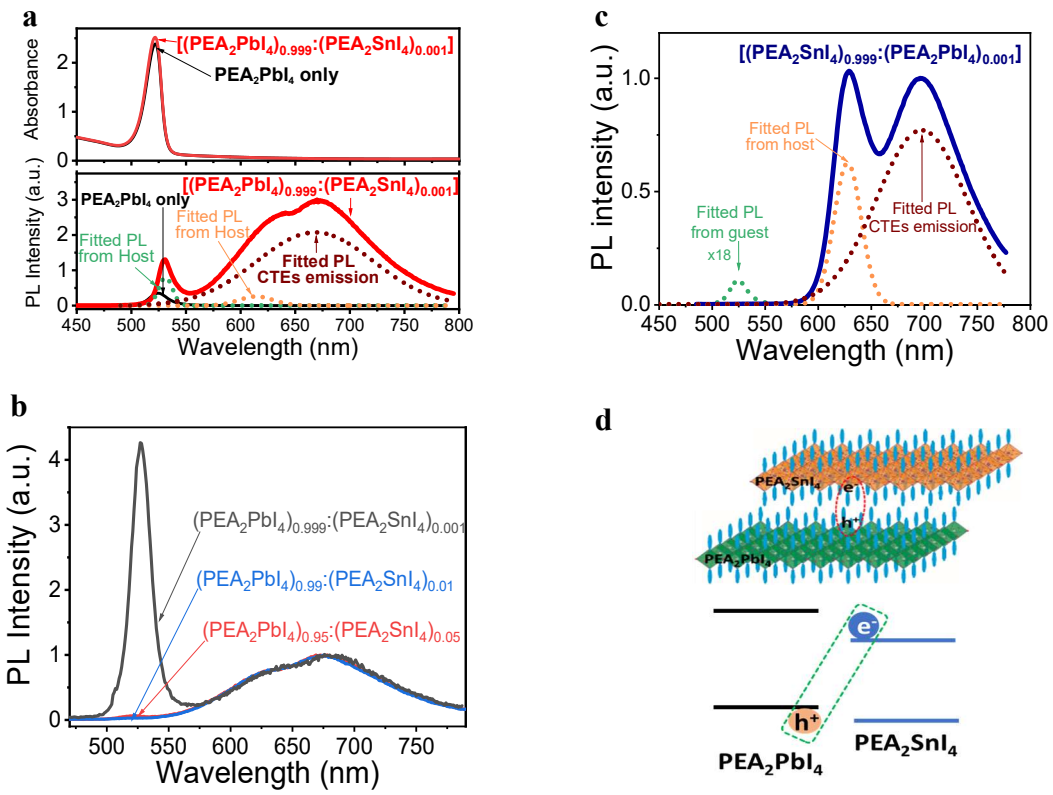


Figure 2-2 Optical characteristics of CTEs formation in 2D perovskite heterostructures. (a) Absorption and PL spectra are shown for 2D perovskite heterostructured $[(PEA_2PbI_4)_{0.999}:(PEA_2SnI_4)_{0.001}]$ film. The absorption spectrum indicates that the bandgap is governed by the host (PEA_2PbI_4) component in the heterostructures. The PL spectrum is dominated by a broad emission peaked at 669 nm with a spectral shoulder at 614 nm from the guest (PEA_2SnI_4) and the intrinsic emission (peaked at 531 nm) from the host (PEA_2PbI_4). (b) Normalized PL spectra to show broad light emission peaked at 669 nm for heterostructured $[(PEA_2PbI_4)_{1-x}:(PEA_2SnI_4)_x]$ films. (c) PL spectrum is shown for 2D perovskite heterostructured $[(PEA_2SnI_4)_{0.999}:(PEA_2PbI_4)_{0.001}]$ film after switching host and guest components. The broad emission is observed with the peak position at 697 nm, in addition to intrinsic emission (peaked at 524 nm and 627 nm) from host (PEA_2PbI_4) and guest (PEA_2SnI_4) components. The PL spectra for pristine PEA_2PbI_4 and PEA_2SnI_4 films are also shown as reference. (d) Schematic diagram illustrates the formation of CTEs at the interfaces between PEA_2PbI_4 and PEA_2SnI_4 components in 2D perovskite heterostructures $[(PEA_2PbI_4)_{1-x}:(PEA_2SnI_4)_x]$.

[$(PEA_2SnI_4)_{0.999}$:$(PEA_2PbI_4)_{0.001}$] lead to the hypothesis that the CTEs are formed at the interfaces between local PEA_2PbI_4 and PEA_2SnI_4 structures, as illustrated in **Figure 2-2d**. Here, the formation of CTEs requires that (i) the charge transfer is occurred from local host to guest structures and (ii) the electron-hole pairs are formed at the interfaces in the 2D perovskite heterostructures.

To further understand the origin of broad emission occurring in the 2D perovskite heterostructures, we measured the PL intensity dependence and lifetime characteristics. We can see in **Figure 2-3a** and **3b** that the broad emission exhibits the intensity-dependence slop of 1.62, while the intrinsic emission from the host PEA_2PbI_4 component gives rise to the intensity-dependence slop of 1.14. We should note that germinate process dominates the radiative recombination of the intrinsic excitons in host/guest 2D perovskites due to large exciton binding energy, which leads to the power dependence slope of ~1. On the other hand, when electrons and holes are paired to form electron-hole pairs, the pairing probability *p* is proportional to the product between the number (n) of electrons and the number (m) of holes: $p \propto m \cdot n$. In the situation where n=m, then $p \propto n^2$. Therefore, the non-germinate recombination can lead to the intensity-dependence slope of 2 in light emission. Here, the broad emission of our heterostructured [$(PEA_2PbI_4)_{0.95}$:$(PEA_2SnI_4)_{0.05}$] film demonstrates the power dependence slope of 1.62, presenting the suggestion that the CTEs are responsible for the broad emission through non-germinate recombination.

Furthermore, the broad emission peaked at 669 nm shows much prolonged lifetime of 0.5 μs relative to the short lifetime of 1 ns of the intrinsic emission peaked at 524 nm from the host PEA_2PbI_4 component, as shown in **Figure 2-3c**. In general, the lifetime of CTEs is mainly determined by the electron-hole recombination rate governed by Coulomb attractive force. As a result, CTEs often exhibit an extended lifetime due to longer electron-hole separation distance as compared to intrinsic excitons in semiconducting materials.

Here, the much prolonged PL lifetime further verifies that the broad emission originates from CTEs in heterostructured 2D perovskites. We should note that CTEs can still demonstrate various lifetimes when the Coulomb attraction between electron and hole located on different energetic structures is changed by local dielectric backgrounds, widely observed in organic-organic [109-111], organic-inorganic[112], inorganic-inorganic mixtures[113].

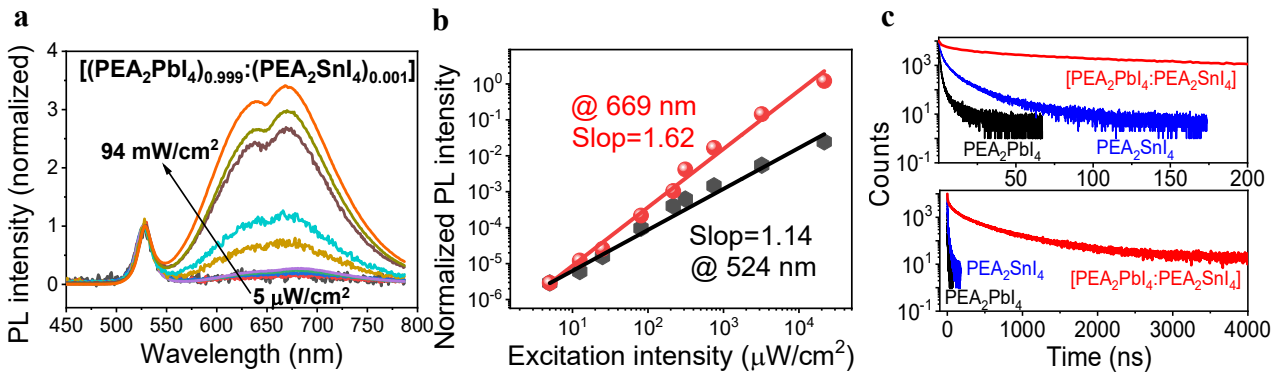


Figure 2- 3 PL characteristics for 2D perovskite heterostructured $[(PEA_2PbI_4)_{0.999}:(PEA_2SnI_4)_{0.001}]$ film. (a) Normalized PL spectra at different excitation intensities ranging from 5 μW/cm^2 to 94 mW/cm^2. (b) PL-excitation intensity dependences for broad emission (peaked at 669 nm) as compared to intrinsic emission (524 nm) from host (PEA_2PbI_4). (c) PL lifetime results for broad emission (peaked at 669 nm) in 2D perovskite heterostructures and intrinsic emission (peaked at 524 nm, and 621 nm) from host (PEA_2PbI_4) and guest (PEA_2SnI_4).

2.4.2 CTEs in double-layered 2D perovskite heterostructures

We note that, in the mixed two precursor solutions with 99.9 % host and 0.1 % guest concentrations, the PEA_2PbI_4 and PEA_2SnI_4 have slower and faster crystallization rates to form heterostructured 2D perovskite [$(PEA_2PbI_4)_{0.999}$:$(PEA_2SnI_4)_{0.001}$] films. This is because the Pb and Sn perovskites have higher and lower Gibbs energies, respectively [114]. Consequently, the PEA_2SnI_4 domains can be quickly formed and followed with the formation of PEA_2PbI_4 domains, leading to the heterostructured 2D perovskite films. The heterostructures provide the necessary condition to initiate the charge transfer from the host to the guest domains towards the formation of CTEs at the host: guest interfaces. Essentially, the CTEs can be formed through Coulomb capture at the interfaces between PEA_2PbI_4 and PEA_2SnI_4 domains in 2D perovskite heterostructures. However, there is a question of whether the low-concentration guest (PEA_2SnI_4) molecules dope into the high-concentration host (PEA_2PbI_4) domains, leading to the possibility of doping effect to generate a broad emission through the so-called self-trapped excitons caused by lattice deformation, which was proposed for doping-induced deformation in (100) 2D single crystals [115] and corrugated (110) 2D structures [116, 117].

To clarify this question, we designed a unique experimental method to mechanically prepare the double-layered PEA_2PbI_4/PEA_2SnI_4 heterointerface by shearing-away the PEA_2SnI_4 film onto the surface of PEA_2PbI_4 film through hand-finger pressing procedure. Specifically, the PEA_2SnI_4 and PEA_2PbI_4 films were separately spin-cast on glass substrates followed by thermal annealing. Then, the PEA_2SnI_4 film coated on glass substrate was hold onto the PEA_2PbI_4 film coated on another glass substrate with face-to-face contact under hand-finger pressing, as schematically illustrated in **Figure 2-4a**. Upon hand-finger pressing with face-to-face contact, the PEA_2SnI_4 film was parallelly shearing away from the surface of PEA_2PbI_4 film. This hand-finger pressing method leaves the PEA_2SnI_4 film-islands on the surface of PEA_2PbI_4 film, forming the double-layered [PEA_2PbI_4/PEA_2SnI_4] interfaces, functioning as heterostructures clearly without doping effects and lattice deformation.

Therefore, our hand-finger pressing method provides a unique experimental approach to clarify the origin of broad emission widely observed in hybrid metal halide perovskite heterostructures formed by mixing different precursor solutions or in nanocrystals formed with lattice strains. Here, it is very interesting to show that our broad emission can be reproduced with

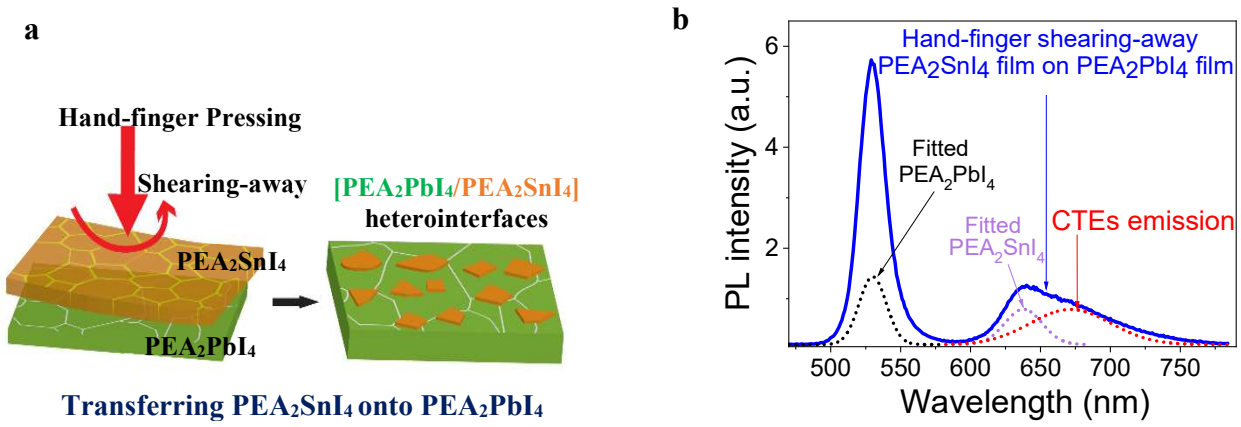


Figure 2- 4 Hand-finger pressing method to confirm CTEs formation in 2D perovskite heterostructures. (a) Schematic diagram illustrates that show PEA_2SnI_4 film is shearing-away on PEA_2PbI_4 film surface to prepare double-layered [PEA_2PbI_4/PEA_2SnI_4] heterointerfaces. (b) PL spectrum was measured for double-layered [PEA_2PbI_4/PEA_2SnI_4] heterointerfaces. The broad emission is shown as an extended spectral tail in addition to intrinsic emission (530 nm and 637.5 nm) from PEA_2PbI_4 and PEA_2SnI_4 components. The dashed lines are shown for three spectral components from PEA_2PbI_4 component, PEA_2SnI_4 component, and [PEA_2PbI_4/PEA_2SnI_4] heterointerfaces.

the peak position at 671 nm in the double-layered PEA_2PbI_4/PEA_2SnI_4 interfaces prepared by our hand-finger pressing method (**Figure 2-4b**), very similar to the broad emission observed by mixing two precursor solutions. Because our hand-finger pressing method can only form a low density of double-layered PEA_2PbI_4/PEA_2SnI_4 heterostructures, the broad emission becomes an appreciable shoulder on the intrinsic emission peaked at 638 nm from the PEA_2SnI_4 perovskite. Clearly, the similar broad emission observed from our hand-finger pressing method as compared to the precursor-solution mixing method provides an unambiguous evidence to confirm that the broad emission indeed represents the CTEs formed at the interfaces between PEA_2PbI_4 and PEA_2SnI_4 domains in 2D perovskite heterostructures.

2.4.3 Dynamic analysis of CTEs formation.

To explore the dynamic behaviors of the CTEs, we performed pump-probe TA studies on the heterostructured 2D perovskite $[(PEA_2PbI_4)_{0.95}:(PEA_2SnI_4)_{0.05}]$ film (**Figure 2-5a**). The TA characteristics show an interesting phenomenon where a broad signal is observed between 600 nm and 800 nm (bottom panel in **Figure 2-5a**). Obviously, the broad TA signal is consistent with the broad emission from CTEs in the heterostructured 2D perovskite film. Contrarily, the pristine PEA_2PbI_4 film does not show any broad TA signal between 600 nm and 800 nm, only leading to a photo-bleaching signal peaked at 514 nm related to intrinsic excitons, as shown in **Figure 2-5b**. Clearly, the broad TA signal provides the dynamic information of CTEs formed in 2D perovskite heterostructures. **Figure 2-5c** summarizes the dynamic characteristics of CTEs with the broad TA signal between 600 nm and 800 nm occurring at the $[PEA_2PbI_4:PEA_2SnI_4]$ interfaces in 2D perovskite heterostructures $[(PEA_2PbI_4)_{0.95}:(PEA_2SnI_4)_{0.05}]$. The CTEs shown as the broad TA signal between 600 nm and 800 nm are quickly formed in 3 ps and slowly generate a light emission after 230 ps. Interestingly, the broad photoinduced bleaching TA signal extends to a few nanoseconds without any appreciable decay. This indicates that the CTEs are essentially metastable states in 2D perovskite heterostructures. Furthermore, the TA characteristics show a spectral shoulder at 537.5 nm in the heterostructured 2D perovskite film, slightly below the emission from intrinsic excitons (peaked at 513.8 nm) in the PEA_2PbI_4 domains. This spectral shoulder (537.5 nm) is formed in 1 ps, quickly demonstrates a light emission after 2.2 ps and decays within nanosecond time window. By considering the lower energy (51 meV below the band-to-band transition) and photobleaching developed after the band-to-band transition, we

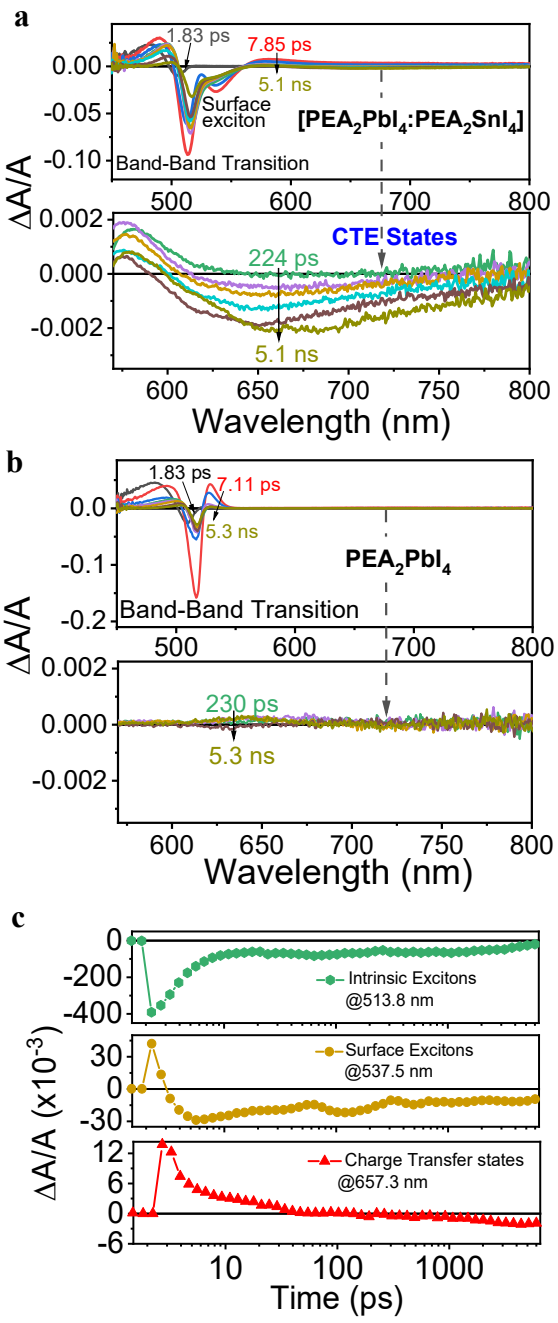


Figure 2- 5 Transient absorption (TA) characteristics for 2D perovskite heterostructures and PEA_2PbI_4. (a) TA spectra for 2D perovskite heterostructured $[(PEA_2PbI_4)_{0.95}:(PEA_2SnI_4)_{0.05}]$ film. (b) TA spectra for pristine PEA_2PbI_4 film. (c) TA dynamics plotted for band-to-band transition (513.8 nm), surface excitons (537.5 nm) and broad emission (657.3 nm) in 2D perovskite heterostructures.

assigned the TA spectral shoulder (peaked at 537.5 nm) to surface-trapped excitons. Because the CTEs are developed into a bleaching signal after 230 ps, the surface-trapped excitons which are quickly shown a bleaching signal within 2.2 ps can have an opportunity to contribute to the formation of CTEs. Furthermore, the surface-trapped excitons have a limited light emission in our 2D perovskite heterostructured film. It is shown that the PL of pure PEA_2PbI_4 film contains a weak tail located around 540 nm, slightly below the emission (peaked at 520 nm) from intrinsic excitons with decreased film thickness (~20 nm), leading to an asymmetric spectrum. This weak PL tail at 540 nm coincides with the surface-trapped excitons at 537.5 nm shown in transient absorption (**Figure 2-5a**). With increasing the film thickness to ~150 nm, this weak tail becomes negligible, making the entire PL spectrum symmetric. We believe this weak tail on PL spectrum at thinner film provides a further indication to support the surface-trapped excitons. As a comparison, the intrinsic excitons shown as the band-to-band transition peaked at 513.8 nm are quickly developed into a light emission within ~ 1 ps. Therefore, the dynamics of CTEs include the following three processes. First, both intrinsic and surface-trapped excitons experience a quick charge transfer, leading to the formation of CTEs at the heterointerfaces between host and guest perovskite structures within 3 ps. Second, the CTEs formed at heterostructures gradually develop a broad light emission, showing a TA bleaching signal after 230 ps. Third, the light emission of CTEs exhibits an extended lifetime (~0.5 μs), indicating that the CTEs are metastable states in 2D perovskite heterostructured film. To further verify the formation of CTEs, we have also measured TA for the double-layered heterointerfaces prepared by our hand-finger pressing method. The double-layered heterointerfaces demonstrate a broad TA signal between 640 nm and 800 nm, in addition to the band-to-band transitions (peaked at 520 nm and 590 nm) in Pb and Sn perovskites. This broad TA signal observed from the double-layered heterointerfaces prepared by our hand-finger pressing method provides a further evidence to confirm the formation of CTEs.

2.4.4 Heterostructured 2D perovskite photodetectors and LEDs.

Now we use below-bandgap photoexcitation to show that the CTEs are vital states formed in 2D perovskite heterostructures. **Figure 2-6a** illustrates the photocurrents for pristine (PEA_2PbI_4, PEA_2SnI_4) and heterostructured [$(PEA_2PbI_4)_{0.95}$:$(PEA_2SnI_4)_{0.05}$] films with the device architecture of ITO/PEDOT:PSS/perovskite/$PC_{61}BM$/PEI/Ag under the photoexcitation of 640 nm. We should note that the 2D heterostructured [$(PEA_2PbI_4)_{0.95}$:$(PEA_2SnI_4)_{0.05}$] and the pristine PEA_2PbI_4 film

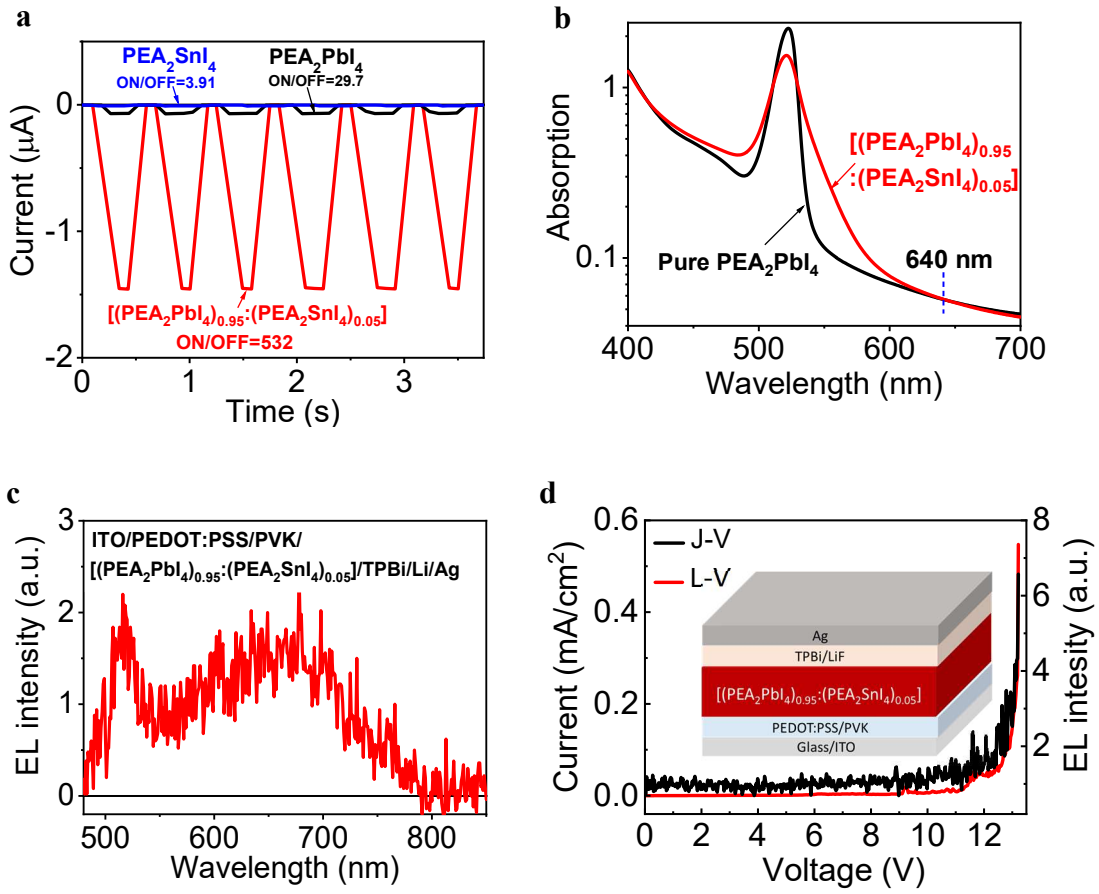


Figure 2- 6 Device performance of photodetectors and LEDs for 2D perovskite heterostructures. (a) The ON-OFF behaviors of heterostructured 2D perovskite $[(PEA_2PbI_4)_{0.95}:(PEA_2SnI_4)_{0.05}]$ photodetector (red) as compared to pure PEA_2PbI_4 (black) and PEA_2SnI_4 (blue) devices when exciting at 640 nm (1000 mW/cm^2). (b) Absorption spectra of two films. (c) EL spectrum containing broad CTEs emission and host emission. (d) Current density-voltage-EL curve of doped device. The device structure is shown as the inset.

have the same absorbance at the wavelength of 640 nm (selected as the below-bandgap photoexcitation) (**Figure 2-6b**). Interestingly, the heterostructured [$(PEA_2PbI_4)_{0.95}$:$(PEA_2SnI_4)_{0.05}$] film demonstrates a much enlarged ON-OFF ratio of 532 on the photocurrent when the 640 nm photoexcitation is applied and removed periodically. This below-bandgap photoexcitation-induced photocurrent directly indicates that the charge-transfer states are vital states formed in 2D perovskite heterostructures. On contrast, both pristine PEA_2PbI_4 and PEA_2SnI_4 films show significantly reduced ON-OFF ratios of 29.7 and 3.91 on photocurrent upon repeatedly applying and removing the 640 nm photoexcitation.

Furthermore, we observed that the CTEs can be generated by electrically injected charge carriers in 2D perovskite heterostructures. **Figure 2-6c** shows the electroluminescence (EL) spectrum from the heterostructured 2D perovskite [$(PEA_2PbI_4)_{0.95}$:$(PEA_2SnI_4)_{0.05}$] film based on the device design of ITO/PEDOT: PSS/PVK/perovskite/TPBi/LiF/Ag. The EL spectrum combines the emission from both intrinsic excitons (peaked at 517 nm) from the host PEA_2PbI_4 component and the CTEs (peaked at 669 nm) formed at the interfaces between PEA_2PbI_4 and PEA_2SnI_4 components in 2D perovskite heterostructures [$(PEA_2PbI_4)_{0.95}$:$(PEA_2SnI_4)_{0.005}$]. The EL-voltage-current characteristics shown in **Figure 2-6d** indicate the typical LED behaviors from CTEs under electrical injection. It should be pointed out that, the injection current is quite low: (< 1 mA/cm^2) due to the lower conductance caused by insulating organic long-chain ligands in 2D perovskite film even when the applied bias reaches 13 V. Clearly, the CTEs allow the generation of broad EL in 2D perovskite heterostructures under electrical injection.

2.5 Summary

In summary, we found that the CTEs can be formed at the interfaces between PEA_2PbI_4 and PEA_2SnI_4 components in 2D perovskite heterostructures [$(PEA_2PbI_4)_{1-x}$:$(PEA_2SnI_4)_x$] prepared by chemically mixing two precursor (PEA_2PbI_4 and PEA_2SnI_4) solutions. The PEA_2PbI_4 and PEA_2SnI_4 serve as host and guest components in the heterostructured 2D perovskite [$(PEA_2PbI_4)_{0.999}$:$(PEA_2SnI_4)_{0.001}$] films. A broad emission peaked at 669 nm with spectral range between 575 nm and 800 nm was observed with the intensity-dependence slope of 1.62 and the prolonged lifetime (~ 0.5 μs) in such 2D perovskite heterostructures. Particularly, when the host and guest components are alternatively switched to shift the bandgap largely from 2.33 eV in the [$(PEA_2PbI_4)_{0.999}$:$(PEA_2SnI_4)_{0.001}$] to 1.95 eV in the [$(PEA_2SnI_4)_{0.999}$:$(PEA_2PbI_4)_{0.001}$], the broad

emission spectrum is only slightly changed from 669 nm (1.85 eV) to 697 nm (1.78 eV) in peak position, leading to similar broad emission between PEA_2PbI_4 and PEA_2SnI_4 based heterostructures. This leads to the hypothesis that the CTEs can be conveniently established in 2D perovskite heterostructures. This hypothesis was verified by the unique phenomenon: a similar broad emission can be reproduced when the PEA_2SnI_4 film was shearing-away onto the surface of the PEA_2PbI_4 film by hand-finger pressing method. The pump-probe transient absorption studies show that the CTEs are formed within 3 ps between PEA_2PbI_4 and PEA_2SnI_4 components and slowly developed into a photobleaching signal after 230 ps. Particularly, the photobleaching signal from CTEs extends a few nanoseconds without appreciable decay. Essentially, the CTEs become metastable states in 2D perovskite heterostructures. The photocurrent generated by below-gap photoexcitation shows that the charge-transfer states are vital states formed at the interfaces between PEA_2PbI_4 and PEA_2SnI_4 components in heterostructured 2D perovskite films. The EL indicates that the CTEs can be formed by electrically injected electrons and holes to generate a broad light emission in perovskite LEDs. Therefore, the CTEs present new opportunities to develop advanced optoelectronic properties based on heterostructural design in 2D perovskites.

Chapter 3 Doping Induced Orbit-orbit Interaction between Excitons while Enhancing Photovoltaic Performance in Tin Perovskite Solar Cells

3.1 Abstract

Doping has been used as a common method to improve photovoltaic performance in perovskite solar cells (PSCs). This paper reports a new phenomenon that the SnF_2 doping can largely increase the exciton-exciton interaction through orbital magnetic dipoles towards increasing dissociation probabilities in lead-free $FASnI_2Br$ PSCs. Essentially, when orbit-orbit interaction between excitons occurs, linearly and circularly polarized photoexcitations can inevitably generate different photocurrents, giving rise to a ΔJsc phenomenon. Here, it is found that, when SnF_2 doping is used to boost photovoltaic efficiency to 7.61 %, the orbit-orbit interaction is increased by a factor of 2.2, shown as the ΔJsc changed from 1.21 % to 0.55 %. Simultaneously, magnetic field effects of Jsc indicate that increasing orbit-orbit interaction leads to an increase on the spin-orbital coupling in Sn perovskite ($FASnI_2Br$) upon SnF_2 doping. This presents a new doping effect occurring in Sn perovskite solar cell towards enhancing photovoltaic efficiency.

3.2 Introduction

Doping has been known as an important method to improve photovoltaic performance in perovskite solar cells, which can effectively decrease defects formed in polycrystalline perovskites.[118-123] It is reported that the SnF_2 doping in Sn based perovskites can effectively suppress the oxidation of $Sn^{2+} \rightarrow Sn^{4+}$ and/or decreased Sn vacancy concentration, resulting in the largely reduced defects and directly suppressed photovoltaic loss of non-radiative recombination.[56-62] In addition, intensive research efforts have been made to reduce defects towards boosting power conversion efficiency (PCE) in Pb-free Sn based perovskite solar cells by incorporating hierarchy structure (9.41%),[124] controlling the grain orientation (PCE=10.16%),[125] introducing Lewis acid post-treatment (PCE=10.18%)[126] and regulating cations (PCE=13.24%).[127] However, it still remains challenging to achieve high-efficiency Sn perovskite solar cells due to the weak orbital momentum, which limits the conversion and dissociation of photogenerated excited states.[19]

Notably, organic-inorganic hybrid perovskites possess both orbital **L** and spin **S** momentums with the total momentum **J** = **L** + **S**, leading to bright (**J** = 1; $|\Psi_{1,+1}\rangle$, $|\Psi_{1,0}\rangle$ and $|\Psi_{1,-1}\rangle$) and dark (**J** = 0; ($|\Psi_{0,0}\rangle$) states with allowed and forbidden transitions.[18,20,26] As discovered

by our previous experimental results, the population between bright and dark states can be tuned through magnetic field effects or exciton-exciton interaction, which may cause a change on photocurrent in perovskite solar cells.[19,20] Exciton binding energy is usually very low in 3D perovskites, which can easily to dissociate into free carriers. However, these free electrons and holes can form bond electron hole pairs through Coulomb attraction towards excitons, evidenced by magnetic field effects of photoluminescence and photocurrent. Specifically, the exciton-exciton interaction can occur through the interaction between orbital magnetic dipoles, leading to more optically generated bright states (spin-allowed to recombine) converted to dark states (spin-forbidden to recombine). Therefore, stronger exciton-exciton interaction will lead to more dark states, resulting in increased Jsc.

On the other hand, the hybrid perovskites possess a strong interaction between electrical and spin polarizations to demonstrate an electrical-magnetic coupling phenomenon.[21-25] Essentially, the orbit-orbit interaction between excitons can occur through orbital magnetic dipoles or orbital polarizations, forming short-range and long-range orbit-orbit interactions between excitons.[26] It should be pointed out that tuning the orbit-orbit interaction plays an important role in determining the photovoltaic performance, but it remains an unexplored field on whether doping effect can affect the orbit-orbit interaction.

Here, we explore the orbit-orbit interaction between excitons when doping is used to improve the photovoltaic efficiency in lead-free Sn perovskite solar cells. The orbit-orbit interaction between excitons was identified by monitoring the change of photocurrent (ΔJsc) while switching the photoexcitation between linear and circular polarizations. Note that, linearly/circularly polarized light generates bright excitons with opposite/same directional orbital magnetic dipoles, leading to low/high total orbit momentums. Thus, less/more dark states will be converted through orbit-orbit interaction, resulting in low/high photocurrent, i.e. ΔJsc.

In the present work, it is the first time to verify that SnF_2 doping in the Sn perovskites ($FASnI_2Br$) can lead to largely enhanced orbit-orbit interaction via polarization dependent photocurrent and magneto-photocurrent characteristics with the device architecture of ITO/PEDOT:PSS/$FASnI_2Br$/$PC_{61}BM$/PEI/Ag. This work has been published (*Journal of Physical Chemistry Letters 11*, 6996-7001, 2020).

3.3 Materials and Methods

3.3.1 Materials and Device fabrication

Formamidinium bromine (FABr, 99%) and PEDOT:PSS (Clevious PVP AI 4083) were purchased from Xi'an Polymer Light Technology Corp (PLT). Tin (II) iodide (SnI_2, 99.999%), Tin (II) Flouride (SnF_2, 99%) and Polyethylenimine (PEI) (branched, M=20,000) were purchased from Sigma Aldrich. All the materials were used as received.

Devices studied in this work were fabricated with an inverted structure of ITO/PEDOT:PSS/perovskite/$PC_{61}BM$/PEI/Ag. The precursor solutions for $FASnI_2Br$ were prepared by dissolving SnI_2 (1.3 M) with FABr (1.0 M) in a mixture solvent of γ-butyrolactone (GBL): dimethyl sulfoxide (DMSO) (7:3, v/v). Then 10 mol% SnF_2 was added or not to the solutions. The mixture solutions were kept in dark condition for at least 2 hours to get all compounds fully dissolved. The PEDOT: PSS thin films were spin-coated, from solution filtered with 0.22 μm PVDF filter, on the pre-cleaned ITO/glass substrates at 4000 rpm for 60 s and then annealed at 150 ℃ for 30 min on a hot plate in ambient environment. The perovskite precursor solutions were spin coated onto PEDOT: PSS film using a two-step spin-coating process at 1000 rpm for 10s and 4000 rpm for 47s, and 400 μL of toluene was dropped onto the perovskite films as anti-solvent at the last 20^{th} second. These films were then annealed at 90℃ for 20 min. After cooling down, phenyl-C_{61}-butyric acid methyl ester ($PC_{61}BM$, 20 mg/mL in chlorobenzene) was spin-cast on top of perovskite films at 2000 rpm for 50 s. The films are kept in dark for at least 30 min, and then an interface-modifying layer PEI (0.1 wt%, in anhydride 2-Propanol) at 5000 rpm for 60 s. Finally, 90-nm-thick silver top electrodes were thermally evaporated on top of the film through metal mask under a vacuum of 2×10^{-4} Pa. The active area of the devices is 0.06 cm^2.

3.3.2 Characterizations and Measurements

The I–V characteristics were recorded by using Keithley 2400 source meter under illumination of AM 1.5G 100 mW/cm^2 from Newport solar simulator calibrated by a silicon reference cell. The absorption spectra were recorded using UV3600 (Shimadzu, Japan). The external quantum efficiency (EQE) spectra were measured by a hand-made system. The cells were subjected to monochromatic illumination (300 W Xe lamp passing through a monochromator and

appropriate filters). The light intensity was calibrated by a standard Si biased photodetector (DET100A, 350 nm-1100 nm, Thor Labs). The light beam was chopped at 230 Hz and the response of the cell was acquired by a Stanford Research SR830 lock-in amplifier. Magneto-photocurrent measurements were conducted by recording photocurrent (Jsc) as a function of magnetic field up to ~900 mT (parallel to device plane). The magnetic field was applied parallel to the device plane while using 488 nm CW laser as a photoexcitation. Photocurrent was monitored by Keithley 2400 source meter under short-circuit condition upon switching the photoexcitation between linear and circular polarizations at same intensity (148 mW/cm^2) and wavelength(405nm). Essentially, as schematically shown in our previous work[19], the circularly polarized light was converted from linearly polarized 405 nm CW laser beam perpendicularly through a λ/4 wave plate at 45°. Also, a commercial silicon solar cell was used as the reference to ensure no change generated in light reflection with the optical path. Meanwhile, the light intensity dependent Jsc and Voc was measured with neutral density filters stacked on the devices to modify the light intensity. The C-f and C-V measurements were performed by using a dielectric spectrometer (Agilent, 4294A) with alternating voltage of 50 mV.

3.4 Results and Discussion

Figure 3-1a shows the experimental principle to identify the orbit-orbit interaction between excitons upon switching the photoexcitation between linear and circular polarizations. Circularly and linearly polarized photoexciations generate excitons with same-directional and opposite-directional orbital magnetic dipoles, respectively. If the exciton-exciton interaction is not occurred through orbit-orbit interaction, linearly and circularly polarized photoexcitations with identical intensity would generate same photocurrents because of same density of optically generated excitons. If the exciton-exciton interaction is occurred through orbit-orbit interaction, linearly and circularly polarized photoexcitations with identical intensity can then generate different photocurrents, leading to a ΔJsc phenomenon. We should note that the orbit-orbit interaction between excitons can occur through orbital magnetic dipoles or orbital polarizations (**Figure 3-1a**). When orbital magnetic dipoles dominate the orbit-orbit interaction between excitons, same-directional and opposite directional orbital magnetic dipoles generated by circularly and linearly polarized photoexcitations correspond to stronger and weaker SOC, respectively. Because SOC can serve as the underlying mechanism to flip spins to convert optically

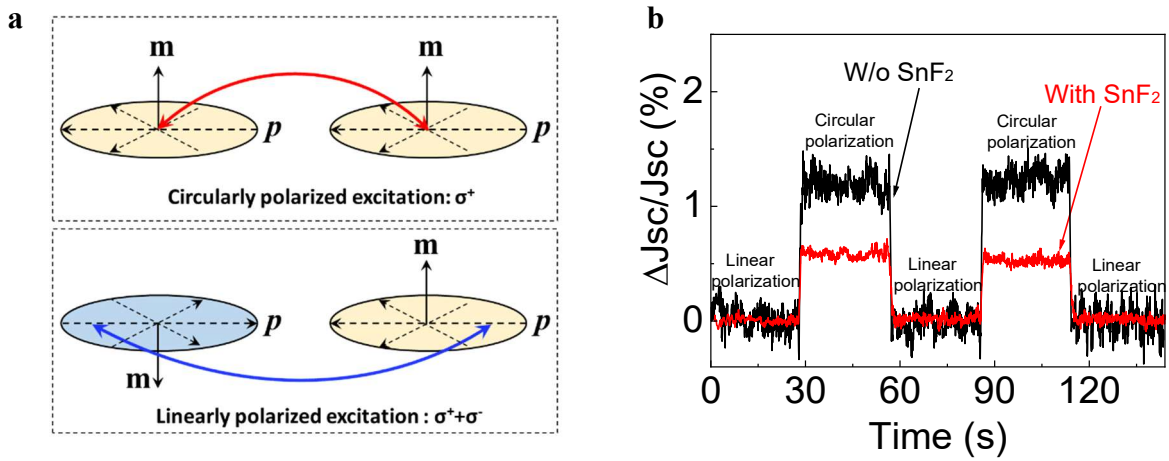


Figure 3- 1 Orbit-orbit interaction in $FASnI_2Br$ perovskites. (a) Schematic diagram to show the orbit-orbit interaction between excitons upon switching the photoexcitation between linear and circular polarizations (b) Photocurrent change of devices without and with SnF_2 doping by switching between linear and circular polarized photoexcitations (405 nm) at identical intensity (148 mW/cm^2).

generate bright states into dark states.[20,27] Circularly/linearly polarized photoexcitation can then generate larger/smaller photocurrent, presenting a +ΔJsc when switching the photoexcitation from linear to circular polarization. When orbital polarizations dominate the orbit-orbit interaction between excitons, the parallel and antiparallel orbital polarizations can be established by the same-directional and opposite-directional orbital magnetic dipoles, causing less and more dissociation due to dipole-dipole interaction. This leads to a -ΔJsc when switching the photoexcitation from linear to circular polarization at the situation where orbital polarizations dominate the orbit-orbit interaction between excitons. Therefore, monitoring the ΔJsc provides a unique experimental method to explore the orbit-orbit interaction between excitons in hybrid perovskites. We should point out that the ΔJsc phenomenon[28] is established when the optically-induced orbit-orbit interaction can compete with the intrinsic orbit-orbit interaction already-existed before photoexcitation. If the optically-induced orbit-orbit interaction is much weaker than intrinsic orbit-orbit interaction, ΔJsc become negligible.

Clearly, larger/smaller ΔJsc corresponds to weaker/stronger intrinsic orbit-orbit interaction. **Figure 3-1b** shows the ΔJsc results before and after the SnF_2 doping in the Sn perovskite solar cell [ITO/PEDOT:PSS/$FASnI_2Br$/$PC_{61}BM$/PEI/Ag] measured by switching the photoexcitation from linear to circular polarization. Here we can see two interesting information. First, the +ΔJsc observed by switching the photoexcitation from linear to circular polarization indicates that the orbital magnetic dipoles are indeed dominated the orbit-orbit interaction between excitons. Second, the SnF_2 doping causes a large reduction on the +ΔJsc value from 1.21 % to 0.55 % by a factor of 2.2. This presents a new phenomenon that the SnF_2 doping can increase the intrinsic orbit-orbit interaction through orbital magnetic dipoles while the photovoltaic efficiency is improved in Sn perovskite solar cells.

Now we discuss the SOC upon increasing the orbit-orbit interaction through magnetic dipoles in Sn perovskite solar cell under SnF_2 doping by using magnetic field effects of Jsc, namely magneto-Jsc. Our early studies have shown that magneto-Jsc can be observed in hybrid perovskite solar cells when an external magnetic field can disturb the intersystem crossing from optically generated bright states (J = 1) into dark states (J = 0).[20] Essentially, magnetic field effects of Jsc is established when an external magnetic field competes with intrinsic SOC towards controlling the intersystem crossing from optically generated bright states to dark states.[29] If an external magnetic

field is not able to compete with intrinsic SOC, magneto-Jsc become negligible. If an external magnetic field is able to compete with intrinsic SOC, magneto-Jsc can then be observed. Therefore, magneto-Jsc can reflect intrinsic SOC characteristics. Here, the line-shape of magneto-Jsc characterized by internal magnetic parameter (B_0) can be used to estimate the intrinsic SOC. Large/small internal magnetic field (B_0) provides high/low resistance for magnetic field to change the intersystem crossing. Therefore, when the intersystem crossing becomes higher, it is more difficult to disturb the equilibrium between optically generated bright states to dark states, broadening the line-shape in magneto-Jsc characteristics. We can see in **Figure 3-2** that magneto-photocurrent shows narrower and broader line-shapes before and after the SnF_2 doping. By using the non-Lorentz equation $\frac{\Delta Jsc(B)}{Jsc(0)} \propto \frac{\boldsymbol{B}}{(|\boldsymbol{B}|+\boldsymbol{B_0})^2}$, the curve fitting shows that the internal magnetic parameter B_0 increases from 76 mT to 201 mT in the $FASnI_2Br$ upon doping SnF_2. This provides a further information that the SnF_2 doping can indeed increase the intrinsic SOC upon increasing the orbit-orbit interaction through orbital magnetic dipoles in Sn perovskite ($FASnI_2Br$). Here, it should be clarified that the SOC can generally exist in both ground and excited states. The SOC in ground states is irrelevant to the situation before applying photoexcitation. In our work, we focus on the SOC in excited states. Our ΔJsc results upon switching photoexcitation between linear and circular polarizations (**Figure 3-1b**) indicates that the SOC in excited states contains the contribution from orbit-orbit interaction. This is reflected by the different populations of bright and dark states under linearly and circularly polarized photoexcitations at same intensity, observed as ΔJsc phenomenon.

Note that, the SnF_2 doping has been used as a common procedure to enhance the photovoltaic efficiency in Sn perovskite solar cell by passivating the grain boundary defects and stabilizing morphological structure. The concentration of SnF_2 doping is optimized in view of best photovoltaic performance as shown in **Figure 3-3** and **Table 3-1**. Here, the doping concentration was tuned from 0% to 20%. Obviously, the SnF_2 is proved to be beneficial for achieving high device performance, through enhancing all three photovoltaic parameters: Jsc, Voc and FF. Especially, the optimal concentration is 10%, which is the best choice for evaluating the doping induced orbit-orbit interaction. **Figure 3-4a** shows the current-voltage (I-V) characteristics for the device [ITO/PEDOT:PSS/perovskite/$PC_{61}BM$/PEI/Ag] with (10%) and without SnF_2 doping. As summarized in **Table 3-2**, doping the SnF_2 can largely increase the device efficiency from 2.07 %

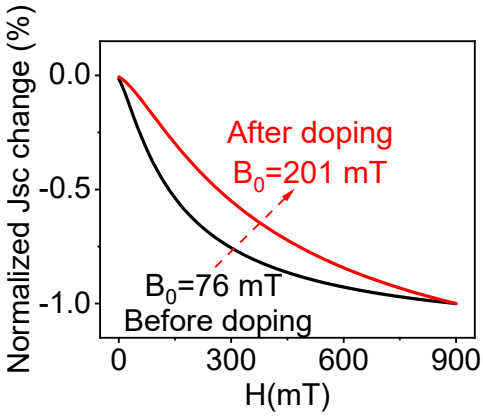


Figure 3- 2 Normalized magneto-photocurrents curves. The internal magnetic parameter B_0 was derived from Lorentizan function in Sn based perovskite solar cells with or without doping.

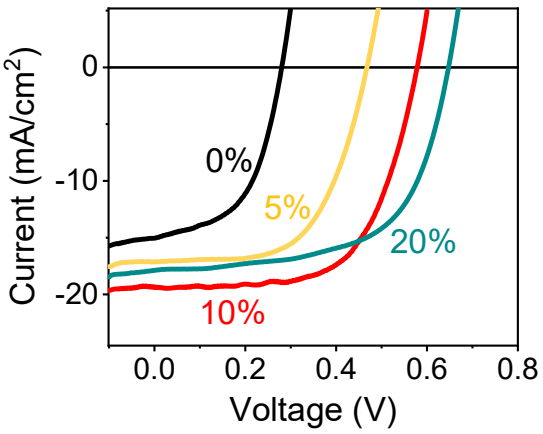


Figure 3- 3 Current-voltage characteristics measured under 1 sun condition $FASnI_2Br$ perovskite solar cells ([ITO/PEDOT:PSS/$FASnI_2Br$/$PC_{61}BM$/PEI/Ag]) with different doping concentration of SnF_2.

Table 3-1. Photovoltaic parameters for $FASnI_2Br$ perovskite solar cells with different doping concentration of SnF_2.

Doping concentration	Jsc (mA/cm^2)	Voc (V)	Fill factor (%)	PCE (%)
0%	14.87	0.27	51.5	2.07
5%	17.13	0.47	59.5	4.79
10%	19.82	0.60	64.0	7.61
20%	17.89	0.65	61.4	7.10

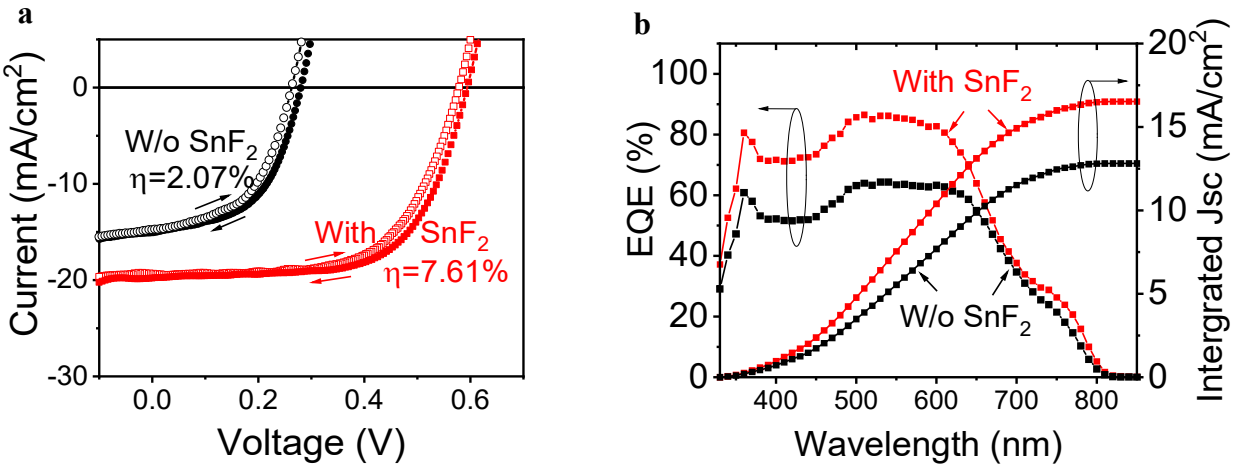


Figure 3- 4 Photovoltaic performance of Sn perovskites with and without SnF_2 doping. (a) Current-voltage characteristics measured under 1 sun condition for Sn solar cell [ITO/PEDOT:PSS/$FASnI_2Br$/$PC_{61}BM$/PEI/Ag]. (b) EQE spectra.

Table 3-2. Photovoltaic parameters for doped and undoped Sn perovskite solar cells.

	Jsc (mA/cm^2)	Voc (V)	Fill factor (%)	PCE (%)
W/o doping	14.87	0.27	51.5	2.07
With doping	19.82	0.60	64.0	7.61

to 7.61 %, the Jsc from 14.87 mA/cm^2 to 19.82 mA/cm^2, Voc from 0.27 V to 0.60 V, and fill factor from 51.5 % to 64.0%. The maximal value of external quantum efficiency (EQE) increases from 64.0% to 86.5%, according to **Figure 3-4b** upon the SnF_2 doping at a concentration of 10%.

To get further insight of the dynamical excited states spin conversion development during efficiency improvement by doping method. We first evaluate the density of defects in Sn perovskite ($FASnI_2Br$) upon SnF_2 doping. The impedance studies show that the SnF_2 doping largely decreases the shallow defects in the $FASnI_2Br$ (**Figure 3-5a**). The density of defects is decreased by a magnitude of 1 at the doping concentration of 10 %. We also conducted the time-resolved photoluminescence characteristics to understand the carrier recombination dynamics in $FASnI_2Br$ films with and without SnF_2 doping. As shown in **Figure 3-5b** and **Table 3-3**, the PL decay traces are fitted with bi-exponential law and prolonged PL lifetime with much boosted bimolecular recombination are observed after SnF_2 doping which further proves that the doing effects indeed largely decease defect density.

In general, excitons are the primary excited states generated in hybrid perovskites under photoexcitation. Because an exciton carries both orbital and spin momentums, the exciton-exciton interaction can be developed through orbital polarizations and orbital magnetic dipoles, leading to two-types of orbit-orbit interactions between excitons, namely electric-type orbit-orbit interaction dominated by orbital polarizations and magnetic-type orbit-orbit interaction dominated by orbital magnetic dipoles within grains in hybrid perovskite films, as schematically illustrated in **Figure 3-6a**. We should note that, when the internal polarization from dipolar and ionic polarization provides a Coulomb screening effect, the electric-type orbit-orbit interaction can be suppressed. In this case, the magnetic-type orbit-orbit interaction through orbital magnetic dipoles becomes a dominant component in the interaction between excitons. Because the orbital magnetic dipoles can function as the basic mechanism to flip the spins, the magnetic-type orbit-orbit interaction can essentially increase the intersystem crossing from optically generated bright (J = 1) states to dark (J = 0) states, changing the populations on bright and dark states. Based on allowed and forbidden recombination, dark and bright states can have higher and lower probabilities to dissociate into free charge carriers, leading to larger and smaller Jsc values. The magnetic-type orbit-orbit interaction can be identified as $+\Delta$Jsc upon switching the photoexcitation from linear to circular polarization.[26] On the other hand, when the internal polarization does not cause an appreciable

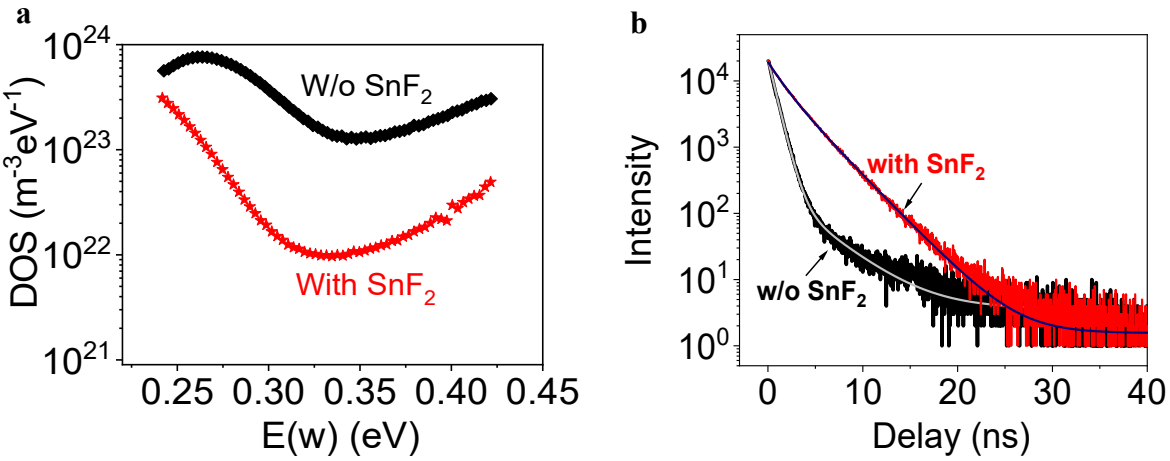


Figure 3- 5 Reduced defect density through SnF_2 doping. (a) Density of trap states (tDOS) deduced from C-f and C-V data at room temperature for doped and undoped devices. (b) Time-resolved photoluminescence characteristics of $FASnI_2Br$ films with and without SnF_2 doping and the solid lines are obtained by fitting the decay traces with a bi-exponential law. The fitted data are shown in **Table 3-3**.

Table 3-3. Fitted parameters of PL lifetime for $FASnI_2Br$ films with and without SnF_2 doping.

Samples	t_1 (ns)	ratio	t_2 (ns)	Ratio	t_{av} (ns)
With doping	1.4	45%	3	55%	2.3
Without doping	0.7	99%	3.9	1%	0.8

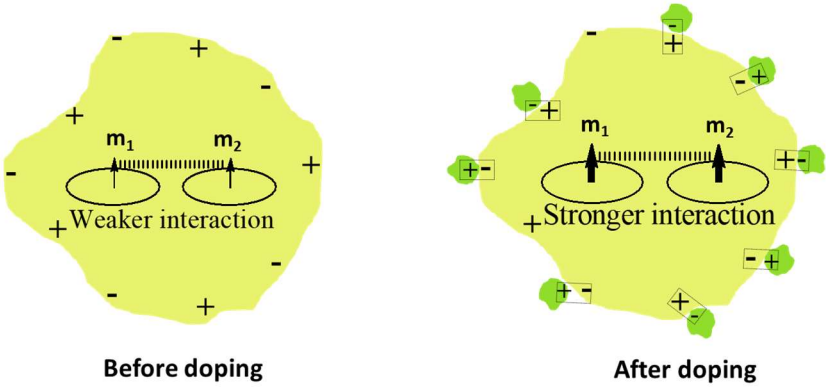


Figure 3- 6 Schematic drawing to show the doping effects on orbit-orbit interaction.

Coulomb screening effect, the electric-type orbit-orbit interaction through orbital polarization becomes a dominant component in the interaction between excitons. In this case, the interaction between orbital polarizations plays an important role to determine the exciton dissociation. This can be identified as a -ΔJsc upon switching the photoexcitation from linear to circular polarization.[26] Here, we observed a +ΔJsc in Sn perovskite soar cell [ITO/PEDOT:PSS/perovskite/$PC_{61}BM$/PEI/Ag] by switching the photoexcitation from linear to circular polarization. This +ΔJsc indicates that the magnetic-type orbit-orbit interaction dominates the interaction between excitons in Sn perovskite. More importantly, we found that the SnF_2 doping can largely increase the magnetic-type orbit-orbit interaction between excitons, according to doping-decreased ΔJsc results shown in **Figure 3-1b**. This indicates that, when the SnF_2 doping passivates the grain boundary defects, the interaction between orbital magnetic dipoles can be increased within grains in Sn perovskite film. This means that the charged defects can partially destroy the interaction between orbital magnetic dipoles between excitons. Decreasing the charged defects can essentially increase the interaction between orbital magnetic dipoles, increasing the SOC in Sn perovskite solar cell, as schematically illustrated in **Figure 3-6b**. Furthermore, other additives such as NH_4SCN have been reported to manipulate the local crystalline structures of Sn perovskite film [124, 128], which may also suppress the charged defects at the grain boundaries and deserve further investigations in the future.

3.5 Summary

In summary, our studies show that the exciton-exciton interaction is occurred in lead-free Sn perovskite solar cell, identified by +ΔJsc upon switching the photoexcitation from linear to circular polarization. This magnetic-type orbit-orbit interaction provides a spin flipping mechanism to convert optically generated bright states to dark states in Sn perovskite. Because allowed and forbidden recombination, increasing the intersystem crossing from optically generated bright states to dark states can lead to an increase on Jsc. More importantly, we found that, when the SnF_2 doping is used to enhance the photovoltaic efficiency from 2.07 % to 7.61 % in Sn perovskite solar cells, the magnetic-type orbit-orbital interaction can be largely increased by a factor of 2.2, shown as the decreased ΔJsc from 1.21 % to 0.55 %. Simultaneously, our magneto-Jsc results indicate that increasing the magnetic-type orbit-orbit interaction can directly increase the SOC in Sn perovskite. Our analysis indicates that the charged defects can suppress the

interaction between orbital magnetic dipoles within grains in Sn perovskite. When the charged defects are decreased by SnF_2 doping, the magnetic-type orbit-orbit interaction can be consequently increased while the photovoltaic efficiency is enhanced. This presents a new phenomenon occurring in Sn perovskite solar cell when doping is used to enhance the photovoltaic efficiency.

Chapter 4 Slow hot-carrier cooling and long-order orbital interaction enabled by uniformly arranging different-n-value nanoplates in quasi-2D perovskites

4.1 Abstract

Long-chain organic ligands are frequently incorporated to halide perovskites to form different-n-value nanoplates, leading to improved environmental stabilities and substantially enriched optoelectronic properties. This paper reports that uniformly arranging different-n-value nanoplates can lead to slow hot-carrier cooling and long-order orbit-orbit interaction in quasi-2D perovskites. Specifically, when the different-n-value nanoplates are uniformly arranged in quasi-2D perovskite ($PEA_2MA_4Pb_5I_{16}$) by enforcing the crystallization with our vacuum-poling treatment, a slow cooling of hot carriers is clearly observed within the time window of 200 ps shown in transient absorption (TA) dynamics, leading to long-lived hot carriers. This slow hot-carrier cooling presents the signature of large polarons occurring in quasi-2D perovskite film by uniformly arranging different-n-value nanoplates. Furthermore, when the slow hot-carrier cooling is occurred, the orbit-orbit interaction is dominated by orbital polarizations, indicating that large polarons can enable a long-order orbital interaction. With the slow hot-carrier cooling and long-order orbital interaction, the quasi-2D perovskite demonstrates superior transport shown by high fill-factor values in solar cell at different carrier densities by varying light illumination intensity.

4.2 Introduction

Slow hot-carrier cooling is an interesting phenomenon towards controlling carrier transport and excited states dynamics in semiconductors. In conventional semiconductors, the hot-carrier cooling is normally occurred rapidly within 10s-100s of femtoseconds[129-131]. Interestingly, in hybrid perovskites, the hot-carrier cooling can be significantly slowed down to hundreds of picoseconds, indicating the formation of large polarons within crystalline structures[132 - 134]. Essentially, polarons are formed when electrons are coupled with phonons within a crystalline lattice through electron-phonon interaction. Normally, soft materials such as organic molecules can conveniently form polarons with spatially extended wavefunctions due to the nature of low dielectric constants that can initiate a strong interaction between electrons and local molecular vibrations[135]. Interestingly, the hybrid perovskites, known as high-dielectric materials are still formed with large polarons within organics mediated inorganic periodic structures. It has been found that large polarons can play dual important roles in developing optoelectronic properties in hybrid perovskites. First, it has been found that large polarons can cause a shielding effect on Coulomb scattering from lattice vibrations, consequently leading to defects-tolerable superfluid-

type transport towards developing high-performance devices[136]. Second, the large polarons are accompanied with slow hot-carrier cooling through phonon-modulated electron relaxation in conduction band. This presents a possibility to break Schockley-Quisser limit of photovoltaic efficiency in perovskite solar cells[137-139]. In general, large polarons can be quickly formed within femtoseconds and spatially extend to a few nanometer scales, functioning as metastable states with spatially extended wavefunctions, in hybrid perovskites[140]. This leads to a hypothesis that large polarons can develop a long-order orbit-orbit interaction, presenting a new tuning mechanism on the optoelectronic properties in hybrid perovskites.

In this work, we explore both slow hot-carrier cooling and orbit-orbit interaction in quasi-2D perovskites while controlling the dispersion of different-n-value nanoplates. It is known that incorporating the long-chain organic ligands into halide perovskites can effectively passivate the grain boundary defects by bonding with the grain surface dangling bonds [141-144]. When introducing the long-chain organic cations such as phenethylammonium (PEA^+) into $MAPbI_3$ halide perovskites, different-n-value 2D ($PEA_2MA_{n-1}Pb_nI_{3n+1}$ RPP) nanoplates are naturally formed with different amount of PEA^+. Thus, tuning the dispersion of PEA^+ to control the dispersion of different-n-value RPP nanoplates provides a convenient way to regulate the localized dielectric environment and defect screening. Here, hot-carrier cooling was studied by monitoring the relaxation of band-to-band transition in light-emitting centers, named as largest-n-value nanoplates by using pump-probe transient absorption. The orbit-orbit interaction was explored by characterizing photocurrent density (Jsc) while optically operating orbital polarization and magnetic dipoles with linearly and circularly polarized photoexcitations.

4.3 Materials and Methods

4.3.1 Materials Processing and Device Fabrication

The quasi-2D perovskite solar cells are fabricated with the same device architecture following our previous procedure. The quasi-2D perovskite films with transport layers are prepared by spin-coating PTAA (3mg/ml, toluene) or $PC_{61}BM$ (20mg/ml, chlorine) onto fully annealed perovskite layers at the speed of 2000 rpm for 50 s. Then the film with transport layers are thermally annealed at 60 ℃ for 10 minutes at a hot plate.

4.3.2 Characterizations and Measurements

The current-voltage (I-V) characteristics were recorded using Keithley 2400 source meter by using Keithley 2400 source meter under the illumination of AM 1.5G 100 mW/cm^2 from Newport solar simulator. The light illumination intensity is tuned by neutral density filters and calibrated by a Commercialized silicon reference cell. Transient absorption spectra were obtained by a Helios fire spectrometer (Ultrafast Systems LLC). The pump pulses of 343nm (28μW) were generated by a harmonic generator (Ultrafast Systems LLC, third harmonic), which was pumped by a Pharos laser (Light Conversion, 1kHz, 1030nm, 290fs). The 343 nm pump beam was focused into a point with the diameter of ~100 μm. The circularly polarized light was generated from linearly polarized 405 nm CW laser beam perpendicularly through a λ/4 wave plate to setup photoexcitation polarization-dependent photocurrent measurement, as shown in our previous work (). The setup for photoexcitation polarization-dependent photocurrent measurement was calibrated by commercial silicon solar cell to ensure the same intensity between linear and circular photoexcitations in optical path.

4.4 Results and Discussion

As schematically shown in **Figure 4-1a**, the uniform dispersion of RPP nanoplates is realized by using our previously reported vacuum poling technique[145], which facilitates the nucleation of the spin-cast liquid film prior to crystallization by instantaneously pump out the remanent solvent toward realizing uniform dispersion of different-n-value nanoplates. Specifically, with the uniform dispersion, all the small-n-value nanoplate have opportunities to directly contact with the largest-n-value nanoplates. And the charge transfer between different-n-value nanoplates occurs via two steps. First, the charge carriers from wide-bandgap small-n-value nanoplates are directly cascaded to adjacent narrow-bandgap largest-n-value nanoplates duo the ladder-like energy diagram Second, the largest-n-value nanoplates can serve as transport highway network to further bring the charge carriers to electrodes for collection. The uniform dispersion of different-n-value nanoplates and efficient charge transfer based on such dispersion are proved by systematical characteristics such as tape peeling based photoluminescence monitoring, energy-dispersive X-ray spectroscopy analysis and transient absorption comparison between bottom and top surfaces in our previous work[145]. As shown in **Figure 4-1b**, based on the efficient charge transfer through uniformly arranging different-n-value nanoplates, the quasi-2D perovskite solar

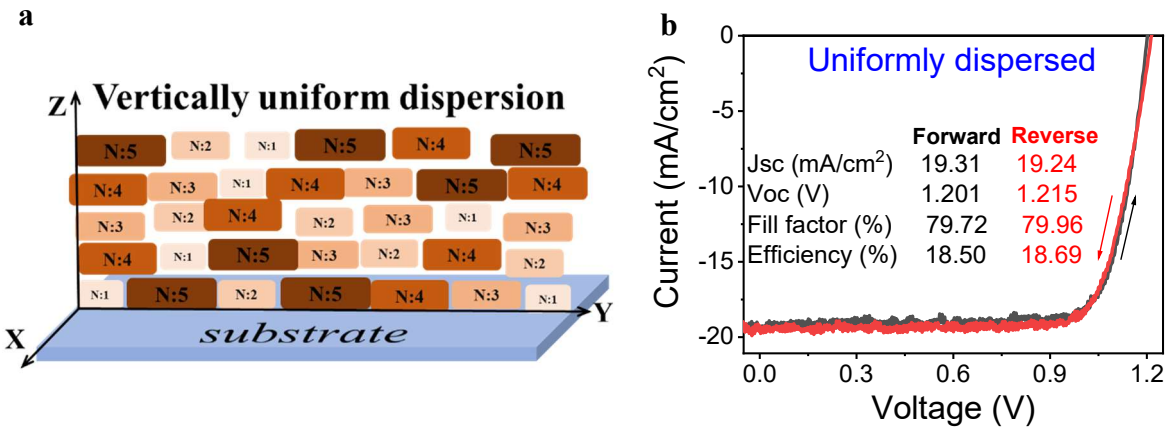


Figure 4- 1 Schematic diagram and optical characteristics of quasi-2D perovskite solar cells with uniformly dispersed nanoplates. (a) Spatial arrangement of uniform dispersed nanoplates. (b) Current-voltage characteristics for device with uniformly distributed nanoplates.

cell with a device architecture of ITO/PTAA/$PEA_2MA_{n-1}Pb_nI_{3n+1}$/$PC_{61}BM$/PEI/Ag exhibit an excellent power conversion efficiency (PCE) of 18.69% with Voc = 1.215 V, Jsc = 19.24 mA/cm^2 and FF = 79.96 %. The relatively low short circuit photocurrent is limited by the insulting nature of the PEA^+ ligands. And the high open circuit voltage and fill factor together with the minor hysteresis between forward and reverse scans further indicate that the quasi-2D perovskite films is of high quality and efficient charge transportation.

Next, we explore the dynamics evolution of excited states during the development of photovoltaic actions. As discussed previously, the long-live hot carriers imply the existence of a large polaron that can be considered as an electron carrying a spatially extended wavefunction, which provides the precondition for the formation of long-order orbital interaction between excited states. Here, transient absorption (TA) characteristics are carried out to track hot carrier dynamics in the uniform dispersed quasi-2D perovskite films. It is shown in **Figure 4-2a** that the film experience charge transfer process from small to large-n nanoplates during the delay time between 0.5–10 ps. The charge transfer process is effectively finished at around 7 ps, then the carriers that are transferred to largest n nanoplates experience a very slow hot carrier cooling process (shown in **Figure 4-2b**). The hot carrier cooling dynamics is obtained by tracking the PB peak energies at different delay time. As shown in **Figure 4-2c**, very slow hot carrier cooling process for uniformly dispersed quasi-2D perovskite films was observed. With exponential fitting, the uniformly dispersed film shows much longer cooling time of 91.7 ps. The significantly slowed down cooling process implies large volume polaron exists in the uniformly dispersed quasi-2D perovskite film.

In order to figure out which type of carriers responsible for slow hot carrier cooling, i.e. hot electrons or hot holes, we characterized the TA dynamics of our quasi-2D perovskite films after spin-casting an electron transport layer (ETL, Bphen) or a hole transport layer (HTL, PTAA). Both ETL and HTL were coated onto the perovskite layer, which enables the same crystallinity of quasi-2D perovskite films in different samples. As shown in **Figure 4-2c**, with an ETL, the perovskite film shows hot carrier cooling lifetime of 69.2 ps, which is faster than the film without coating transport layer. Since the electrons in the conduction band of perovskite can be extracted by ETL, the reduction of electrons is facilitated. Therefore, the faster cooling of hot carriers induced by ETL indicates that the hot carriers are electrons. To further verify our analysis, we characterize the TA dynamics of perovskite film after coating a HTL, which is used to extract

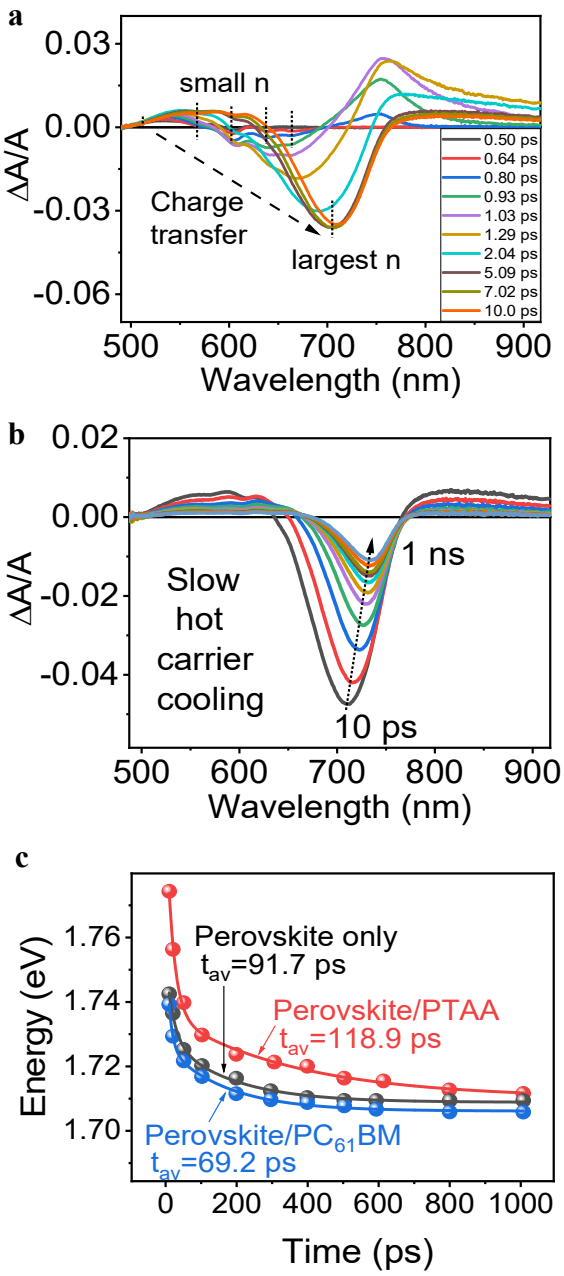


Figure 4- 2 Transient absorption (TA) spectra for quasi-2D perovskite ($PEA_2MA_4Pb_5I_{16}$) films with ordered and uniform distributed nanoplates. (a) TA spectra with delay time between 0.5-10 ps for films with uniformly distributed nanoplates. (b) TA spectra with delay time between 10-1000 ps for films with uniformly distributed nanoplates. (c) Dynamical changes of photoexcited carrier energy as a function of delay time for films of perovskite only (black), perovskite/PTAA (red) and perovskite/$PC_{61}BM$ (blue).

holes in the valance band. Interestingly, the hot carrier cooling lifetime is prolonged to 118.9 ps, which is much slower than the film without coating transport layer. Owing to the reduction of holes, the recombination loss will be reduced, leading to accumulation of electrons in the conduction band. The slowed hot carrier cooling feature proves that electrons in our perovskite films serve as hot carriers.

As schematically shown in **Fig 4-3**, the hot electrons in the conduction band can couple with surroundings to form polarons, leading to more extended wavefuctions as compared with free electrons. Therefore, the polarons are more difficult to be relaxed to the conduction band minimum, which results in prolonged cooling lifetime. Besides, it's known that polaron actually is an excess electron/hole dressed by polarization from nuclear coordinates, and large volume polarons are formed when long range Coulomb potential dominates. And the large volume polarons can be delocalized among multiple unit cells and is dynamically coherent. Thus, with the large volume polaron observed, higher orbital interaction is expected, which can be originated from long-order orbital interactions between polarizations in uniformly dispersed quasi-2D perovskite film.

As previously reported[18,19,28,146], photoexcitation polarization-dependent photocurrent is used to further characterize the orbital interaction of the quasi-2D perovskite film with uniform arranged nanoplates. **Figure 4-4a** shows that switching the photoexcitation from linear to circular polarization at the same intensity causes negative changes on Jsc in uniformly dispersed quasi-2D perovskite solar cells, leading to -ΔJsc phenomenon. Here, -ΔJsc represents long-order orbit-orbit interactions based on the following analysis. A linearly polarized photoexcitation, combining left-hand (σ^+) and right-hand (σ^-) polarized lights, excites the orbitals with opposite-directional orbital magnetic dipoles, which enables increased spin flipping from bright states to dark states through long-order orbital interaction as illustrated in **Figure 4-4b** and **4c**. Clearly, the quasi-2D perovskite films demonstrate long-order Coulomb interactions in the situations with uniformly dispersed RPP nanoplates, according to the observed -ΔJsc phenomenon. Particularly, this long-order Coulomb interaction provides an opportunity to enhance the spin mixing from bright states to dark states in the development of photovoltaic action in quasi-2D perovskites.

We should note that, large polarons enable more spatially extended wavefunction, resulting in efficient charge dissociation and transport regardless of external electric field. Thus, hign FF can be achieved, as evidenced by **Figure 4-1b** where uniform dispersed different-n-value

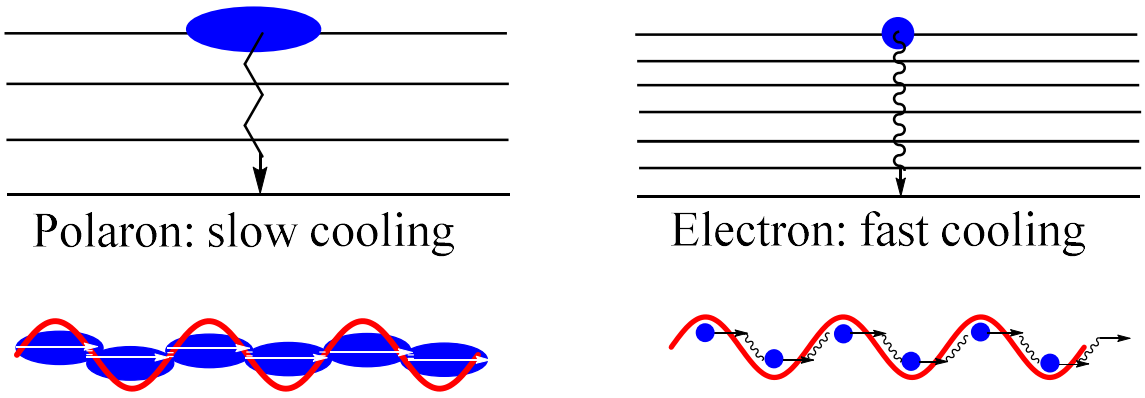


Figure 4- 3 Polarons enable slow cooling with lower transport barriers due to spatially extended wavefunctions within local lattice as compared to electrons with fast cooling and higher transport barriers due to localized wavefunctions.

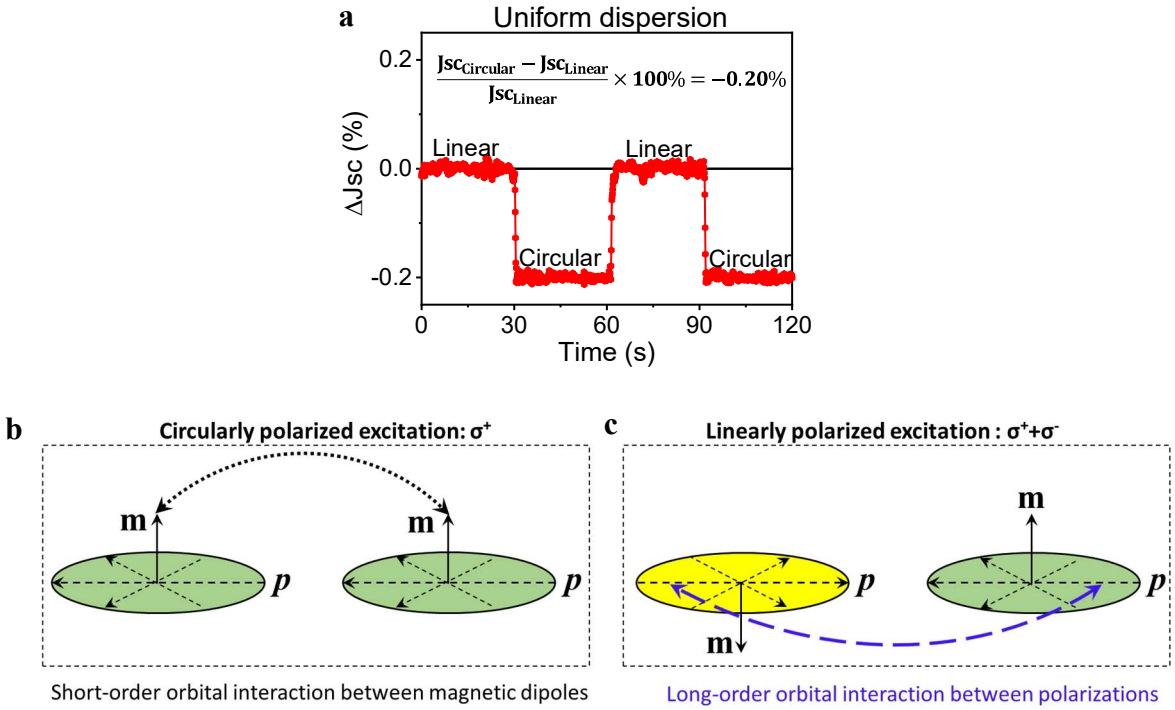


Figure 4- 4 Photocurrent change (ΔJsc) measured by switching photoexcitation from linear to circular polarization and principle diagrams to show long-order orbital interaction. (a) -ΔJsc observed from device prepared with uniformly distributed nanoplates to indicate long-order orbit-orbit Coulomb interaction. (b) Short-order orbital interactions between magnetic dipoles under circular photoexcitation. (c) Long-order orbital interactions between polarizations under linear photoexcitation.

nanoplates are demonstrated toward large polarons and long-lived hot carriers. We further compared current-voltage behaviors of the uniformly dispersed quasi-2D perovskite solar cells at different photoexcitation intensities to get further insight of significantly improved fill factor. As shown in the **Figure 4-5** and **Table 4-1**, for the uniform dispersed quasi-2D perovskites based solar cells, with decreasing the light illumination intensity, the Jsc continuously decreases accompanied with a small reduction of Voc. While the fill factor remains and even higher values of 83.70% at 0.1 sun illumination are obtained as compared with 77.31% at 1 sun illumination. Therefore, upon forming large polarons with enabled long-order orbit-orbit interaction, high fill factor independent of light illumination and the field-independent photocurrent are observed in quasi-2D perovskite solar cells with uniform dispersed different-n-value nanoplates. With the formation of large polarons with enabled long-order orbit-orbit interaction, reduced screening effects and aligned orbital polarization are expected, leading to enhanced charge transport and dissociation.

4.5 Summary

In summary, we explored long-order orbit-orbit interactions by using uniform dispersions of RPP nanoplates in quasi-2D perovskite $(PEA)_2(MA)_4Pb_5I_{16}$) films. The uniform dispersion of nanoplates can contribute to long-order orbital interactions, which lead to the large volume polarons from the transient absorption characteristics. Specifically, our photoexcitation polarization-dependent photocurrent studies found that the uniformly dispersed film leads to a long-order orbit-orbit interaction through reduced scattering. This was drawn by the experimental observation where switching the photoexcitation from linear to circular polarization leads to a -ΔJsc in uniformly dispersed quasi-2D perovskite films. The long-order orbit-orbit interaction provides a fundamental possibility to boost spin mixing from the bright states (spin allowed to recombine towards light emitting actions) to dark states (spin forbidden to recombine, tending to dissociate towards photovoltaic actions) towards boosting photovoltaic performance in quasi-2D perovskite films. Therefore, the long-order orbit-orbit interaction presents a new strategy to facilitate dynamical spin conversion of excited states during the development of photovoltaic actions.

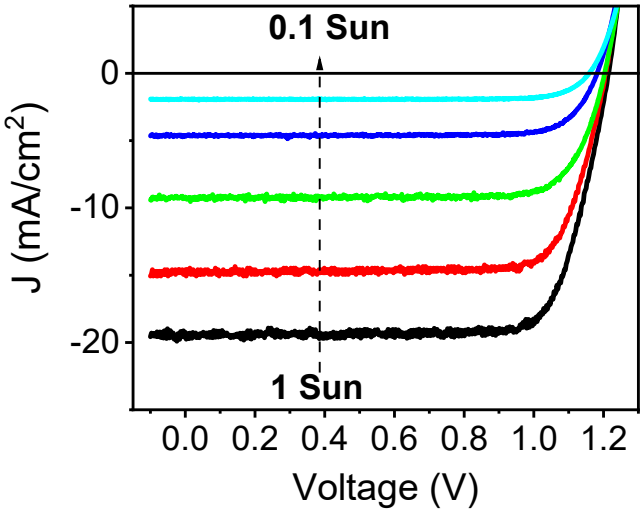


Figure 4- 5 J-V curves at different light illumination intensities from 1 sun to 0.1 Sun conditions for devices with uniform dispersion.

Table 4-1. Photovoltaic parameters for perovskite solar cells with uniform dispersion at different sun conditions.

Sun conditions	Jsc ($mAcm^{-2}$)	Voc (V)	FF	PCE
1 Sun	19.24	1.215	79.96%	18.69%
0.8 Sun	14.58	1.207	80.91%	14.24%
0.5 Sun	9.19	1.203	80.74%	8.93%
0.25 Sun	4.67	1.182	80.25%	4.43%
0.1 Sun	1.91	1.159	83.70%	1.85%

Chapter 5 Uniform permutation of quasi-2D perovskites by vacuum poling for efficient, high-fill-factor solar cells

5.1 Abstract

The vertically ordered (small-to-large n) quasi-2D perovskite films are served as common approaches to facilitate directional charge transfer. Here, we report a different strategy of uniformly arranging different-n-value nanoplates ($PEA_2MA_{n-1}Pb_nI_{3n+1}$) by introducing vacuum poling treatment to enforce nucleation during crystallization. This uniform distribution is verified by delicate mechanical tape-peeling method while monitoring optical absorption, photoluminescence (PL) and energy dispersive X-ray spectroscopy (EDS). With uniform distribution, efficient carrier transfer within 10 picoseconds is revealed by transient absorption. Moreover, record-high fill factor (FF) of 82.4 % with power conversion efficiency (PCE) of 18.04% (Voc =1.223V, Jsc =17.91 mA/cm^2) were demonstrated. Superior stability is achieved with retaining 96.1% of initial efficiency after 8-month storage, and maintaining 97.7% at 80 °C for over 180 h. This uniformly arranging different-n-value nanoplates offers a new material engineering strategy to enhance carrier transfer and extraction for developing high-efficiency and stable quasi-2D perovskite solar cells.

5.2 Introduction

Incorporation of long-chain organic ligands A' has improved the optoelectronic performance[147-152] and stabilities[63-65,153] of perovskites by forming quasi-2D structures with the formula of $A'_2A_{n-1}M_nX_{3n+1}$, where n refers to the number of planes of the corner-sharing $[MX_6]^{4-}$ octahedral, and A, M, X refer to the monovalent cations, divalent metal cations and halide anions, respectively. Remarkable tunability on optical properties via controlling morphological structures by selecting different functional A/A' molecules has been shown to be a unique feature for quasi-2D perovskites.[148,153-155] However, with the incorporation of long chain insulating organic ligands, carrier transport becomes a limiting factor to develop the optoelectronic properties. Vertically ordered small-n-value to large-n-value nanoplates between bottom and top surfaces of the quasi-2D perovskite films are normally self-assembled based on unequal growth rates of different-n-value nanoplates, in which different amounts of organic ligands such as PEA^+ act as a barrier for mass transfer towards crystallization during thermal annealing.[147, 156 - 158] Interestingly, such ordered n value dispersion in quasi-2D perovskite films provides an energy-cascade process to simultaneously transfer electrons and holes, and consequently enhancing carrier transport.[151,159-161] This vertically ordered nanoplates of different n values have been shown to be the primary

strategy to enhance photovoltaic[149, 162] and light-emitting performance[147,160,161] in quasi-2D perovskite devices. In the present work, we demonstrate a uniform dispersion of different-n-value nanoplates as a new strategy to enhance the optoelectronic properties of quasi-2D perovskites by using our vacuum poling treatment. Different from reported vacuum assisted annealing method, [163,164] we developed our vacuum poling treatment to enforce nucleation during crystallization, leading to uniform dispersion of different-n-value nanoplates. With this new design, the charge transfer and carrier extraction are further improved towards developing high-performance quasi-2D perovskite solar cells. This work has been published (*Joule 3*, 3061-3071, 2019).

5.3 Materials and Methods

5.3.1 Materials Processing and Device Fabrication

The ITO substrates were cleaned by ultrasonic treatment with detergent, deionized water, acetone and isopropanol, subsequently, for 20 minutes in each cycle. After cleaning, the ITO substrates were exposed to UV ozone for 30 minutes and followed by spin-coating PEDOT: PSS with the thickness of 40 nm or PTAA with the thickness of 10 nm. The PEDOT: PSS (Clevious PVP AI 4083) films coated at the rate of 4000 rpm for 1 minute were thermally annealed at 150 ℃ for 0.5 h; the PTAA (1.5 mg/mL in toluene) was spin-cast at the rate of 2000 rpm for 1 minute followed by thermal annealing at 110 ℃ for 10 minutes.

The precursor solution of with the target of <n>=5 quasi-2D perovskites was prepared by the mixture of PEAI:MAI:PbI_2:$PbCl_2$ with molar ratio of 0.4:0.9:0.95:0.05 in mixed solvent of DMF:DMSO (9:1 vol). The stoichiometric ratios to prepare <n>=4 and <n>=3 perovskites are 0.5M (PEAI): 0.85M (MAI): 0.95M (PbI_2): 0.05M ($PbCl_2$) and 0.67M (PEAI): 0.77M (MAI): 0.95M (PbI_2): 0.05M ($PbCl_2$), respectively. It should be noted that in-situ MACl additives were introduced through the reaction of $0.05PbCl_2$ + 0.1MAI = $0.05PbI_2$ + 0.1MACl for better crystallization and improved film quality.[165, 166] During the crystallization, different n-value nanoplates are co-grown to form quasi-2D perovskite films during spin-coating. The concentrations for perovskite precursor solutions used for the PEDOT: PSS and PTAA based devices were 1 M and 0.7 M of Pb^{2+}, respectively. All precursor solutions (200μL) were spin-cast on the preheated substrates (100 ℃ for over 20 min) at the rate of 5000 rpm for 20 s, followed by vacuum poling of 8 minutes in a vacuum chamber where the gage pressure is quickly reduced to -

1 bar within 14 s to initiate vacuum poling effects. It should be noted that to delay the crystallization during the spin-coating process, in situ MACl and additional DMSO were intentionally introduced in the precursor solution. Moreover, before starting spin-coating, we dropped large amount of cold precursor solution (200 μL) onto preheated substrate (1.5 cm x 1.5 cm) to further delay crystallization during the spin-coating. After thermal annealing, all samples including quasi-2D perovskites prepared with and without vacuum poling were thermally annealed at 100 ℃ for 10 minutes. The electron transport layer phenyl-C_{61}-butyric acid methyl ester ($PC_{61}BM$, 20 mg/mL in chlorobenzene) was spin-cast on top of perovskite films at 2000 rpm for 50 s and kept in dark for at least 60 mins before the coating of an interface-modifying layer PEI (0.5mg/mL, in anhydride 2-Propanol) at 5000 rpm for 60 s. Finally, these films were transferred into a thermal evaporator for the deposition of 90-nm-thick silver electrodes under a vacuum of 2×10^{-4} Pa. The 3D-only perovskite control devices are fabricated with the same device architecture following our previous procedure.[19]

5.3.2 Characterizations and Measurements

For tape peeling method, the thicknesses for unpeeled and peeled films are ~300 nm and ~25 nm for quasi-2D perovskite film, confirmed by atomic force microscopy (AFM). For NMR measurement, solvent Dimethyl sulfoxide-d6 (DMSO-D6) was purchased from commercial vendors and used without further purification. ^{1}H spectra were recorded at ambient temperature on a JEOL 400YH spectrometer, and ^{1}H NMR chemical shifts were referenced to the residual solvent. For SEM-EDS Mapping, scanning electron microscope (SEM) Energy-dispersive X-ray spectroscopies (EDS) mapping[76] was conducted on a Hitachi High-Technologies TM3030Plus SEM microscope at 15 kV.

Transient absorption spectra were collected by using a Helios fire spectrometer (Ultrafast Systems LLC). The pump pulses (346 nm, 5μW) were generated through a harmonic generator (Ultrafast Systems LLC, third harmonic) pumped by a Pharos laser (Light Conversion, 1kHz, 1030nm, 290fs). The 346 nm pump beam was focused into point on the samples with the diameter of ~100 μm.

The device active area is 0.06 cm^2, which is realized by shadow mask. The current-voltage (I-V) characteristics of the solar cells were measured by scanning the voltage from -0.1 to 1.25 V

(forward scan) and then from 1.25 to -0.1 V (reverse scan) with 0.68 mV step and NPLC=0.001. The I–V characteristics were recorded by using Keithley 2400 source meter under the illumination of AM 1.5G 100 mW/cm^2 from Newport solar simulator calibrated by a silicon reference cell. Operational stability tests were operated under constant bias at maximum power point in nitrogen glove-box. Thermal stability tests were operated by placing the device on the hotplate with temperature at 80 ℃.

The absorption spectrum is measured with an integrating sphere system (R7, ideaoptics, China) equipped with spectrometers (PG2000-Pro, NIR1700, ideaoptics, China). The external quantum efficiency (EQE) spectra were measured by subjecting the cells to a monochromatic illumination (300 W Xe lamp passing through a monochromator and appropriate filters). The light intensity was calibrated by a standard Si based photodetector (DET100A, 350 nm-1100 nm, Thor Labs). The light beam was chopped at 230 Hz and the response of the cell was acquired by a Stanford Research SR830 lock-in amplifier. The PL lifetimes were measured by Streak camera (HAMAMATSU C10627) by exciting the samples with a 346 nm pulse laser (300 fs per pulse) generated by noncollinear optical parametric amplifier (NOPA) seeded by the second harmonic of a Yb-doped fiber laser (TANGERINE, Amplitude System) with 50 kHz repetition rate and the average power of 10 μW.

5.4 Results and Discussion

As schematically shown in **Figure 5-1a**, the precursor solutions with the stoichiometry designed to <n> = 5 are first spin-cast on pre-heated substrates to form high density of nucleus. Then the films are immediately placed in a chamber for 8 minutes with the gage pressure quickly decreasing to -1.0 bar. Here, applying vacuum poling treatment can simultaneously increase the nucleation and limit the grain sizes by quickly removing residual solvent towards realizing uniform dispersion of different-n-value nanoplates. Afterwards, thermal annealing is followed to further crystallize the 2D nanoplates at 100 ℃ for 10 minutes in N_2 atmosphere. Consequently, high-quality quasi-2D perovskite films are formed with uniform dispersion of different-n-value nanoplates. The competition between crystallization and nucleation process during vacuum poling treatment is verified by absorption and photoluminescence (PL) results (see **Figure 5-2**). On contrast, without vacuum poling treatment, the un-accelerated nucleation leads to the crystallization to form nanoplates with small n values on the bottom surface and large n values

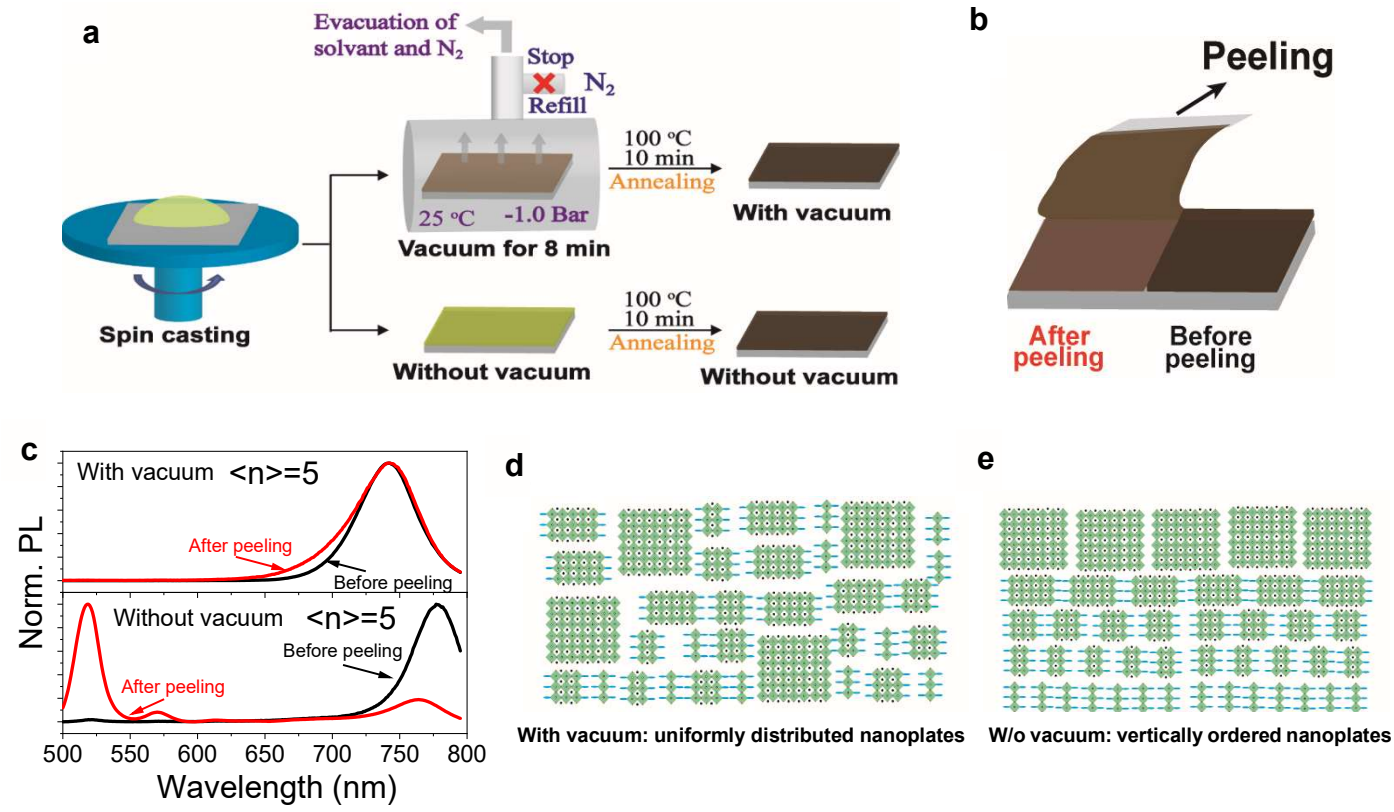


Figure 5- 1 Schematic diagram of film fabrication procedure and tape peeling-based photoluminescence (PL) characterizations of quasi-2D perovskite films prepared with and without vacuum poling treatment. (a) Schematic diagram to show processing methods with and without vacuum poling treatment to prepare quasi-2D perovskite films. (b) Schematic drawing to illustrate our tape-peeling method, to mechanically detach monolayers from quasi-2D perovskite films, while subsequently measuring PL spectra. (c) PL spectra measured before and after peeling for <n>=5 quasi-2D perovskite films prepared with and without vacuum poling treatment. (d), (e) Schematic diagram to indicate uniform (d) and ordered (e) formation of different-n-value nanoplates in quasi-2D perovskite films prepared with and without vacuum poling treatment.

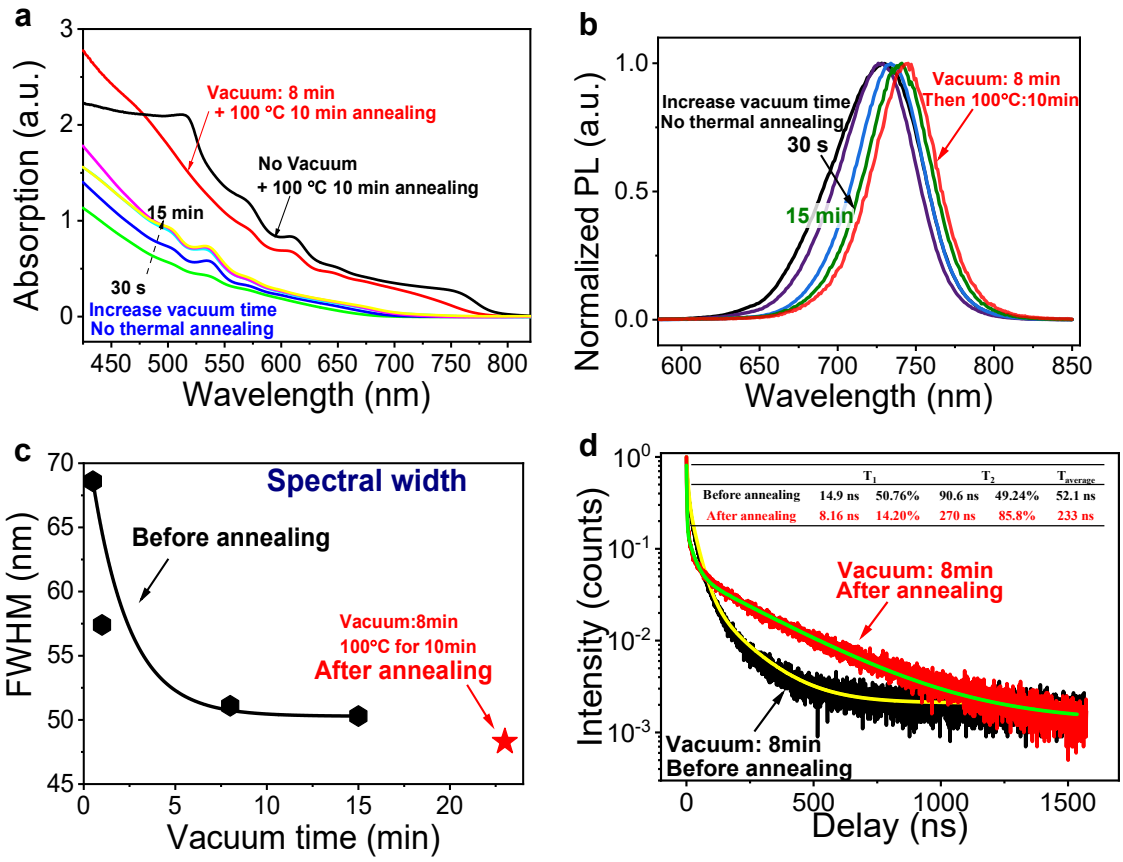


Figure 5- 2 Absorption and photoluminescence (PL) results of films (<n>=5) right after different vacuum-poling-treated times before thermal annealing. (a) Absorption evolution induced by vacuum poling treatment and thermal annealing. With nucleation prior to full crystallization, the absorbance remains very low before annealing. After annealing, absorption become increased, showing full crystallization. (b) Normalized PL spectra of films after different vacuum-poling-treated times. There is a red shift as vacuum-poling-treatment time increases, indicating the further formation of large-n-value nanoplates. (c) Spectral width (FWHM) of films as a function of vacuum-poling-treated time. All the vacuum-poling-treated films without annealing show broader spectral width than annealed film due to inhomogeneous disorder from insufficient crystallization. (d) Transient PL results of perovskite films before (black curve) and after (red curve) annealing. After fully crystallization, the annealed film (red recurve) shows much longer lifetime.

towards the top surface, creating vertically ordered (small-to-large n) dispersion of nanoplates in quasi-2D perovskite films under thermal annealing.

To reveal the uniform dispersion of different-n-value nanoplates between bottom and top surfaces in quasi-2D perovskite films induced by vacuum poling treatment, we developed a delicate tape-peeling method (**Figure 5-1b**, the thicknesses for unpeeled and peeled films are ~300 nm and ~25 nm), to mechanically detach the multiple monolayers of nanoplates from top surface subsequently towards bottom surface while monitoring PL, as shown in **Figure 5-1c**. With mechanically tape peeling method, very similar PL spectra with dominated peak at 740 nm is observed after peeling off multiple monolayers of nanoplates from top surface towards bottom surface. These provide additional evidence of uniform distribution of nanoplates within quasi-2D perovskite films prepared with vacuum poling treatment.

On contrast, without vacuum poling treatment, the formation of an ordered distribution of nanoplates with small-n value towards the bottom and large-n value towards the top are suggested. Meanwhile, with mechanically tape peeling method, very different PL spectra (see down figure of **Figure 5-1c**) are observed: the dominant PL peak locates at 778nm related to large-n-value nanoplates before peeling and 519nm related to small-n-value nanoplates after peeling, further proving the existence of ordered distribution of nanoplates. In addition, it should be noted that the coexistence of multiple PL peaks indicates that the charge transfer is not efficient between nanoplates with ordered-n-value dispersion. The spatial distribution of different n-value nanoplates are illustrated in **Figure 5-1d** and **1e**.

To discuss the dynamics of charge transfer in quasi-2D perovskite films, transient absorption (TA) measurements were carried out. With vacuum poling treatment, the TA measured through top and bottom show similar characteristics as shown in **Figure 5-3a**, further verifying the uniform dispersion of different-n-value nanoplates. Without vacuum poling treatment, the TA measured through top and bottom show very different characteristics (see **Figure 5-3b**), verifying smaller-n-value and larger-n-value nanoplates are distributed towards bottom and top, respectively. This is consistent with the publication of other ordered quasi-2D perovskite films.[150] Moreover, TA dynamics at wavelengths at 534 nm, 567 nm, 609 nm and 724 nm (or 750 nm) correspond to signals from small-n-value to largest-n-value nanoplates are plotted in **Figure 5-3c** and **3d**. It is shown that vacuum poling treatment leads to a fast increment within 10 ps on the negative $\Delta A/A$

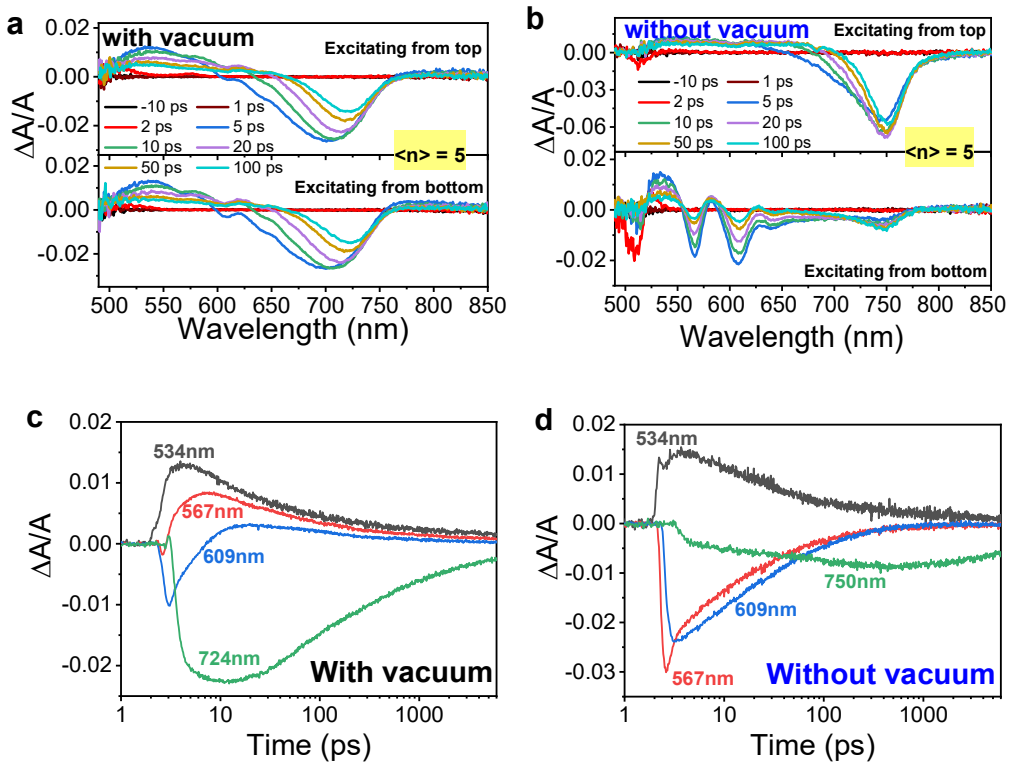


Figure 5- 3 Transient absorption (TA) spectra at different delay times (-10 ps, 1 ps, 2ps, 5ps, 10 ps, 20 ps, 50 ps, 100 ps) and dynamics of quasi-2D perovskite (<n>=5) films when exciting through top (upper figures of a and b) and bottom (down figures of a and b). The wavelengths at 534 nm, 567 nm, 609 nm and 724 nm (750 nm) Correspond to Signals from Small-n-value to Largest-n-value Nanoplates. (a) With vacuum poling treatment. TA spectra are similar when exciting through top (upper figure) and bottom (down figure), indicating the uniform distribution of nanoplates. (b) Without vacuum poling treatment. TA spectra are quite different when exciting through top (upper figure) and bottom (down figure), indicating order dispersion of nanoplates. (c) <n>=5 film with vacuum poling treatment shows positive transient absorption signals at small-n-value nanoplates and fast (within 10 ps) increased negative signal at 724 nm (corresponding to largest-n-value nanoplates). (d) <n>=5 film without vacuum poling treatment shows both positive (at 534 nm) and negative (at 567 nm and 609 nm) transient absorption signals at small-n-value nanoplates and slow (~ 600 ps) negative signal at 750 nm (corresponding to largest-n-value nanoplates).

signal at 724 nm in **Figure 5-3c** (corresponding to largest-n-value nanoplates). At the meantime, positive ΔA/A signals at other wavelengths are observed, indicating the charge transfer from small-n-value nanoplates to largest-n-value nanoplates is very efficient without much accumulations between nanoplates. On contrast, without vacuum poling treatment, the negative ΔA/A signal (750 nm in **Figure 5-3d**: corresponding to largest-n-value nanoplates) shows a much slower increment within 600 ps, while negative ΔA/A signals also appear at 567 nm and 609 nm. It implies that accumulations of charge carriers occur at corresponding small-n-value nanoplates (567nm and 609nm), leading to less efficient charge transfer in the ordered dispersion of different-n-value nanoplates prepared without vacuum poling treatment.

To further understand the dynamics of photoexcited states under uniform and ordered dispersions of different-n-value nanoplates, PL characteristics were analyzed for quasi-2D perovskite films prepared with and without vacuum poling treatment. Under both conditions, the PL spectra consist of various peaks originating from different n-value nanoplates (n=1, 2, 3, 4, n > 4) peaked at around 518 nm, 570 nm, 612nm, 710 nm and 750 nm, as shown in **Figure 5-3a** and **3b**. However, with vacuum poling, increasing the photoexcitation intensity at 405 nm significantly increases the light emission from the largest-n-value nanoplates (n > 4), while the light emission from small n values (n ≤ 4) are slightly increased (see the inset of **Figure 5-4a**). This intensity-dependent PL[160,161] indicates that the uniform dispersion of different-n-value nanoplates generates efficient transport of photogenerated carriers from small to large n-value nanoplates in quasi-2D perovskite films prepared with vacuum poling treatment. Contrarily, without vacuum poling, increasing excitation intensity mainly increases the light emission from small-n-value nanoplates dominated by n = 1 (see **Figure 5-4b**). This implies that the transport of photogenerated carriers is less efficient in the ordered dispersion of different-n-value nanoplates.

Moreover, we notice that the vacuum poling treatment increases the slope of PL-excitation intensity dependence from 1.61 to 1.95 towards ideal bimolecular recombination in the large-n-value nanoplates with emission at 750 nm but the slop almost keeps unchanged in small-n-value nanoplates with emission peaked at around 518 nm, 570nm, 612nm, 710 nm (shown in **Figure 5-4c**). This phenomenon may imply that small-n-value nanoplates can function as passivation agents and largest-n-value nanoplates as the emitting centers, which is similar to our recent observation that small grains can passivate the defects on the surfaces of large grains in hybrid

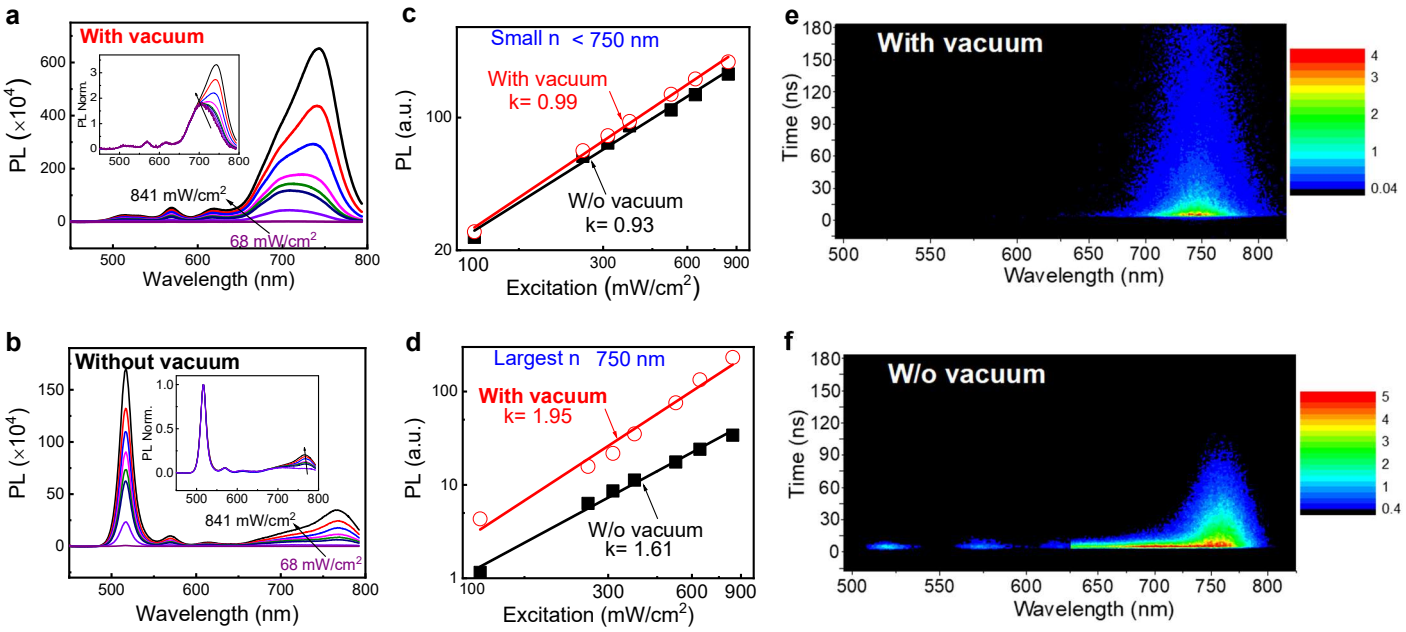


Figure 5- 4 PL Characterizations and dynamics for quasi-2D perovskite films prepared with and without vacuum poling treatment. (a), (b) PL spectra for quasi-2D perovskite films prepared with and without vacuum poling treatment. (c) PL-excitation intensity dependences for emission peaks ≤ 710 nm related to small n-value nanoplates prepared with and without vacuum poling treatment. (d) PL-excitation intensity dependences (at 750 nm) for largest n-value nanoplates prepared with and without vacuum poling treatment. (e), (f) PL dynamics for quasi-2D perovskite films prepared with and without vacuum poling treatment. Sample structure: ITO/PEDOT:PSS/Perovskite. Excitation: 346 nm pulse laser (pulse width of 290 fs) with Intensity of 5 μW.

perovskites.[167,168] In quasi-2D perovskite films with uniform distribution of nanoplates, large-n-value nanoplates are surrounded by small-n-value nanoplates, which enables more contacts for passivation than ordered dispersion of nanoplates (the films without vacuum poling treatment). TRPL data detected with the streak camera in **Figure 5-4e** and **4f** indicate the prolonged PL lifetime under vacuum poling treatment. Clearly, the uniform dispersion of nanoplates shows one major emission peak at 750 nm with a longer lifetime while the ordered nanoplates show multiple emission peaks with shorter PL lifetimes.

To understand the carrier extraction mechanism under uniform dispersion of different-n-value nanoplates based on vacuum poling treatment, the photovoltaic performance was characterized based on the device architecture of ITO/PTAA/$PEA_2MA_{n-1}Pb_nI_{3n+1}$/$PC_{61}BM$/PEI/Ag. As shown in **Figure 5-5a**, the vacuum poling treatment leads to the record-high FF of 82.4 % with the PCE reaching 18.04 % (Voc = 1.223 V, Jsc = 17.91 mA/cm^2), indicating extremely efficient carrier extraction under the uniform dispersion of different-n-value nanoplates

It is well known that using different organic ligands and transport-layer engineering can improve the FF of quasi-2D perovskite solar cells.[169 -174] Here, we compare the solar cells prepared by our vacuum poling treatment with the devices prepared by published conventional non-vacuum method. Clearly, the FF of our champion devices is the highest among published quasi-2D perovskite solar cells (see **Figure 5-5b**).

Moreover, the upper curve of **Figure 5-5c** shows the output efficiency at maximum power point (MPP) monitored continuously without device encapsulation. The PCE remains as high as 95.2 % of the maximum point after more than 9.5 hours, indicating considerably improved operational stability at continuous working condition. More surprisingly, after heating the device at 80 ℃ for over 180 hours, the PCE maintains 97.7% (see middle curve of **Figure 5-5c**) of its original value for quasi-2D perovskite devices prepared with vacuum poling treatment, which indicates extremely good thermal stability. In addition, the device efficiency retains 96.1 % of original value after storing in glove box for 8 months without encapsulation (see down curve of **Figure 5-5c**). The statistics data in **Figure 5-5d** show that vacuum poling treatment significantly improves reproducibility of device performance. As schematically shown in **Figure 5-5e**, the uniform dispersion increases the contact probabilities between different-n-value nanoplates to generate isotropic transport from all small-n-value nanoplates directly to largest-n-value

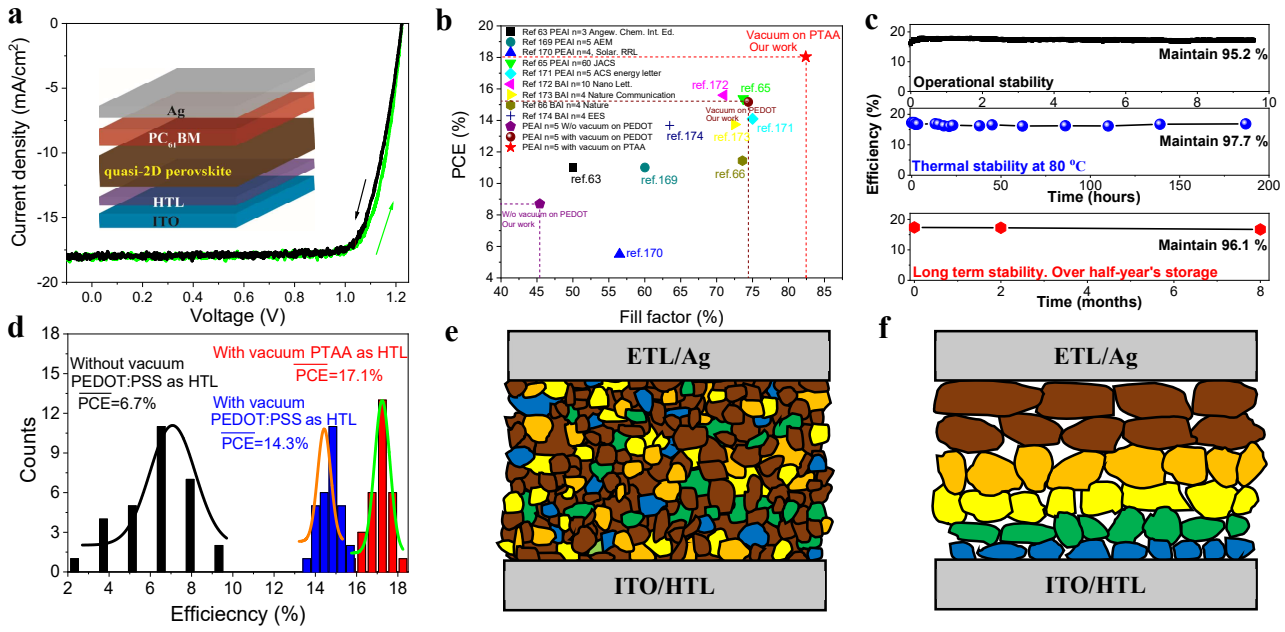


Figure 5- 5 Characterizations and schematic diagram of quasi-2D perovskite solar cells prepared with/without vacuum poling treatment. (a) I-V characteristics measured under 1 Sun illumination in quasi-2D perovskite solar cells prepared with vacuum poling treatment (PTAA used as hole transport layer (HTL)). (b) Photovoltaic performance (FF and PCE) of our device as compared with published PEA^+ and BA^+ based quasi-2D perovskite solar cells. Our vacuum poling treatment leads to extremely high FF and PCE. (c) Device stability test of quasi-2D perovskite device prepared with vacuum poling treatment (HTL: PTAA) under various conditions. Upper figure: operational stability under continuous one-sun illumination; Middle figure: thermal stability at 80 ^oC; Down figure: Over half a year long term stability in glovebox. (d) Statistics data of photovoltaic performance of quasi-2D perovskite solar cells with three different designs: without vacuum poling on PEDOT:PSS, with vacuum poling on PEDOT:PSS and with vacuum poling on PTAA. (e) Schematic diagram to show isotropic carrier extraction from small-n-value nanoplates directly to largest-n-value nanoplates functioning as transport high-way (shown in brown color) under uniform dispersion of different-n-value nanoplates. (f) Schematic diagram to show less efficient and prolonged carrier extraction length from n=1 to n=2, n=3, n=4, n=5 nanoplates through cascade process under ordered dispersion of different-n-value nanoplates. Blue and green area: small-n-value nanoplates, yellow and orange area: medium-n-value nanoplates, brown area: largest-n-value nanoplates.

nanoplates. Consequently, photogenerated carriers are isotropically transported from small-n-value nanoplates to largest-n-value nanoplates in all directions in quasi-2D perovskite films prepared with uniform dispersion of nanoplates. It should be emphasized that the uniform dispersion can decrease the transport time to collect photogenerated carriers because all photogenerated carriers in small-n-value nanoplates have an opportunity to directly transport to largest-n-value nanoplates (functioning as transport-highway network), due to the increased contact probabilities between different-n-value nanoplates. Therefore, a record-high fill factor (82.4%) is demonstrated in our work. On contrast, in ordered dispersion, the photogenerated carriers are cascaded from n=1 to n=2, n=3, n=4, n=5 nanoplates, leading to a prolonged time to collect photogenerated carriers through such cascade process. In ordered dispersion (see **Figure 5-5f**), large-n-value nanoplates do not form a continuous network vertically, consequently lacking the transport highway to more effectively collect photogenerated carriers.

5.5 Summary

In summary, we explored the uniform dispersion of different-n-value nanoplates homogenously located between bottom and top surfaces in quasi-2D perovskite films [$(PEA)_2(MA)_{n-1}Pb_nI_{3n+1}$] by introducing vacuum poling treatment. On contrast, without vacuum poling treatment, the different-n-value nanoplates are formed with vertically ordered dispersion from small to large n values between bottom and top surfaces in quasi-2D perovskite films. The uniform and ordered dispersions of different-n-value nanoplates between bottom and top surfaces were verified by our tape peeling method to mechanically detach monolayers of nanoplates from top surface subsequently towards bottom surface while monitoring the EDS, PL spectra and optical absorption. The TA results showed that the uniform dispersion of different-n-value nanoplates leads to a fast charge transfer towards the largest-n-value nanoplates within 10 picoseconds. The PL dynamics studies implied that, with vacuum poling-enabled uniform dispersion, small-n-value and large-n-value nanoplates may function as passivation agents and light-emitting centers, respectively, in quasi-2D perovskite films with enhanced PL intensity and lifetime. Furthermore, with uniform dispersion of different-n-value nanoplates, the quasi-2D perovskite solar cells demonstrate a record-high FF (82.4 %) with maximum PCE of 18.04 % (Jsc = 17.91 mA/cm^2 and Voc = 1.223 V) based on the device structure of ITO/PTAA/$PEA_2MA_{n-1}Pb_nI_{3n+1}$/$PC_{61}BM$/PEI/Ag. Surprisingly, superior stabilities are achieved with retaining over 96% of their initial efficiency

after storing for 8 months, and 97.7% of the original value at 80 °C for over 180 h. Therefore, uniformly arranging different-n-value nanoplates through vacuum poling treatment provides a new strategy to enhance carrier extraction towards developing high-performance quasi-2D perovskite optoelectronics.

Chapter 6 Enabling AC electroluminescence in quasi-2D perovskites by uniformly arranging different-n-value nanoplates to allow bidirectional charge transport

6.1 Abstract

Perovskite light-emitting diodes (LEDs) are normally operated under forward direct current (DC) to realize electron/hole injection at cathode/anode surfaces. Here, we demonstrate an alternating current (AC) driven LED enabled by bi-directionally allowed charge transport in quasi-2D perovskite ($PEA_2MA_{n-1}Pb_nI_{3n+1}$) film. Essentially, the bi-directional charge transport is realized by uniformly arranging different-n-value 2D nanoplates together with symmetrically designed anode/cathode interfaces, which can allow injected electrons and holes to form light-emitting states under both forward and reverse biases, leading to an AC electroluminescence (EL) with the device architecture of ITO/PEI/PEDOT:PSS/$PEA_2MA_{n-1}Pb_nI_{3n+1}$/P3HT/PEI/Ag. The high AC EL performance was achieved with the radiance = 24 $WSr^{-1}m^{-2}$ and 18.3 $WSr^{-1}m^{-2}$ and EQE = 12.5% and 3.7% under forward and reverse biases. The device-operational stability was largely improved with the half-intensity time of T_{50} = 11.0 hours under AC bias (+2 V/-2 V, 50 Hz) as compared to T_{50} = 3.9 hours under forward bias (+2 V/0 V, 50 Hz).

6.2 Introduction

Metal halide perovskites have demonstrated superior photoluminescence quantum yield[73-75], facile color tuning capabilities[1-4], and high-quality thin-film formation[69,84-86], leading to excellent performance in LEDs[70,71]. In general, LEDs are allowed to operate under forward bias due to the limitation where reduced potential barriers at the anode and cathode can only be realized under forward electrical field to simultaneously enable bipolar electron and hole injection towards generating an EL[175,176]. When switching an external bias from forward to reverse condition, it is normally difficult to realize carrier injection due to the high potential barriers at both electrodes. Therefore, when an AC bias is applied, the LEDs normally give rise to an EL only during forward cycle and leave in-operational EL during reverse cycle. To develop an AC LED, the fundamental challenge is to realize an EL under both forward and reverse cycles under AC bias. Notably, symmetrically configured device band diagrams were adopted in organic LEDs to show AC EL[177,178]. Furthermore, the light-emitting electrochemical cells (LEECs) with desired n-/p- type doping by mobile ions at the interfaces were proposed to increase injection probabilities for both electrons and holes under AC bias[179-181]. On the other hand, perovskite LEECs have also been fabricated based on $MAPbI_3$ to show an AC EL by using ions-induced band bending at interfaces to facilitate bipolar injection under both forward and reverse biases[182].

In the present work, we explored strategies to realize AC EL by using symmetrical device architecture together with quasi-2D perovskite ($PEA_2MA_{n-1}Pb_nI_{3n+1}$) film where different-n-value nanoplates are uniformly dispersed by enforcing the crystallization with our vacuum-poling treatment[145]. Here, it's worthy to point out that within uniform dispersion of different-n-value nanoplates, the charge transport is occurred through two processes: (i) from all small-n-value nanoplates directly to largest-n-value nanoplates through direct contact[183] and (ii) within the network between largest-n-value nanoplates. Furthermore, different-n-value 2D perovskite nanoplates possess different optical bandgap and energy levels of conduction band minimum (CB) and valence band maximum (VB). Thus, uniformly distributed nanoplates will provide more energy levels to accept and transfer the injected carriers, leading to a unique mechanism to realize efficient charge transport bidirectionally under both forward and reverse biases. In addition, we also selected poly(ethyleneimine) (PEI) layer to modify the work functions of indium tin oxide (ITO) and Ag electrodes, and the poly(3,4-ethylenedioxythiophene) polystyrene sulfonate (PEDOT:PSS) and poly(3-hexylthiophene) (P3HT) transport layers were chosen to ensure better device symmetry towards balancing electron/hole injection. Also, the PEDOT:PSS and P3HT have relatively proper conductivities for electrons and holes, which are also important to carry out AC EL. With above design, we demonstrated an AC EL from our quasi-2D perovskite film with the device architecture of ITO/PEI/PEDOT:PSS/$PEA_2MA_{n-1}Pb_nI_{3n+1}$/P3HT/PEI/Ag. EL under AC bias at frequency from 1 to 100 Hz were also realized. Furthermore, device-operational stability under AC bias was largely improved as compared with under forward bias. Therefore, our findings provide a design and open up the way to achieve efficient AC LEDs in metal halide perovskites. This work has been published (*Nano Energy 79*, 105413, 2021).

6.3 Materials and Methods

6.3.1 Materials Processing and Device Fabrication

Lead iodide (PbI_2), P3HT, dimethyl sulfoxide (DMSO), Dimethylformamide (DMF), PEI (50wt%), chlorobenzene (CB) and anhydride isopropyl alcohol (IPA) were purchased from Sigma-Aldrich. Methylammonium iodide (MAI) and phenethylammonium iodide (PEAI) were purchased from Xi'an Polymer Light Technology Corp. PEDOT:PSS was purchased from Clevios. All chemicals were used as received without further purification. The quasi-2D perovskite precursor

solution (concentration: 1 M) was prepared by mixing PEAI:MAI:PbI_2:$PbCl_2$ with the molar ratio of 0.4:0.9:0.95:0.05 in mixed solvent of DMF:DMSO (9:1 vol)), and the stoichiometry was designed to a target of <n> = 5. The ratio designed in our work would result in 1M $(PEA)_2(MA)_4Pb_5I_{16}$ + 0.1M MACl. We have added in-situ MACl additives through the reaction of 0.05 $PbCl_2$ + 0.1MAI = 0.05 PbI_2 + 0.1 MACl in the precursor solution for better crystallization and improved film quality. P3HT was dissolved in CB with different concentrations: 3 mg/ml, 6 mg/ml and 9 mg/ml. PEI (50mt% in water) was diluted by anhydride IPA to a concentration of 0.5 mg/ml. First, an interface modification layer of PEI (0.5 mg/ml, IPA) was spin coated onto precleaned ITO substrates at a spin speed of 5000 rpm for 60 seconds, then the PEI layer was kept in dark for over 20 min to remove the residual solvent. After that, PEDOT:PSS was spin-coated on top of PEI at 4000 rpm for 60 seconds, and then followed by thermal annealing at 150 ℃ for 30 minutes. The quasi-2D perovskite layer was prepared following our previously reported vacuum poling method. In short, 200 μL of perovskite precursor solution were dropped onto the preheated PEDOT:PSS (100 ℃, over 20 min inside the nitrogen glove box), and the spin speed was set to 5000 rpm for 25 s, then the spin-coated perovskite film was immediately transferred into an antechamber where the gage pressure was quickly reduced to -1.0 bar and the vacuum poling treatment was kept for 8 min. Then, the vacuum poling treated perovskite film was put onto a hot plate for further thermal annealing (100 ℃ for 10 min). After that, P3HT with different concentrations was spin coated onto the perovskite layer at the speed of 2000 rpm for 50 s, then the P3HT layer was kept in dark for over 20 min to remove the residual solvent. Next, another interface modification layer of PEI was spin-coated on the top of P3HT as described above. Finally, silver layers (90 nm) were thermally deposited as the top electrode to complete the devices. The active area of the devices is 0.06 cm^2.

6.3.2 Characterizations and measurements

The PL and EL spectra were collected with Flouro Log III spectrometer. The current-voltage (I-V) characteristics were recorded using Keithley 2400 source meter. The GIWAXS data was collected by using sector 8-IDE at the Advanced Photon Source at Argonne National Laboratory. The AC EL profiles were recorded by oscilloscope (TDS 3032B from Tektronix). The EL intensities were calibrated by comparing their EL intensities with a commercialized near infrared LED (LED with glass lens, 750 nm, 18mW, TO-18, THORLABS). The alternating bias

was generated by a pulsed generator (model 645, 50 MHz function/arbitrary waveform generator from Berkeley Nucleonics Corp).

6.4 Results and Discussion

It is noted that, an AC EL requires three necessary conditions: (i) the mechanism to allow bipolar charge injection under both forward and reverse biases (injection issue), (ii) the confinement probabilities of injected electrons and holes (exciton formation issue), (iii) the possibilities of passivating defects on light-emitting nanoplates (photoluminescence efficiency issue). Here, the quasi-2D perovskite film with target <n> value of 5, in-situ MACl passivation and uniform dispersed different-n-value nanoplates is optimized through comparing film quality, PL lifetime and device performance. In this study, we utilize the uniformly arranged quasi-2D perovskite[145] together with symmetrical device architecture by using PEI, PEDOT:PSS and P3HT to explore AC EL, as schematically shown in **Figure 6-1a**. The grazing incidence wide angle X-ray scattering (GIWAXS) data for the uniformly dispersed film of <n> = 5 is shown in **Figure 6-1b**. Compared with previous reports[66,184], the dots feature together with weaker (202) signal at $q_y = 0$ as compared with that at $q_z = 0$ indicates that 2D nanoplates within the uniformly dispersed film of <n> =5 are more vertically orientated. To clearly show that different-n-value nanoplates are co-existed in our uniformly dispersed <n> = 5 films, the transient absorption (TA) combined with photoluminescence (PL) characteristics were studied. The TA spectra in **Figure 6-1c** show that the <n>=5 film consists of feature peaks at 530 nm (refer to n=1), 564.6 nm (refer to n=2), 603.8 nm (refer to n=3), 639.3 nm (refer to n =4), 668.8 nm and 726.7 nm (refer to n≥5), implying the coexistence of different-n-value nanoplates. We should note that there exists a charge transfer from small-n-value nanoplates to large-n-value nanoplates, as indicated by the fact that increasing excitation intensity changes the relative PL intensities between small- and large-n-value nanoplates (**Figure 5-4a**). Because of charge transfer, the lower PL intensity corresponding to small-n-value nanoplates does not really mean the un-appreciable amount. However, with low excitation density (68 mW/cm^2)**,** coexisted PL peaks at 530 nm, 564.6 nm, 603.8 nm, 639.3 nm and 650 nm to 740 nm can be observed, which further verifies the coexistence of different-n-value nanoplates.

We should point out that uniformly dispersing different-n-value nanoplates offers high-quality dense quasi-2D perovskite films where small-n-value nanoplates all have an opportunity to contact with large-n-value nanoplates to enable bidirectional charge transport. To investigate

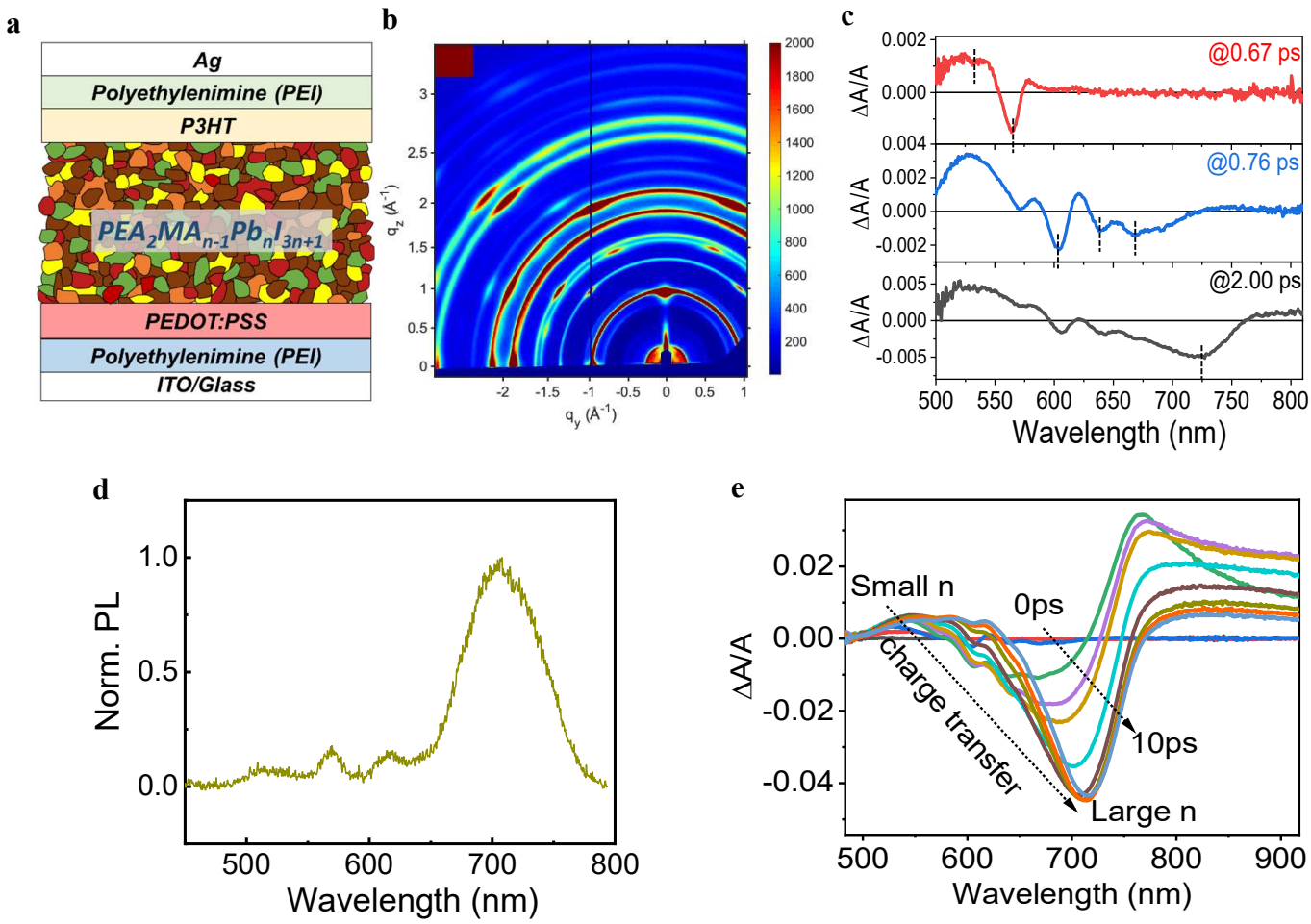


Figure 6- 1 Quasi-2D perovskite LEDs towards realizing both forward and reverse EL. (a) Quasi-2D perovskite LEDs based on device architecture of ITO/PEI/PEDOT:PSS/$PEA_2MA_{n-1}Pb_nI_{3n+1}$/P3HT/PEI/Ag. (b) GIWAXS map for uniformly dispersed quasi-2D perovskite film of <n>=5. (c) TA spectra for uniformly dispersed film of <n>=5 at different delay times with feature peaks corresponding to different-n-value nanoplates marked with dashed black lines: 530 nm (n=1), 564.6 nm (n=2), 603.8 nm (n=3), 639.3 nm (n =4), 668.8 nm and 726.7 nm (n≥5). (d) PL spectra for uniformly dispersed film of <n>=5 (with 405 nm laser excitation at power intensity of 68 mW/cm^2). Feature peaks corresponding to different-n-value nanoplates are observed: 527 nm (n=1), 568.8 nm (n=2), 613.7 (n=3), 645 (n=4) and 744.1 nm (n≥5). (e) TA spectra of uniformly dispersed film of <n>=5 at delay time from 0 to 10 ps.

the charge transport dynamics, we monitored the pump-probe transient absorption spectra of the quasi-2D perovskite film. As shown in **Figure 6-1e**, the TA feature peaks corresponding to small-n-value nanoplates quickly appear before 1.33 ps. With increasing pump-probe delay time, the photobleaching peak is rapidly red-shifted towards larger-n-value nanoplates, showing the fast charge transfer from small to large-n-value nanoplates. After 7 ps, the photobleaching peak is dominated by the signal from large-n-nanoplates, indicating efficient charge transfer occurred within 7 ps in quasi-2D perovskite film prepared with the uniform dispersion of different-n-value nanoplates. Therefore, there are two key parameters to control EL performance within uniform dispersion of different-n-value nanoplates: (i) the probability that all small-n-value nanoplates can directly contact with largest-n-value nanoplates: the issue for effective defect passivation towards charge transfer and high light emission, and (ii) the ratio between small-n-value nanoplates and largest-n-value nanoplates: the issue for charge confinement towards forming excitons.

Figure 6-2 illustrates the band diagram for quasi-2D perovskite film with the uniform dispersion of different-n-value nanoplates fabricated with the device architecture of ITO/PEI/PEDOT:PSS/$PEA_2MA_{n-1}Pb_nI_{3n+1}$/P3HT/PEI/Ag. Here, PEI is used to modify the work functions of both electrodes (ITO and Ag) to enable similar injection barriers for electrons and holes at both forward and reverse bias. We select PEDOT:PSS and P3HT as the transport material to sandwich perovskite layer due to their favorable energy levels towards balancing electron/hole injection and relatively proper electron and hole mobilities[185,186]. The nanoplates within the perovskite layer show different energy levels with the CB and VB, respectively. Because of the uniform dispersion of different-n-value nanoplates, both electron and hole injection surfaces consist of multiple CB and VB levels. Once the electrons are injected into the lowest CB (n = 5) under forward and reverse biases, the holes can be injected from small-n-value nanoplates into large-n-value nanoplates, leading to a cascade process to facilitate hole injection. Upon enabling electron and hole injection under both forward and reverse biases, an AC EL can be expected in quasi-2D perovskite film prepared with the uniform dispersion of different-n-value nanoplates.

As discussed above, an AC EL requires similar injection and transport under both forward and reverse biases. Here, the PEDOT:PSS and P3HT were used as the transport layers based on the favorable energy levels towards similar injection under forward and reverse conditions. Furthermore, the ambipolar transport properties of P3HT[187] facilitates the transport for both

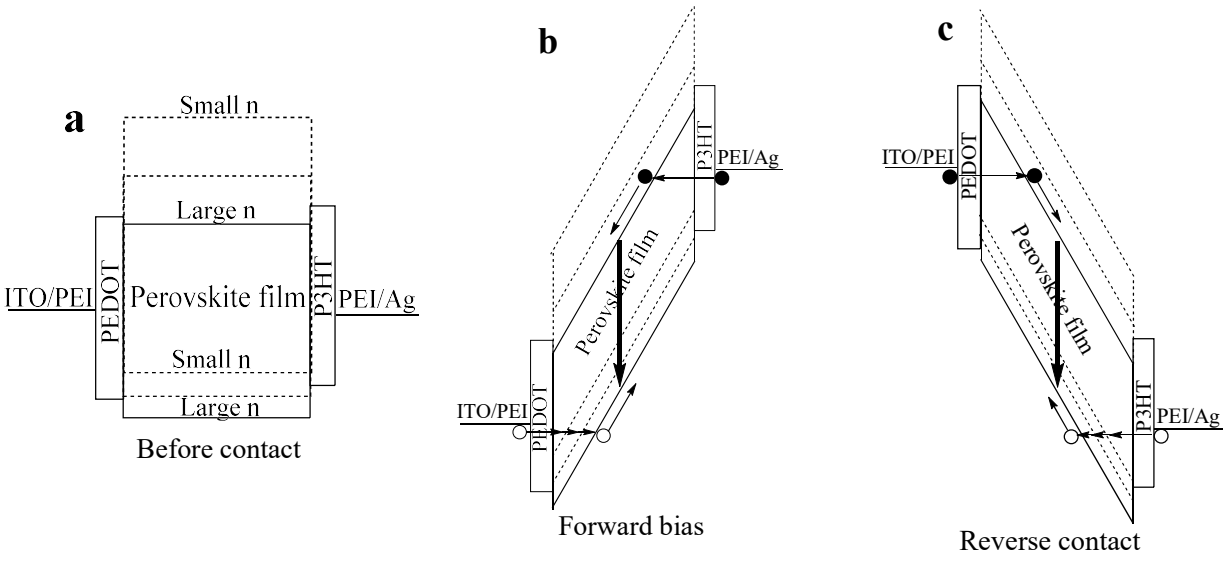


Figure 6- 2 Band diagram to enable AC EL in quasi-2D perovskite LEDs with uniform dispersion of different-n-value nanoplates. (a) Before contact. (b) Forward bias. (c) Reverse bias.

electrons and holes. We should note that, the P3HT has much lower carrier mobility than PEDOT:PSS[150], and consequently the device performance is very sensitive to the P3HT thickness. **Figure 6-3a** shows the current-voltage-EL (I-V-L) characteristics of our quasi-2D perovskite LEDs with an optimized P3HT thickness spin-coated from the concentration of 6 mg/mL. Clearly, the bipolar (electron and hole) injection can be realized under forward and reverse biases. Interestingly, both forward and reverse bipolar injection can successfully generate an EL at threshold biases of 1.7 V and -1.3 V, leading to an AC EL in the quasi-2D perovskite LEDs (ITO/PEI/PEDOT:PSS/$PEA_2MA_{n-1}Pb_nI_{3n+1}$/P3HT/PEI/Ag). The EL irradiance reaches 24.0 W/Sr/m^2 at the forward bias of 2.5 V and 18.3 W/Sr/m^2 at the reverse bias of -1.5 V. The similar EL characteristics between forward and reverse biases indicate that the quasi-2D perovskite film with uniform dispersion of different-n-value nanoplates forms a symmetric-like band diagram with PEDOT and P3HT transport layers in connection with ITO/PEI and PEI/Ag electrodes under forward and reverse biases. This provides the necessary condition to realize an AC EL in quasi-2D perovskite LEDs. **Figure 6-3b** illustrates the EL spectra recorded at ±1.8 V. We can see that forward and reverse bipolar injection lead to similar EL spectra with the peak position at around 750 nm. The similar EL spectra indicate that the largest-n-value nanoplates function as light-emitting centers under both forward and reverse bipolar injection. Here, our quasi-2D perovskite AC LED shows a high EL performance at both forward and reverse biases with maximal external quantum efficiencies (EQE) of 12.5 % (forward bias) and 3.7 % (reverse bias), as shown in **Figure 6-3c**. More importantly, largely improved operational stability is observed under AC condition, as compared with DC condition. As shown in **Figure 6-3d**, when an AC bias (+2 V/-2 V, 50 Hz) is applied, T_{50} reaches 11 hours. Under DC bias (+2 V/0 V, 50 Hz), T_{50} is reduced to 3.9 hours.

To further confirm the AC-driven quasi-2D perovskite LEDs, the EL output was measured with square-wave AC biases at different frequencies (1 Hz, 20 Hz, 50 Hz and 100 Hz). As shown in **Figure 6-4**. it can be clearly seen that both positive and negative biases can generate an EL output, confirming the AC EL action. It is noted that the EL output is gradually rising but rapidly ceasing when the square-wave voltage is applied and removed. Especially, increasing AC frequency causes a slower EL response, indicating the possibilities that mobile ions are accumulated at perovskite surfaces to facilitate bipolar electron and hole injection under both forward and reverse biases. As shown in perovskite LEECs[182], the ionic motion can cause a band bending on perovskite surfaces to lower injection barriers for electron and hole injection under

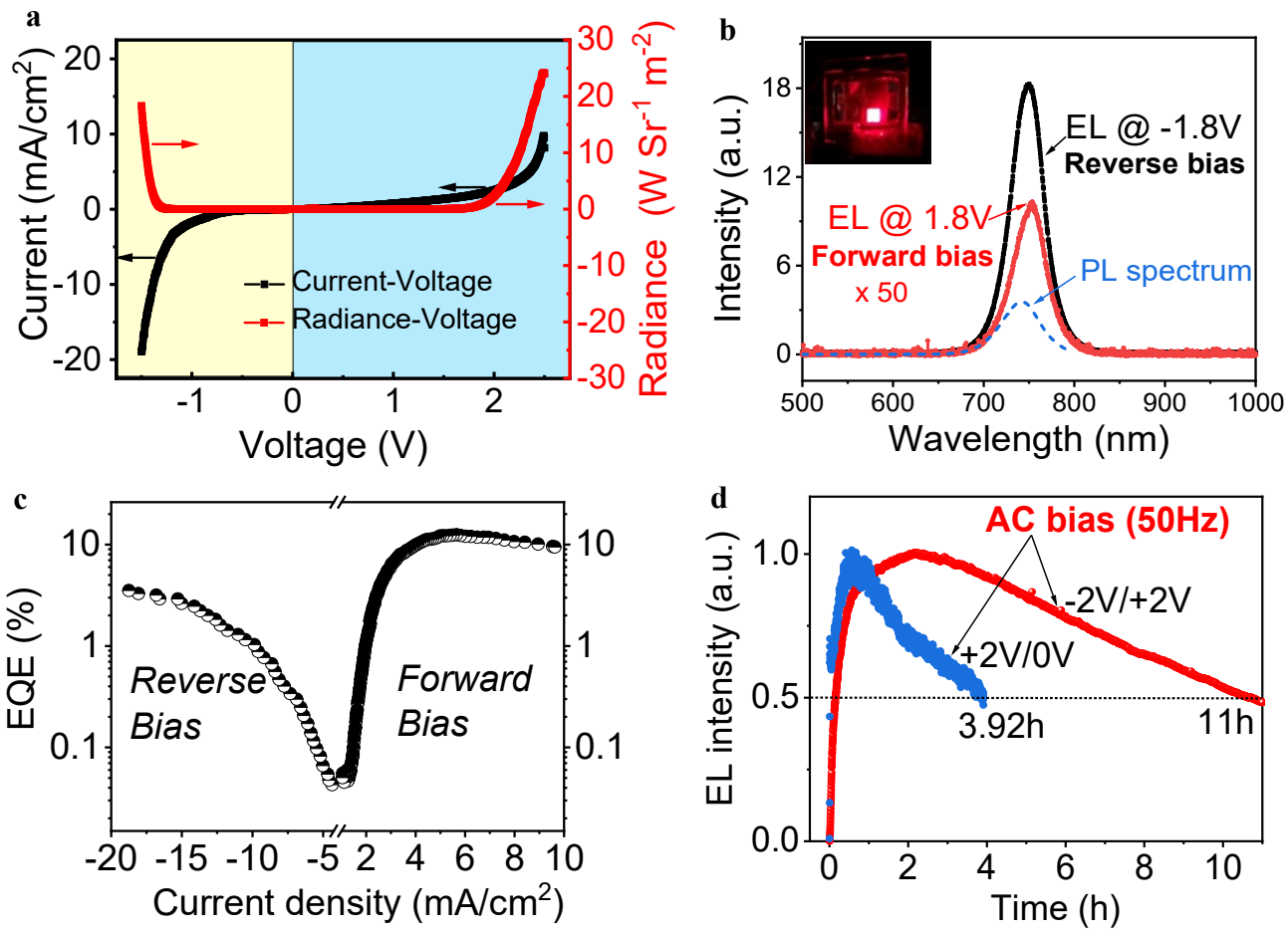


Figure 6- 3 EL Characteristics in quasi-2D perovskite LEDs under forward and reverse biases. (a) Current-voltage-EL characteristics. (b) EL spectra under forward (+1.8 V) and reverse (-1.8 V) biases. Dashed line: PL spectrum. Inset: photograph of device operated under -1.8 V to show strong EL. (c) EQE characteristics at forward and reverse injection currents. (d) Operational stability is shown with T_{50} = 11 hours for AC bias (+2 V/-2 V at 50 Hz, red curve) and T_{50} = 3.9 hours for DC bias (+2 V at 50 Hz, blue curve).

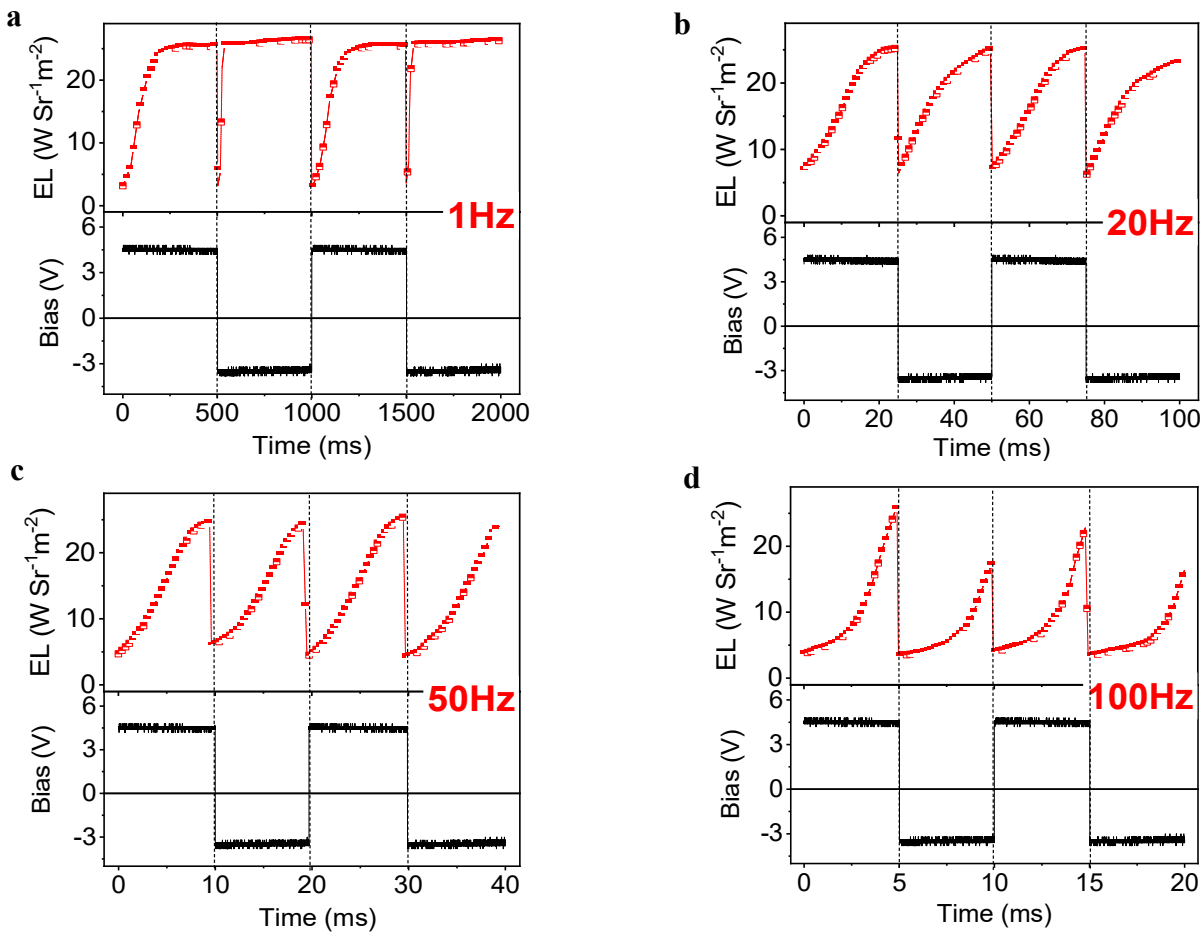


Figure 6- 4 EL profile of quasi-2D perovskite LEDs under forward (4.5V) and reverse (-3.5V) square-wave biases at different frequencies. (a) f = 1 Hz. (b) f = 20 Hz. (c) f = 50 Hz. (d) f = 100 Hz.

both forward and reverse biases, leading to an AC EL. Nonetheless, the EL output profile under positive and negative biases further confirms that the quasi-2D perovskite ($PEA_2MA_{n-1}Pb_nI_{3n+1}$) film of <n> = 5 prepared with the uniform dispersion of different-n-value nanoplates together with the symmetrical device architecture can demonstrate an EL under both forward and reverse biases. In addition, decreasing the thickness of quasi-2D perovskite layer by diluting the precursor solution from 1 M to 0.6 M can lead to more symmetric bipolar (electron and hole) injection under forward and reverse biases. Clearly, our 2D perovskite AC LED is operated based on following three necessary conditions. First, the uniform dispersion of different-n-value nanoplates provides the possibilities to have the lowest-bandgap nanoplates on 2D perovskite surfaces, functioning as reduced potential barriers for electron and hole injection with the capability of allowing bi-directional transport under both forward and reverse biases. Second, the mobile ions can cause a band bending to further lower the injection barriers to inject electrons and holes under an AC bias. Third, the uniformly dispersed different-n-value nanoplates can enhance the "quantum well" effects to confine injected electrons and holes within the lowest-bandgap nanoplates through bi-directional transport to form light-emitting excitons under AC operation.

6.5 Summary

In summary, we have successfully achieved an efficient AC-driven quasi-2D perovskite LED for the first time via uniformly dispersing different-n-value nanoplates together with symmetrical device architecture. Essentially, the uniform dispersion of different-n-value nanoplates provides a mechanism to symmetrically lower the potential barriers for bipolar electron and hole injection and to enable the bidirectional charge transport with charge confinement from small-n-value nanoplates to large-n-value nanoplates towards realizing an AC EL. Furthermore, the injection barriers under both forward and reverse biases were reduced through symmetrical device structure by using PEI as workfunction-modification layer, PEDOT:PSS and P3HT as transport layers. We should point out that our AC quasi-2D perovskite LED shows a high EL performance with the radiance=24 $WSr^{-1}m^{-2}$ and EQE=12.5 % at forward bias and the radiance=18.3 $WSr^{-1}m^{-2}$ and EQE=3.7 % at reverse bias. Moreover, under AC bias (+2 V/-2 V, 50 Hz) condition, the operational stability is reached to T_{50} =11 hours, as compared with the T_{50}=3.9 hours under DC bias (+2 V/0V, 50 Hz). Therefore, we propose a useful strategy to develop AC EL in quasi-2D perovskite LEDs for future commercialization.

Chapter 7 Conclusion

The behaviors of excited states are studied combined with perovskite solar cells and LEDs in this research. The generation, conversion and transport processes are discussed in various perovskite systems, such as 2D, quasi-2D and 3D perovskites. Also, related solar cell or LED efficiencies are optimized through regulating the primary excited states.

First, we found that CTEs can be effectively formed in heterostructured 2D perovskites (PEA_2PbI_4:PEA_2SnI_4), leading to bright broad emission with long PL lifetime of ~ 0.5 μs. By applying our hand-finger pressing method to form PEA_2PbI_4/PEA_2SnI_4 interface, we exclude the possibility of self-trapped exciton emission. We also explore the possible application of CTEs in solar cells by detecting the below-bandgap photocurrent and in LEDs by obtaining electroluminescence through electrical injection. Clearly, the CTEs presents a new mechanism to advance the multifunctionalities in 2D perovskites.

Second, orbit-orbit interaction between excitons have been studied in both 3D Sn based perovskites and quasi-2D perovskites ($PEA_2MA_4Pb_5I_{16}$). Through SnF_2 doping in $FASnI_2Br$ film, the intrinsic orbit-orbit interaction is increased through orbital magnetic dipoles, leading to the photovoltaic efficiency improvement. The enhanced orbit-orbit interaction can be verified by photoexcitation polarization dependent Jsc with +ΔJsc value decreasing from 1.21 % to 0.55 % after doping. This presents a new doping effect occurring in Sn perovskite solar cells towards enhancing photovoltaic efficiency. Besides, a slow cooling of hot carriers is clearly observed within the time window of 200 ps shown in transient absorption (TA) dynamics, leading to long-lived hot carriers in quasi-2D perovskite film ($PEA_2MA_4Pb_5I_{16}$). This slow hot-carrier cooling presents the signature of large polarons occurring in quasi-2D perovskite film by uniformly arranging different-n-value nanoplates. Furthermore, when the slow hot-carrier cooling is occurred, the orbit-orbit interaction is dominated by orbital polarizations, indicating that large polarons can enable a long-order orbital interaction. With the slow hot-carrier cooling and long-order orbital interaction, the quasi-2D perovskite demonstrates superior transport shown by high fill-factor values in solar cell at different carrier densities by varying light illumination intensity. As a consequence, enhancing orbit-orbit interaction presents a new strategy to facilitate dynamical spin conversion of excited states during the development of photovoltaic actions.

Last, the transport of excited states in quasi-2D perovskites is optimized with our proposed vacuum poling treatment method to enforce nucleation during crystallization. This vacuum poling

treatment leads to uniform distribution of different-n-value nanoplates, which is verified through TA measurement and our developed scotch-tape peeling method. With this uniform-distribution, efficient carrier transfer within 10 picoseconds from small-n-value to large-n-value nanoplates are revealed by transient absorption results. Moreover, the record-high fill factor (FF) of 82.4 % with power conversion efficiency (PCE) of 18.04% (Voc =1.223V and Jsc =17.91 mA/cm^2) are demonstrated through efficient carrier extraction. Furthermore, superior stability is achieved with retaining over 96% of their initial efficiency after a storage for 8 months, and maintaining 97.7% at 80 °C for over 180 h. Thus, uniformly arranging different-n-value nanoplates offers a new materials engineering strategy to enhance carrier transfer and extraction for developing high-efficiency and stable quasi-2D perovskite solar cells. Specifically, this efficient charge transfer in our perovskite film results in excellent bipolar carrier transport, which us to achieve high-efficiency AC driven quasi-2D perovskite LEDs. With the device architecture of ITO/PEI/PEDOT:PSS/$PEA_2MA_{n-1}Pb_nI_{3n+1}$/P3HT/PEI/Ag. The high AC EL performance was achieved with the radiance = 24 $WSr^{-1}m^{-2}$ and 18.3 $WSr^{-1}m^{-2}$ and EQE = 12.5% and 3.7% under forward and reverse biases. The device-operational stability was largely improved with the half-intensity time of T_{50} = 11.0 hours under AC bias (+2 V/-2 V, 50 Hz) as compared to T_{50} = 3.9 hours under forward bias (+2 V/0 V, 50 Hz).

In sum, this thesis provides fundamental understanding and future possibilities for perovskite optoelectronic applications.

References

1. Y.-H. Kim, H. Cho, J.H. Heo, T.-S. Kim, N. Myoung, C.-L. Lee, S.H. Im, T.-W. Lee. Multicolored organic/inorganic hybrid perovskite light-emitting diodes. *Advanced Materials*, 2015, **27**, 1248-1254.

2. H.C. Yoon, H. Kang, S. Lee, J.H. Oh, H. Yang, Y.R. Do. Study of perovskite QD down-converted LEDs and six-color white LEDs for future displays with excellent color performance. *ACS Applied Materials & Interfaces*, 2016, **8**, 18189-18200.

3. Y.J. Yoon, K.T. Lee, T.K. Lee, S.H. Kim, Y.S. Shin, B. Walker, S.Y. Park, J. Heo, J. Lee, S.K. Kwak, G.-H. Kim, J.Y. Kim. Reversible, full-color luminescence by post-treatment of perovskite nanocrystals. *Joule*, 2018, **2**, 2105-2116.

4. M.D. Smith, B.A. Connor, H.I. Karunadasa. Tuning the luminescence of layered halide perovskites. *Chemical Reviews*, 2019, **119**, 3104-3139.

5. P. Chen, Y. Bai, M. Lyu, J.-H. Yun, M. Hao, L. Wang. Progress and perspective in low-dimensional metal halide perovskites for optoelectronic applications. *Solar RRL*, 2018, **2**, 1700186.

6. T.C. Sum, S. Chen, G. Xing, X. Liu, B. Wu. Energetics and dynamics in organic–inorganic halide perovskite photovoltaics and light emitters. *Nanotechnology*, 2015, **26**, 342001.

7. X. Yang, Y. Fu, R. Su, Y. Zheng, Y. Zhang, W. Yang, M. Yu, P. Chen, Y. Wang, J. Wu, D. Luo, Y. Tu, L. Zhao, Q. Gong, R. Zhu. Superior carrier lifetimes exceeding 6 μs in polycrystalline halide perovskites. *Advanced Materials*, 2020, **32**, 2002585.

8. S.D. Stranks, G.E. Eperon, G. Grancini, C. Menelaou, M.J.P. Alcocer, T. Leijtens, L.M. Herz, A. Petrozza, H.J. Snaith. Electron-hole diffusion lengths exceeding 1 micrometer in an organometal trihalide perovskite absorber. *Science*, 2013, **342**, 341-344.

9. S. De Wolf, J. Holovsky, S.-J. Moon, P. Löper, B. Niesen, M. Ledinsky, F.-J. Haug, J.-H. Yum, C. Ballif. Organometallic halide perovskites: sharp optical absorption edge and its relation to photovoltaic performance. *The Journal of Physical Chemistry Letters*, 2014, **5**, 1035-1039.

10. W.-J. Yin, T. Shi, Y. Yan. Unique properties of halide perovskites as possible origins of the superior solar cell performance. *Advanced Materials*, 2014, **26**, 4653-4658.

11. T.M. Brenner, D.A. Egger, L. Kronik, G. Hodes, D. Cahen. Hybrid organic—inorganic perovskites: low-cost semiconductors with intriguing charge-transport properties. *Nature Reviews Materials*, 2016, **1**, 1-16.

12. J. Hu, L. Yan, W. You. Two-dimensional organic–inorganic hybrid perovskites: a new platform for optoelectronic applications. *Advanced Materials*, 2018, **30**, 1802041.

13. Y. Chen. Y. Sun, J. Peng, J. Tang, K. Zheng, Z. Liang. 2D Ruddlesden–Popper perovskites for optoelectronics. *Advanced Materials*, 2018, **30**, 1703487.

14. L. Zhao, Y.L. Lin, H. Kim, N.C. Giebink, B.P. Rand. Donor/acceptor charge-transfer states at two-dimensional metal halide perovskite and organic semiconductor interfaces. *ACS Energy Letters*, 2018, **3**, 2708-2712.

15. M. Sarma, K.-T. Wong. Exciplex: an intermolecular charge-transfer approach for TADF. *ACS Applied Materials & Interfaces*, 2018, **10**, 19279-19304.

16. L.J. Rothberg, A.J. Lovinger. Status of and prospects for organic electroluminescence. *Journal of Materials Research*, 1996, **11**, 3174-3187.

17. Y. Wu, B. Hu, J. Howe, A.-P. Li, J. Shen. Spin injection from ferromagnetic Co nanoclusters into organic semiconducting polymers. *Physical Review B*, 2007, **75**, 075413.

18. M.A. Becker, R. Vaxenburg, G. Nedelcu, P.C. Sercel, A. Shabaev, M.J. Mehl, J.G. Michopoulos, S.G. Lambrakos, N. Bernstein, J.L. Lyons, T. Stöferle, R.F. Mahrt, M.V. Kovalenko, D.J. Norris, G. Rainò, A.L. Efros. Bright triplet excitons in caesium lead halide perovskites. *Nature*, 2018, **553**, 189-193.

19. J. Zhang, T. Wu, J. Duan, M. Ahmadi, F. Jiang, Y. Zhou, B. Hu. Exploring spin-orbital coupling effects on photovoltaic actions in Sn and Pb based perovskite solar cells. *Nano Energy*, 2017, **38**, 297-303.

20. Y.-C. Hsiao, T. Wu, M. Li, B. Hu. Magneto-optical studies on spin-dependent charge recombination and dissociation in perovskite solar cells. *Advanced Materials*, 2015, **27**, 2899-2906.

21. J. Even, L. Pedesseau, J.-M. Jancu, C. Katan. Importance of spin–orbit coupling in hybrid organic/inorganic perovskites for photovoltaic applications. *The Journal of Physical Chemistry Letters*, 2013, **4**, 2999-3005.

22. D. Niesner, M. Wilhelm, I. Levchuk, A. Osvet, S. Shrestha, M. Batentschuk, C. Brabec, T. Fauster. Giant Rashba splitting in $CH_3NH_3PbBr_3$ organic-inorganic perovskite. *Physical Review Letters*, 2016, **117**, 126401.

23. F. Zheng, L.Z. Tan, S. Liu, A.M. Rappe. Rashba spin–orbit coupling enhanced carrier lifetime in $CH_3NH_3PbI_3$. *Nano Letters*, 2015, **15**, 7794-7800.

24. A. Stroppa, D. Di Sante, P. Barone, M. Bokdam, G. Kresse, C. Franchini, M.-H. Whangbo, S. Picozzi. Tunable Ferroelectric Polarization and Its Interplay with Spin–orbit Coupling in Tin Iodide Perovskites. *Nature Communications*, 2014, **5**, 5900.

25. M. Li, L. Li, R. Mukherjee, K. Wang, Q. Liu, Q. Zou, H. Xu, J. Tisdale, Z. Gai, I.N. Ivanov, D. Mandrus, B. Hu. Magnetodielectric response from spin–orbital interaction occurring at interface of ferromagnetic Co and organometal halide perovskite layers via Rashba effect. *Advanced Materials*, 2017, **29**, 1603667.

26. M. Wang, H. Zou, J. Zhang, T. Wu, H. Xu, S. Haacke, B. Hu. Extremely long spin lifetime of light-emitting states in quasi-2D perovskites through orbit–orbit interaction. *The Journal of Physical Chemistry Letters*, 2020, **11**, 3647-3652.

27. Z. Yu. Rashba effect and carrier mobility in hybrid organic–inorganic perovskites. *The Journal of Physical Chemistry Letters*, 2016, **7**, 3078-3083.

28. W. Qin, H. Xu, B. Hu. Effects of spin states on photovoltaic actions in organo-metal halide perovskite solar cells based on circularly polarized photoexcitation. *ACS Photonics*, 2017, **4**, 2821-2827.

29. H. Xu, M. Wang, Z. Yu, K. Wang, B. Hu. Magnetic field effects on excited states, charge transport, and electrical polarization in organic semiconductors in spin and orbital regimes. *Advances in Physics*, 2019, **68**, 49-121.

30. C. Motta, F. El-Mellouhi, S. Sanvito. Charge carrier mobility in hybrid halide perovskites. *Scientific Reports*, 2015, **5**, 12746.

31. H. Oga, A. Saeki, Y. Ogomi, S. Hayase, S. Seki. Improved understanding of the electronic and energetic landscapes of perovskite solar cells: high local charge carrier mobility, reduced recombination, and extremely shallow traps. *Journal of the American Chemical Society*, 2014, **136**, 13818-13825.

32. Y. Yu, J. Li, D. Geng, J. Wang, L. Zhang, T.L. Andrew, M.S. Arnold, X. Wang. Development of lead iodide perovskite solar cells using three-dimensional titanium dioxide nanowire architectures. *ACS Nano*, 2015, **9**, 564-572.

33. B.-w. Park, S.I. Seok. Intrinsic instability of inorganic–organic hybrid halide perovskite materials. *Advanced Materials*, 2019, **31**, 1805337.

34. D.W. deQuilettes, K. Frohna, D. Emin, T. Kirchartz, V. Bulovic, D.S. Ginger, S.D. Stranks. Charge-carrier recombination in halide perovskites: focus review. *Chemical Reviews*, 2019, **119**, 11007-11019.

35. M.B. Johnston, L.M. Herz. Hybrid perovskites for photovoltaics: charge-carrier recombination, diffusion, and radiative efficiencies. *Accounts of Chemical Research*, 2016, **49**, 146-154.

36. S.D. Stranks. Nonradiative losses in metal halide perovskites. *ACS Energy Letters*, 2017, **2**, 1515-1525.

37. J.C. Blancon, H. Tsai, W. Nie, C.C. Stoumpos, L. Pedesseau, C. Katan, M. Kepenekian, C.M.M. Soe, K. Appavoo, M.Y. Sfeir, S. Tretiak, P.M. Ajayan, M.G. Kanatzidis, J. Even, J.J. Crochet, A.D. Mohite. Extremely efficient internal exciton dissociation through edge states in layered 2D perovskites. *Science*, 2017, **355**, 1288-1292.

38. Y. Yang, M. Yang, Z. Li, R. Crisp, K. Zhu, M.C. Beard. Comparison of recombination dynamics in $CH_3NH_3PbBr_3$ and $CH_3NH_3PbI_3$ perovskite films: influence of exciton binding energy. *The Journal of Physical Chemistry Letters*, 2015, **6**, 4688-4692.

39. A. Miyata, A. Mitioglu, P. Plochocka, O. Portugall, J.T.-W. Wang, S.D. Stranks, H.J. Snaith, R.J. Nicholas. Direct measurement of the exciton binding energy and effective masses for charge carriers in organic–inorganic tri-halide perovskites. *Nature Physics*, 2015, **11**, 582-587.

40. M.A. Green, A. Ho-Baillie, H.J. Snaith. The emergence of perovskite solar cells. *Nature Photonics*, 2014, **8**, 506-514.

41. J.M. Frost, K.T. Butler, F. Brivio, C.H. Hendon, M. van Schilfgaarde, A. Walsh. Atomistic origins of high-performance in hybrid halide perovskite solar cells. *Nano Letters*, 2014, **14**, 2584-2590.

42. C. Zhao, B. Chen, X. Qiao, L. Luan, K. Lu, B. Hu. Revealing underlying processes involved in light soaking effects and hysteresis phenomena in perovskite solar cells. *Advanced Energy Materials*, 2015, **5**, 1500279.

43. A.M.A. Leguy, J.M. Frost, A.P. McMahon, V.G. Sakai, W. Kockelmann, C. Law, X. Li, F. Foglia, A. Walsh, B.C. O'Regan, J. Nelson, J.T. Cabral, P.R.F. Barnes. The dynamics of methylammonium ions in hybrid organic–inorganic perovskite solar cells. *Nature Communications*, 2015, 6, 7124.

44. D. Giovanni, H. Ma, J. Chua, M. Grätzel, R. Ramesh, S. Mhaisalkar, N. Mathews, T.C. Sum. Highly spin-polarized carrier dynamics and ultralarge photoinduced magnetization in $CH_3NH_3PbI_3$ perovskite thin films. *Nano Letters*, 2015, **15**, 1553-1558.

45. M. Kim, J. Im, A.J. Freeman, J. Ihm, H. Jin. Switchable S= 1/2 and J= 1/2 Rashba bands in ferroelectric halide perovskites. *Proceedings of the National Academy of Sciences*, 2014, **111**, 6900-6904.

46. G. Xing, N. Mathews, S.S. Lim, N. Yantara, X. Liu, D. Sabba, M. Grätzel, S. Mhaisalkar, T.C. Sum. Low-temperature solution-processed wavelength-tunable perovskites for lasing. *Nature Materials*, 2014, **13**, 476-480.

47. D. Liu, T.L. Kelly. Perovskite solar cells with a planar heterojunction structure prepared using room-temperature solution processing techniques. *Nature Photonics*, 2014, **8**, 133-138.

48. O. Malinkiewicz, A. Yella, Y.H. Lee, G.M. Espallargas, M. Graetzel, M.K. Nazeeruddin, H.J. Bolink. Perovskite solar cells employing organic charge-transport layers. *Nature Photonics*, 2014, **8**, 128-132.

49. W. Nie, H. Tsai, R. Asadpour, J.-C. Blancon, A.J. Neukirch, G. Gupta, J.J. Crochet, M. Chhowalla, S. Tretiak, M.A. Alam, H.-L. Wang, A.D. Mohite. High-efficiency solution-processed perovskite solar cells with millimeter-scale grains. *Science*, 2015, **347**, 522-525.

50. D. Bi, W. Tress, M.I. Dar, P. Gao, J. Luo, C. Renevier, K. Schenk, A. Abate, F. Giordano, J.-P. Correa Baena, J.-D. Decoppet, S.M. Zakeeruddin, M.K. Nazeeruddin, M. Grätzel, A. Hagfeldt. Efficient luminescent solar cells based on tailored mixed-cation perovskites. *Science Advances*, 2016, **2**, e1501170.

51. M. Saliba, T. Matsui, K. Domanski, J.-Y. Seo, A. Ummadisingu, S.M. Zakeeruddin, J.-P. Correa-Baena, W.R. Tress, A. Abate, A. Hagfeldt, M. Grätzel. Incorporation of rubidium cations into perovskite solar cells improves photovoltaic performance. *Science*, 2016, **354**, 206-209.

52. H. Tan, A. Jain, O. Voznyy, X. Lan, F.P. García de Arquer, J.Z. Fan, R. Quintero-Bermudez, M. Yuan, B. Zhang, Y. Zhao, F. Fan, P. Li, L.N. Quan, Y. Zhao, Z.-H. Lu, Z. Yang, S. Hoogland, E.H. Sargent. Efficient and stable solution-processed planar perovskite solar cells via contact passivation. *Science*, 2017, **355**, 722-726.

53. K.A. Bush, A.F. Palmstrom, Z.J. Yu, M. Boccard, R. Cheacharoen, J.P. Mailoa, D.P. McMeekin, R.L.Z. Hoye, C.D. Bailie, T. Leijtens, I.M. Peters, M.C. Minichetti, N. Rolston, R. Prasanna, S. Sofia, D. Harwood, W. Ma, F. Moghadam, H.J. Snaith, T. Buonassisi, Z.C. Holman, S.F. Bent, M.D. McGehee. 23.6%-efficient monolithic perovskite/silicon tandem solar cells with improved stability. *Nature Energy*, 2017, **2**, 17009.

54. Q. Jiang, Y. Zhao, X. Zhang, X. Yang, Y. Chen, Z. Chu, Q. Ye, X. Li, Z. Yin, J. You. Surface passivation of perovskite film for efficient solar cells. *Nature Photonics*, 2019, **13**, 460-466.

55. NREL, Efficiency chart: *https://www.nrel.gov/pv/cell-efficiency.html.* (Accessed September 2020).

56. M.H. Kumar, S. Dharani, W.L. Leong, P.P. Boix, R.R. Prabhakar, T. Baikie, C. Shi, H. Ding, R. Ramesh, M. Asta, M. Graetzel, S.G. Mhaisalkar, N. Mathews. Lead-free halide perovskite solar cells with high photocurrents realized through vacancy

modulation. *Advanced Materials*, 2014, **26**, 7122-7127.

57. W. Liao, D. Zhao, Y. Yu, C.R. Grice, C. Wang, A.J. Cimaroli, P. Schulz, W. Meng, K. Zhu, R.G. Xiong, Y. Yan. Lead-free inverted planar formamidinium tin triiodide perovskite solar cells achieving power conversion efficiencies up to 6.22%. *Advanced Materials*, 2016, **28**, 9333-9340.

58. Z. Zhu, C.-C. Chueh, N. Li, C. Mao, A.K.Y. Jen. Realizing efficient lead-free formamidinium tin triiodide perovskite solar cells via a sequential deposition route. *Advanced Materials*, 2018, **30**, 1703800.

59. S.J. Lee, S.S. Shin, Y.C. Kim, D. Kim, T.K. Ahn, J.H. Noh, J. Seo, S.I. Seok. Fabrication of efficient formamidinium tin iodide perovskite solar cells through SnF_2–pyrazine complex. *Journal of the American Chemical Society*, 2016, **138**, 3974-3977.

60. S. Gupta, D. Cahen, G. Hodes. How SnF_2 impacts the material properties of lead-free tin perovskites. *The Journal of Physical Chemistry C*, 2018, **122**, 13926-13936.

61. G. Nasti, A. Abate. Tin halide perovskite ($ASnX_3$) solar cells: a comprehensive guide toward the highest power conversion efficiency. *Advanced Energy Materials*, 2020, **10**, 1902467.

62. C.H. Ng, K. Nishimura, N. Ito, K. Hamada, D. Hirotani, Z. Wang, F. Yang, S. likubo, Q. Shen, K. Yoshino, T. Minemoto, S. Hayase. Role of GeI_2 and SnF_2 additives for SnGe perovskite solar cells. *Nano Energy*, 2019, **58**, 130-137.

63. I.C. Smith, E.T. Hoke, D. Solis-Ibarra, M.D. McGehee, H.I. Karunadasa. A layered hybrid perovskite solar-cell absorber with enhanced moisture stability. *Angewandte Chemie*, 2014, **126**, 11414-11417.

64. G. Grancini, C. Roldán-Carmona, I. Zimmermann, E. Mosconi, X. Lee, D. Martineau, S. Narbey, F. Oswald, F. De Angelis, M. Graetzel, M.K. Nazeeruddin. One-Year stable perovskite solar cells by 2D/3D interface engineering. *Nature Communications*, 2017, **8**, 15684.

65. L.N. Quan, M. Yuan, R. Comin, O. Voznyy, E.M. Beauregard, S. Hoogland, A. Buin, A.R. Kirmani, K. Zhao, A. Amassian, D.H. Kim, E.H. Sargent. Ligand-stabilized reduced-dimensionality perovskites. *Journal of the American Chemical Society*, 2016, **138**, 2649-

2655.

66. H. Tsai, W. Nie, J.-C. Blancon, C.C. Stoumpos, R. Asadpour, B. Harutyunyan, A.J. Neukirch, R. Verduzco, J.J. Crochet, S. Tretiak, L. Pedesseau, J. Even, M.A. Alam, G. Gupta, J. Lou, P.M. Ajayan, M.J. Bedzyk, M.G. Kanatzidis, A.D. Mohite. High-efficiency two-dimensional Ruddlesden–Popper perovskite solar cells. *Nature*, 2016, **536**, 312-316.

67. X. Zhang, G. Wu, S. Yang, W. Fu, Z. Zhang, C. Chen, W. Liu, J. Yan, W. Yang, H. Chen. Vertically oriented 2D layered perovskite solar cells with enhanced efficiency and good stability. *Small*, 2017, **13**, 1700611.

68. R. Quintero-Bermudez, A. Gold-Parker, A.H. Proppe, R. Munir, Z. Yang, S.O. Kelley, A. Amassian, M.F. Toney, E.H. Sargent. Compositional and orientational control in metal halide perovskites of reduced dimensionality. *Nature Materials*, 2018, **17**, 900-907.

69. Y. Cao, N. Wang, H. Tian, J. Guo, Y. Wei, H. Chen, Y. Miao, W. Zou, K. Pan, Y. He, H. Cao, Y. Ke, M. Xu, Y. Wang, M. Yang, K. Du, Z. Fu, D. Kong, D. Dai, Y. Jin, G. Li, H. Li, Q. Peng, J. Wang, W. Huang. Perovskite light-emitting diodes based on spontaneously formed submicrometre-scale structures. *Nature*, 2018, **562**, 249-253.

70. K. Lin, J. Xing, L.N. Quan, F.P.G. de Arquer, X. Gong, J. Lu, L. Xie, W. Zhao, D. Zhang, C. Yan, W. Li, X. Liu, Y. Lu, J. Kirman, E.H. Sargent, Q. Xiong, Z. Wei. Perovskite light-emitting diodes with external quantum efficiency exceeding 20 per cent. *Nature*, 2018, **562**, 245-248.

71. L. Gao, L.N. Quan, F.P. García de Arquer, Y. Zhao, R. Munir, A. Proppe, R. Quintero-Bermudez, C. Zou, Z. Yang, M.I. Saidaminov, O. Voznyy, S. Kinge, Z. Lu, S.O. Kelley, A. Amassian, J. Tang, E.H. Sargent. Efficient near-infrared light-emitting diodes based on quantum dots in layered perovskite. *Nature Photonics*, 2020, **14**, 227-233.

72. H. Wang, F.U. Kosasih, H. Yu, G. Zheng, J. Zhang, G. Pozina, Y. Liu, C. Bao, Z. Hu, X. Liu, L. Kobera, S. Abbrent, J. Brus, Y. Jin, M. Fahlman, R.H. Friend, C. Ducati, X.-K. Liu, F. Gao. Perovskite-molecule composite thin films for efficient and stable light-emitting diodes. *Nature Communications*, 2020, **11**, 891.

73. F. Liu, Y. Zhang, C. Ding, S. Kobayashi, T. Izuishi, N. Nakazawa, T. Toyoda, T. Ohta, S. Hayase, T. Minemoto, K. Yoshino, S. Dai, Q. Shen. Highly luminescent phase-stable

$CsPbI_3$ perovskite quantum dots achieving near 100% absolute photoluminescence quantum yield. *ACS Nano*, 2017, **11**, 10373-10383.

74. A. Dutta, R.K. Behera, P. Pal, S. Baitalik, N. Pradhan. Near-unity photoluminescence quantum efficiency for all $CsPbX_3$ (X= Cl, Br, and I) perovskite nanocrystals: a generic synthesis approach. *Angewandte Chemie*, 2019, **131**, 5608-5612.

75. S. Wang, C. Bi, J. Yuan, L. Zhang, J. Tian. Original core–shell structure of cubic $CsPbBr_3$@ amorphous $CsPbBr_x$ perovskite quantum dots with a high blue photoluminescence quantum yield of over 80%. *ACS Energy Letters*, 2017, **3**, 245-251.

76. D.H. Cao, C.C. Stoumpos, O.K. Farha, J.T. Hupp, M.G. Kanatzidis. 2D homologous perovskites as light-absorbing materials for solar cell applications. *Journal of the American Chemical Society*, 2015, **137**, 7843-7850.

77. X.-K. Liu, W. Xu, S. Bai, Y. Jin, J. Wang, R.H. Friend, F. Gao. Metal halide perovskites for light-emitting diodes. *Nature Materials*, 2021, **20**, 10-21.

78. M. Ahmadi, T. Wu, B. Hu. A review on organic–inorganic halide perovskite photodetectors: device engineering and fundamental physics. *Advanced Materials*, 2017, **29**, 1605242.

79. F.P. García de Arquer, A. Armin, P. Meredith, E.H. Sargent. Solution-processed semiconductors for next-generation photodetectors. *Nature Reviews Materials*, 2017, **2**, 1-17.

80. H. Zhou, Q. Chen, G. Li, S. Luo, T.-b. Song, H.-S. Duan, Z. Hong, J. You, Y. Liu, Y. Yang. Interface engineering of highly efficient perovskite solar cells. *Science*, 2014, **345**, 542-546.

81. N.J. Jeon, J.H. Noh, W.S. Yang, Y.C. Kim, S. Ryu, J. Seo, S.I. Seok. Compositional engineering of perovskite materials for high-performance solar cells. *Nature*, 2015, **517**, 476-480.

82. Z. Li, T.R. Klein, D.H. Kim, M. Yang, J.J. Berry, M.F.A.M. van Hest, K. Zhu. Scalable fabrication of perovskite solar cells. *Nature Review Materials*, 2018, **3**, 18017.

83. S. Bai, P. Da, C. Li, Z. Wang, Z. Yuan, F. Fu, M. Kawecki, X. Liu, N. Sakai, J.T.-W. Wang,

S. Huettner, S. Buecheler, M. Fahlman, F. Gao, H.J. Snaith. Planar perovskite solar cells with long-term stability using ionic liquid additives. *Nature*, 2019, **571**, 245-250.

84. J. Woo Choi, H.C. Woo, X. Huang, W.-G. Jung, B.-J. Kim, S.-W. Jeon, S.-Y. Yim, J.-S. Lee, C.-L. Lee. Organic-inorganic hybrid perovskite quantum dots with high PLQY and enhanced carrier mobility through crystallinity control by solvent engineering and solid-state ligand exchange. *Nanoscale*, 2018, **10**, 13356-13367.

85. Y. Liu, J. Cui, K. Du, H. Tian, Z. He, Q. Zhou, Z. Yang, Y. Deng, D. Chen, X. Zuo, Y. Ren, L. Wang, H. Zhu, B. Zhao, D. Di, J. Wang, R.H. Friend, Y. Jin. Efficient blue light-emitting diodes based on quantum-confined bromide perovskite nanostructures. *Nature Photonics*, 2019, **13**, 760-764.

86. J. Luo, X. Wang, S. Li, J. Liu, Y. Guo, G. Niu, L. Yao, Y. Fu, L. Gao, Q. Dong, C. Zhao, M. Leng, F. Ma, W. Liang, L. Wang, S. Jin, J. Han, L. Zhang, J. Etheridge, J. Wang, Y. Yan, E.H. Sargent, J. Tang. Efficient and stable emission of warm-white light from lead-free halide double perovskites. *Nature*, 2018, **563**, 541-545.

87. K. Tanaka, T. Kondo. Bandgap and exciton binding energies in lead-iodide-based natural quantum-well crystals. *Science and Technology of Advanced Materials*, 2004, **4**, 599-604.

88. K. Galkowski, A. Mitioglu, A. Miyata, P. Plochocka, O. Portugall, G.E. Eperon, J.T.-W. Wang, T. Stergiopoulos, S.D. Stranks, H.J. Snaith, R.J. Nicholas. Determination of the exciton binding energy and effective masses for methylammonium and formamidinium lead tri-halide perovskite semiconductors. *Energy & Environmental Science*, 2016, **9**, 962-970.

89. V. D'Innocenzo, A.R. Srimath Kandada, M. De Bastiani, M. Gandini, A. Petrozza. Tuning the light emission properties by band gap engineering in hybrid lead halide perovskite. *Journal of the American Chemical Society*, 2014, **136**, 17730-17733.

90. Y. Hassan, Y. Song, R.D. Pensack, A.I. Abdelrahman, Y. Kobayashi, M.A. Winnik, G.D. Scholes. Structure-tuned lead halide perovskite nanocrystals. *Advanced Materials*, 2016. **28**, 566-573.

91. M. Yuan, L.N. Quan, R. Comin, G. Walters, R. Sabatini, O. Voznyy, S. Hoogland, Y. Zhao, E.M. Beauregard, P. Kanjanaboos, Z. Lu, D.H. Kim, E.H. Sargent. Perovskite energy funnels for efficient light-emitting diodes. *Nature Nanotechnology*, 2016, **11**, 872-877.

92. H. Cho, S.-H. Jeong, M.-H. Park, Y.-H. Kim, C. Wolf, C.-L. Lee, J.H. Heo, A. Sadhanala, N. Myoung, S. Yoo, S.H. Im, R.H. Friend, T.-W. Lee. Overcoming the electroluminescence efficiency limitations of perovskite light-emitting diodes. *Science*, 2015, **350**, 1222.

93. B. Zhao, S. Bai, V. Kim, R. Lamboll, R. Shivanna, F. Auras, J.M. Richter, L. Yang, L. Dai, M. Alsari, X.-J. She, L. Liang, J. Zhang, S. Lilliu, P. Gao, H.J. Snaith, J. Wang, N.C. Greenham, R.H. Friend, D. Di. High-efficiency perovskite–polymer bulk heterostructure light-emitting diodes. *Nature Photonics*, 2018, **12**, 783-789.

94. X. Yang, X. Zhang, J. Deng, Z. Chu, Q. Jiang, J. Meng, P. Wang, L. Zhang, Z. Yin, J. You. Efficient green light-emitting diodes based on quasi-two-dimensional composition and phase engineered perovskite with surface passivation. *Nature Communications*, 2018, **9**, 570.

95. X.Y. Zhu, Q. Yang, M. Muntwiler. Charge-transfer excitons at organic semiconductor surfaces and interfaces. *Accounts of Chemical Research*, 2009, **42**, 1779-1787.

96. A.E. Jailaubekov, A.P. Willard, J.R. Tritsch, W.-L. Chan, N. Sai, R. Gearba, L.G. Kaake, K.J. Williams, K. Leung, P.J. Rossky, X.Y. Zhu. Hot charge-transfer excitons set the time limit for charge separation at donor/acceptor interfaces in organic photovoltaics. *Nature Materials*, 2013, **12**, 66-73.

97. M. Li, H. Wang, L. He, H. Zang, H. Xu, B. Hu. Optically tunable spin-exchange energy at donor: acceptor interfaces in organic solar cells. *Applied Physics Letters*, 2014, **105**, 023302.

98. L. He, M. Li, A. Urbas, B. Hu. Optically tunable magneto-capacitance phenomenon in organic semiconducting materials developed by electrical polarization of intermolecular charge-transfer states. *Advanced Materials*, 2014, **26**, 3956-3961.

99. G. Dennler, M.C. Scharber, C.J. Brabec. Polymer-fullerene bulk-heterojunction solar cells. *Advanced Materials*, 2009, **21**, 1323-1338.

100. P. Heremans, D. Cheyns, B.P. Rand. Strategies for increasing the efficiency of heterojunction organic solar cells: material selection and device architecture. *Accounts of Chemical Research*, 2009, **42**, 1740-1747.

101. E.A. Chandross, H.T. Thomas. Intramolecular exciplex formation in naphthylalkylamines. *Chemical Physics Letters*, 1971, **9**, 393-396.

102. N. Mataga, M. Hiroshi. Electron transfer and exciplex chemistry. *Advances in Chemical Physics: Electron Transfer—from Isolated Molecules to Biomolecules*, 1999, **107**, 431-496.

103. D.D. Gebler, Y.Z. Wang, J.W. Blatchford, S.W. Jessen, D.K. Fu, T.M. Swager, A.G. MacDiarmid, A.J. Epstein. Exciplex emission in bilayer polymer light-emitting devices. *Applied Physics Letters*, 1997, **70**, 1644-1646.

104. W.-M. Liao, J.-H. Zhang, S.-Y. Yin, H. Lin, X. Zhang, J. Wang, H.-P. Wang, K. Wu, Z. Wang, Y.-N. Fan, M. Pan, C.-Y. Su. Tailoring exciton and excimer emission in an exfoliated ultrathin 2D metal-organic framework. *Nature Communications*, 2018, **9**, 2401.

105. C. Calvino, A. Guha, C. Weder, S. Schrettl. Self-calibrating mechanochromic fluorescent polymers based on encapsulated excimer-forming dyes. *Advanced Materials*, 2018, 30, 1704603.

106. H. Dong, Y. Wei, W. Zhang, C. Wei, C. Zhang, J. Yao, Y.S. Zhao. Broadband tunable microlasers based on controlled intramolecular charge-transfer process in organic supramolecular microcrystals. *Journal of the American Chemical Society*, 2016, **138**, 1118-1121.

107. C. Wei, M. Gao, F. Hu, J. Yao, Y.S. Zhao. Excimer emission in self-assembled organic spherical microstructures: an effective approach to wavelength switchable microlasers. *Advanced Optical Materials*, 2016, **4**, 1009-1014.

108. W. Li, Y. Pan, R. Xiao, Q. Peng, S. Zhang, D. Ma, F. Li, F. Shen, Y. Wang, B. Yang, Y. Ma. Employing~ 100% excitons in OLEDs by utilizing a fluorescent molecule with hybridized local and charge-transfer excited state. *Advanced Functional Materials*, 2014, **24**, 1609-1614.

109. J.W. Verhoeven, H.J. van Ramesdonk, M.M. Groeneveld, A.C. Benniston, A. Harriman. Long-lived charge-transfer states in compact donor–acceptor dyads. *ChemPhysChem*, 2005, **6**, 2251-2260.

110. P.B. Deotare, W. Chang, E. Hontz, D.N. Congreve, L. Shi, P.D. Reusswig, B. Modtland, M.E. Bahlke, C.K. Lee, A.P. Willard, V. Bulović, T. Van Voorhis, M.A. Baldo. Nanoscale transport of charge-transfer states in organic donor–acceptor blends. *Nature Materials*, 2015, **14**, 1130-1134.

111. M.A. Loi, S. Toffanin, M. Muccini, M. Forster, U. Scherf, M. Scharber. Charge transfer excitons in bulk heterojunctions of a polyfluorene copolymer and a fullerene derivative. *Advanced Functional Materials*, 2007, **17**, 2111-2116.

112. S. Bettis Homan, V.K. Sangwan, I. Balla, H. Bergeron, E.A. Weiss, M.C. Hersam. Ultrafast exciton dissociation and long-lived charge separation in a photovoltaic pentacene–MoS_2 van der Waals heterojunction. *Nano Letters*, 2017, **17**, 164-169.

113. K. Wu, Q. Li, Y. Jia, J.R. McBride, Z.X. Xie, T. Lian. Efficient and ultrafast formation of long-lived charge-transfer exciton state in atomically thin cadmium selenide/cadmium telluride type-II heteronanosheets. *ACS Nano*, 2015, **9**, 961-968.

114. T. Yokoyama, D.H. Cao, C.C. Stoumpos, T.-B. Song, Y. Sato, S. Aramaki, M.G. Kanatzidis. Overcoming short-circuit in lead-free $CH_3NH_3SnI_3$ perovskite solar cells via kinetically controlled gas–solid reaction film fabrication process. *The Journal of Physical Chemistry Letters*, 2016, **7**, 776-782.

115. J. Yu, J. Kong, W. Hao, X. Guo, H. He, W.R. Leow, Z. Liu, P. Cai, G. Qian, S. Li, X. Chen, X. Chen. Broadband extrinsic self-trapped exciton emission in Sn-doped 2D lead-halide perovskites. *Advanced Materials*, 2018, **31**, 1806385.

116. T. Hu, M.D. Smith, E.R. Dohner, M.-J. Sher, X. Wu, M.T. Trinh, A. Fisher, J. Corbett, X.Y. Zhu, H.I. Karunadasa, A.M. Lindenberg. Mechanism for broadband white light emission from two-dimensional (110) hybrid perovskites. *The Journal of Physical Chemistry Letters*, 2016, **7**, 2258-2263.

117. X. Li, P. Guo, M. Kepenekian, I. Hadar, C. Katan, J. Even, C.C. Stoumpos, R.D. Schaller, M.G. Kanatzidis. Small cyclic diammonium cation templated (110)-oriented 2D halide (X

= I, Br, Cl) perovskites with white-light emission. *Chemistry of Materials*, 2019, **31**, 3582-3590.

118. M. Abdi-Jalebi, Z. Andaji-Garmaroudi, S. Cacovich, C. Stavrakas, B. Philippe, J.M. Richter, M. Alsari, E.P. Booker, E.M. Hutter, A.J. Pearson, S. Lilliu, T.J. Savenije, H. Rensmo, G. Divitini, C. Ducati, R.H. Friend, S.D. Stranks. Maximizing and Stabilizing Luminescence from Halide Perovskites with Potassium Passivation. *Nature*, 2018, **555**, 497-501.

119. W. Xiang, Z. Wang, D.J. Kubicki, W. Tress, J. Luo, D. Prochowicz, S. Akin, L. Emsley, J. Zhou, G. Dietler, M. Grätzel, A. Hagfeldt. Europium-doped $CsPbI_2Br$ for Stable and Highly Efficient Inorganic Perovskite Solar Cells. *Joule*, 2019, **3**, 205-214.

120. P.C. Harikesh, B. Wu, B. Ghosh, R.A. John, S. Lie, K. Thirumal, L.H. Wong, T.C. Sum, S. Mhaisalkar, N. Mathews. Doping and switchable photovoltaic effect in lead-free perovskites enabled by metal cation transmutation. *Advanced Materials*, 2018, **30**, 1802080.

121. J. Jiang, Q. Wang, Z. Jin, X. Zhang, J. Lei, H. Bin, Z.-G. Zhang, Y. Li, S. Liu. Polymer Doping for High-efficiency perovskite solar cells with improved moisture stability. *Advanced Energy Materials*, 2018, **8**, 1701757.

122. W.-Q. Wu, Q. Wang, Y. Fang, Y. Shao, S. Tang, Y. Deng, H. Lu, Y. Liu, T. Li, Z. Yang, A. Gruverman, J. Huang. Molecular doping enabled scalable blading of efficient hole-transport-layer-free perovskite solar cells. *Nature Communications*, 2018, **9**, 1625.

123. J. Gong, M. Yang, D. Rebollar, J. Rucinski, Z. Liveris, K. Zhu, T. Xu. Divalent anionic doping in perovskite solar cells for enhanced chemical stability. *Advanced Materials*, 2018, **30**, 1800973.

124. F. Wang, X. Jiang, H. Chen, Y. Shang, H. Liu, J. Wei, W. Zhou, H. He, W. Liu, Z. Ning. 2D-Quasi-2D-3D hierarchy structure for tin perovskite solar cells with enhanced efficiency and stability. *Joule*, 2018, **2**, 2732-2743.

125. X. Meng, Y. Wang, J. Lin, X. Liu, X. He, J. Barbaud, T. Wu, T. Noda, X. Yang, L. Han. Surface-controlled oriented growth of $FASnI_3$ crystals for efficient lead-free perovskite solar cells. *Joule*, 2020, **4**, 902-912.

126. M.A. Kamarudin, D. Hirotani, Z. Wang, K. Hamada, K. Nishimura, Q. Shen, T. Toyoda, S. Iikubo, T. Minemoto, K. Yoshino, S. Hayase. Suppression of charge carrier recombination in lead-free tin halide perovskite via lewis base post-treatment. *The Journal of Physical Chemistry Letters*, 2019, **10**, 5277-5283.

127. K. Nishimura, M.A. Kamarudin, D. Hirotani, K. Hamada, Q. Shen, S. Iikubo, T. Minemoto, K. Yoshino, S. Hayase. Lead-free tin-halide perovskite solar cells with 13% efficiency. *Nano Energy*, 2020, **74**, 104858.

128. X. Jiang, F. Wang, Q. Wei, H. Li, Y. Shang, W. Zhou, C. Wang, P. Cheng, Q. Chen, L. Chen, Z. Ning. Ultra-high open-circuit voltage of tin perovskite solar cells via an electron transporting layer design. *Nature Communications*, 2020, **11**, 1245.

129. R.W. Schoenlein, W.Z. Lin, E.P. Ippen, J.G. Fujimoto, Femtosecond hot-carrier energy relaxation in GaAs, *Applied Physics Letters*, 1987, **51**, 1442-1444.

130. A. McClelland, V. Fomenko, E. Borguet, Ultrafast hot-carrier dynamics at chemically modified Ge interfaces probed by SHG, *The Journal of Physical Chemistry B*, 2006, **110**, 19784-19787.

131. C. Zhu, X. Yuan, F. Xiu, C. Zhang, Y. Xu, R. Zhang, Y. Shi, F. Wang, Broadband hot-carrier dynamics in three-dimensional Dirac semimetal Cd_3As_2, *Applied Physics Letters*, 2017, **111**, 091101.

132. D. Niesner, H. Zhu, K. Miyata, P.P. Joshi, T.J. Evans, B.J. Kudisch, M.T. Trinh, M. Marks, X.Y. Zhu, Persistent energetic electrons in methylammonium lead iodide perovskite thin films, *Journal of the American Chemical Society*, 2016, **138**, 15717-15726.

133. P.P. Joshi, S.F. Maehrlein, X. Zhu, Dynamic screening and slow cooling of hot carriers in lead halide perovskites, *Advanced Materials*, 2019, **31**, e1803054.

134. S.D. Verma, Q. Gu, A. Sadhanala, V. Venugopalan, A. Rao, Slow carrier cooling in hybrid Pb–Sn halide perovskites, *ACS Energy Letters*, 2019, **4**, 736-740.

135. M. Bonn, K. Miyata, E. Hendry, X.Y. Zhu, Role of dielectric drag in polaron mobility in lead halide perovskites, *ACS Energy Letters*, 2017, **2**, 2555-2562.

136. K. Miyata, T.L. Atallah, X.Y. Zhu, Lead halide perovskites: crystal-liquid duality, phonon

glass electron crystals, and large polaron formation, *Science Advances*, 2017, **3**, e1701469.

137. M. Li, S. Bhaumik, T.W. Goh, M.S. Kumar, N. Yantara, M. Gratzel, S. Mhaisalkar, N. Mathews, T.C. Sum, Slow cooling and highly efficient extraction of hot carriers in colloidal perovskite nanocrystals, *Nature Communications*, 2017, **8**, 14350.

138. H. Zhu, K. Miyata, Y. Fu, J. Wang, P.P. Joshi, D. Niesner, K.W. Williams, S. Jin, X.Y. Zhu, Screening in crystalline liquids protects energetic carriers in hybrid perovskites, *Science*, 2016, **353**, 1409.

139. K.K. Chauhan, S. Prodhan, D. Ghosh, P. Waghale, S. Bhattacharyya, P.K. Dutta, P.K. Datta, Long carrier diffusion length and slow hot carrier cooling in thin film mixed halide perovskite, *IEEE Journal of Photovoltaics*, 2020, **10**, 803-810.

140. Z. Guo, Y. Wan, M. Yang, J. Snaider, K. Zhu, L. Huang, Long-range hot-carrier transport in hybrid perovskites visualized by ultrafast microscopy, *Science*, 2017, **356**, 59.

141. N.K. Noel, A. Abate, S.D. Stranks, E.S. Parrott, V.M. Burlakov, A. Goriely, H.J. Snaith. Enhanced photoluminescence and solar cell performance via Lewis base passivation of organic–inorganic lead halide perovskites. *ACS Nano*, 2014, **8**, 9815–9821.

142. W. Xu, Q. Hu, S. Bai, C. Bao, Y. Miao, Z. Yuan, T. Borzda, A.J. Barker, E. Tyukalova, Z. Hu, M. Kawecki, H. Wang, Z. Yan, X. Liu, X. Shi, K. Uvdal, M. Fahlman, W. Zhang, M. Duchamp, J.-M. Liu, A. Petrozza, J. Wang, L.-M. Liu, W. Huang, F. Gao. Rational molecular passivation for high-performance perovskite light-emitting diodes. *Nature Photonics*, 2019, **13**, 418-424.

143. D.S. Lee, J.S. Yun, J. Kim, A.M. Soufiani, S. Chen, Y. Cho, X. Deng, J. Seidel, S. Lim, S. Huang, A.W.Y. Ho-Baillie. Passivation of grain boundaries by phenethylammonium in formamidinium-methylammonium lead halide perovskite solar cells. *ACS Energy Letters*, 2018, **3**, 647-654.

144. L. Zhou, Z. Lin, Z. Ning, T. Li, X. Guo, J. Ma, J. Su, C. Zhang, J. Zhang, S. Liu, J. Chang, Y. Hao. Highly efficient and stable planar perovskite solar cells with modulated diffusion passivation toward high power conversion efficiency and ultrahigh fill factor. *Solar RRL*, 2019, **3**, 1900293.

145. J. Zhang, J. Qin, M. Wang, Y. Bai, H. Zou, J.K. Keum, R. Tao, H. Xu, H. Yu, S. Haacke, B.

Hu, Uniform permutation of quasi-2D perovskites by vacuum poling for efficient, high-fill-factor solar cells, *Joule*, 2019, **3**, 3061-3071.

146. J. Zhang, B. Hu, Revealing photoinduced bulk polarization and spin-orbit coupling effects in high-efficiency 2D/3D Pb–Sn alloyed perovskite solar cells, *Nano Energy*, 2020, **76**, 104999.

147. N. Wang, L. Cheng, R. Ge, S. Zhang, Y. Miao, W. Zou, C. Yi, Y. Sun, Y. Cao, R. Yang, Y. Wei, Q. Guo, Y. Ke, M. Yu, Y. Jin, Y. Liu, Q. Ding, D. Di, L. Yang, G. Xing, H. Tian, C. Jin, F. Gao, R.H. Friend, J. Wang, W. Huang. Perovskite light-emitting diodes based on solution-processed self-organized multiple quantum wells. *Nature Photonics*, 2016, **10**, 699-704.

148. Z. Chen, Y. Guo, E. Wertz, J. Shi. Merits and challenges of ruddlesden–popper soft halide perovskites in electro‐optics and optoelectronics. *Advanced Materials*, 2019, **31**, 1803514.

149. A.H. Proppe, R. Quintero-Bermudez, H. Tan, O. Voznyy, S.O. Kelley, E.H. Sargent. Synthetic control over quantum well width distribution and carrier migration in low-dimensional perovskite photovoltaics. *Journal of the American Chemical Society*, 2018, **140**, 2890-2896.

150. J. Liu, J. Leng, K. Wu, J. Zhang, S. Jin. Observation of internal photoinduced electron and hole separation in hybrid two-dimentional perovskite films. *Journal of the American Chemical Society*, 2017, **139**, 1432-1435.

151. Q. Shang, Y. Wang, Y. Zhong, Y. Mi, L. Qin, Y. Zhao, X. Qiu, X. Liu, Q. Zhang. Unveiling structurally engineered carrier dynamics in hybrid quasi-two-dimensional perovskite thin films toward controllable emission. *The Journal of Physical Chemistry Letters*, 2017, **8**, 4431-4438.

152. C.R. Kagan, D.B. Mitzi, C.D. Dimitrakopoulos. Organic-inorganic hybrid materials as semiconducting channels in thin-film field-effect transistors. *Science*, 1999, **286**, 945-947.

153. Y. Chen, Y. Sun, J. Peng, J. Tang, K. Zheng, Z. Liang. 2D Ruddlesden-Popper perovskites for optoelectronics. *Advanced Materials*, 2018, **30**, 1703847-1703862.

154. Z. Xiao, L. Zhao, N.L. Tran, Y.L. Lin, S.H. Silver, R.A. Kerner, N. Yao, A. Kahn, G.D.

Scholes, B.P. Rand. Mixed-halide perovskites with stabilized bandgaps. *Nano Letters*, 2017, **17**, 6863-6869.

155. W. Peng, J. Yin, K.-T. Ho, O. Ouellette, M. De Bastiani, B. Murali, O. El Tall, C. Shen, X. Miao, J. Pan, E. Alarousu, J.-H. He, B.S. Ooi, O.F. Mohammed, E. Sargent, O.M. Bakr. Ultralow self-doping in two-dimensional hybrid perovskite single crystals. *Nano Letters*, 2017, **17**, 4759-4767.

156. J. Qiu, Y. Zheng, Y. Xia, L. Chao, Y. Chen, W. Huang. Rapid crystallization for efficient 2D Ruddlesden–Popper (2DRP) perovskite solar cells. *Advanced Functional Materials*, 2018, **29**, 1806831.

157. C. Xue, Y. Shi, C. Zhang, Y. Lv, Y. Feng, W. Tian, S. Jin, T. Ma. Favorable growth of well-crystallized layered hybrid perovskite by combination of thermal and solvent assistance. *Journal of Power Sources*, 2019, **422**, 156-162.

158. C.M.M. Soe, W. Nie, C.C. Stoumpos, H. Tsai, J.-C. Blancon, F. Liu, J. Even, T.J. Marks, A.D. Mohite, M.G. Kanatzidis. Understanding film formation morphology and orientation in high member 2D Ruddlesden-Popper perovskites for high-efficiency solar cells. *Advanced Energy Materials*, 2018, **8**, 1700979.

159. J. Wang, J. Leng, J. Liu, S. He, Y. Wang, K. Wu, S. Jin. Engineered directional charge flow in mixed two-dimensional perovskites enabled by facile cation-exchange. *The Journal of Physical Chemistry C*, 2017, **121**, 21281-21289.

160. P. Chen, Y. Meng, M. Ahmadi, Q. Peng, C. Gao, L. Xu, M. Shao, Z. Xiong, B. Hu. Charge-transfer versus energy-transfer in quasi-2D perovskite light-emitting diodes. *Nano Energy*, 2018, **50**, 615-622.

161. L.N. Quan, Y. Zhao, F.P. García de Arquer, R. Sabatini, G. Walters, O. Voznyy, R. Comin, Y. Li, J.Z. Fan, H. Tan, J. Pan, M. Yuan, O.M. Bakr, Z. Lu, D.H. Kim, E.H. Sargent. Tailoring the energy landscape in quasi-2D halide perovskites enables efficient green-light emission. *Nano Letters*, 2017, **17**, 3701-3709.

162. R. Yang, R. Li, Y. Cao, Y. Wei, Y. Miao, W.L. Tan, X. Jiao, H. Chen, L. Zhang, Q. Chen, H. Zhang, W. Zou, Y. Wang, M. Yang, C. Yi, N. Wang, F. Gao, C.R. McNeill, T. Qin, J. Wang, W. Huang. Oriented quasi-2D perovskites for high performance optoelectronic

devices. *Advanced Materials*, 2018, **30**, 1804771-1804779.

163. F.X. Xie, D. Zhang, H. Su, X. Ren, K.S. Wong, M. Grätzel, W.C.H. Choy. Vacuum-assisted thermal annealing of $CH_3NH_3PbI_3$ for highly stable and efficient perovskite solar cells. *ACS Nano*, 2015, **9**, 639-646.

164. X. Li, D. Bi, C. Yi, J.-D. Décoppet, J. Luo, S.M. Zakeeruddin, A. Hagfeldt, M. Grätzel. A vacuum flash–assisted solution process for high-efficiency large-area perovskite solar cells. *Science*, 2016, **353**, 58-62.

165. J. Qing, X.-K. Liu, M. Li, F. Liu, Z. Yuan, E. Tiukalova, Z. Yan, M. Duchamp, S. Chen, Y. Wang, S. Bai, J.-M. Liu, H.J. Snaith, C.-S. Lee, T.C. Sum, F. Gao. Aligned and graded type-II Ruddlesden-Popper perovskite films for efficient solar cells. *Advanced Energy Materials*, 2018, **8**, 1800185.

166. H. Lai, B. Kan, T. Liu, N. Zheng, Z. Xie, T. Zhou, X. Wan, X. Zhang, Y. Liu, Y. Chen. Two-dimensional Ruddlesden-Popper perovskite with nanorod-like morphology for solar cells with efficiency exceeding 15. *Journal of the American Chemical Society*, 2018, **140**, 11639-11646.

167. Y. Bai, J. Qin, L. Shi, J. Zhang, M. Wang, Y. Zhan, H. Zou, S. Haacke, X. Hou, J. Zi, B. Hu. Amplified spontaneous emission realized by cogrowing large/small grains with self-passivating defects and aligning transition dipoles. *Advanced Optical Materials*, 2019, **7**, 1900345.

168. J. Qin, J. Zhang, Y. Bai, S. Ma, M. Wang, H. Xu, M. Loyd, Y. Zhan, X. Hou, B. Hu. Enabling self-passivation by attaching small grains on surfaces of large grains toward high-performance perovskite LEDs. *iScience*, 2019, **19**, 378-387.

169. X. Zhang, G. Wu, W. Fu, M. Qin, W. Yang, J. Yan, Z. Zhang, X. Lu, H. Chen. Orientation regulation of phenylethylammonium cation based 2D perovskite solar cell with efficiency higher than 11%. *Advanced Energy Materials*, 2018, **8**, 1702498-1702507.

170. D. Thrithamarassery Gangadharan, Y. Han, A. Dubey, X. Gao, B. Sun, Q. Qiao, R. Izquierdo, D. Ma. Aromatic Alkylammonium spacer cations for efficient two-dimensional perovskite solar cells with enhanced moisture and thermal stability. *Solar RRL*, 2018, **2**, 1700215-1700225.

171. W. Fu, J. Wang, L. Zuo, K. Gao, F. Liu, D.S. Ginger, A.K.Y. Jen. Two-dimensional perovskite solar cells with 14.1% power conversion efficiency and 0.68% external radiative efficiency. *ACS Energy Letters*, 2018, **3**, 2086-2093.

172. B.-E. Cohen, Y. Li, Q. Meng, L. Etgar. Dion-Jacobson two-dimensional perovskite solar cells based on benzene dimethanammonium cation. *Nano Letters*, 2019, **19**, 2588-2597.

173. T. Liu, Y. Jiang, M. Qin, J. Liu, L. Sun, F. Qin, L. Hu, S. Xiong, X. Jiang, F. Jiang, P. Peng, S. Jin, X. Lu, Y. Zhou. Tailoring vertical phase distribution of quasi-two-dimensional perovskite films via surface modification of hole-transporting layer. *Nature Communications*, 2019, **10**, 878.

174. X. Zhang, X. Ren, B. Liu, R. Munir, X. Zhu, D. Yang, J. Li, Y. Liu, D.-M. Smilgies, R. Li, Z. Yang, T. Niu, X. Wang, A. Amassian, K. Zhao, S. Liu. Stable high efficiency two-dimensional perovskite solar cells via cesium doping. *Energy & Environmental Science*, 2017, **10**, 2095-2102.

175. C.W. Tang, S.A. VanSlyke. Organic electroluminescent diodes. *Applied Physics Letters*, 1987, **51**, 913-915.

176. S.T. Lee, Y.M. Wang, X.Y. Hou, C.W. Tang. Interfacial electronic structures in an organic light-emitting diode. *Applied Physics Letters*, 1999, **74**, 670-672.

177. Z. Yang, B. Hu, F.E. Karasz. Polymer electroluminescence using ac or reverse dc biasing. *Macromolecules*, 1995, **28**, 6151-6154.

178. Y.Z. Wang, D.D. Gebler, L.B. Lin, J.W. Blatchford, S.W. Jessen, H.L. Wang, A.J. Epstein. Alternating-current light-emitting devices based on conjugated polymers. *Applied Physics Letters*, 1996, **68**, 894-896.

179. Q. Pei, G. Yu, C. Zhang, Y. Yang, A.J. Heeger. Polymer light-emitting electrochemical cells. *Science*, 1995, **269**, 1086-1088.

180. Q. Pei, Y. Yang, G. Yu, C. Zhang, A.J. Heeger. Polymer light-emitting electrochemical cells: in situ formation of a light-emitting p–n junction. *Journal of the American Chemical Society*, 1996, **118**, 3922-3929.

181. K. Youssef, Y. Li, S. O'Keeffe, L. Li, Q. Pei, Fundamentals of materials selection for light-

emitting electrochemical cells. *Advanced Functional Materials*, 2020, **30**, 1909102.

182. H. Zhang, H. Lin, C. Liang, H. Liu, J. Liang, Y. Zhao, W. Zhang, M. Sun, W. Xiao, H. Li, S. Polizzi, D. Li, F. Zhang, Z. He, W.C.H. Choy, Organic–inorganic perovskite light-emitting electrochemical cells with a large capacitance, *Advanced Functional Materials*, 2015, **25**, 7226-7232.

183. G. Grancini, M.K. Nazeeruddin. Dimensional tailoring of hybrid perovskites for photovoltaics. *Nature Review Materials*, 2019, **4**, 4-22.

184. A.Z. Chen, M. Shiu, J.H. Ma, M.R. Alpert, D. Zhang, B.J. Foley, D.-M. Smilgies, S.-H. Lee, J.J. Choi. Origin of vertical orientation in two-dimensional metal halide perovskites and its effect on photovoltaic performance. *Nature Communications*, 2018, **9**, 1336.

185. S.A. Choulis, Y. Kim, J. Nelson, D.D.C. Bradley, M. Giles, M. Shkunov, I. McCulloch. High ambipolar and balanced carrier mobility in regioregular poly(3-hexylthiophene). *Applied Physics Letters*, 2004, **85**, 3890-3892.

186. X. Wang, X. Zhang, L. Sun, D. Lee, S. Lee, M. Wang, J. Zhao, Y. Shao-Horn, M. Dincă, T. Palacios, K.K. Gleason. High electrical conductivity and carrier mobility in oCVD PEDOT thin films by engineered crystallization and acid treatment. *Science Advances*, 2018, **4**, eaat5780.

187. X. Li, J. Hoffman, W. Ke, M. Chen, H. Tsai, W. Nie, A.D. Mohite, M. Kepenekian, C. Katan, J. Even, M.R. Wasielewski, C.C. Stoumpos, M.G. Kanatzidis, Two-dimensional halide perovskites incorporating straight chain symmetric diammonium ions, $(NH_3C_mH_{2m}NH_3)(CH_3NH_3)_{n-1}Pb_nI_{3n+1}$ (m =4-9; n =1-4). *Journal of the American Chemical Society*, 2018, **140**, 12226-12238.

Appendix

List of Publications

1. **Jia Zhang**, Ting Wu, Jiashun Duan, Mahshid Ahmadi, Fangyuan Jiang, Yinhua Zhou, and Bin Hu. "Exploring spin-orbital coupling effects on photovoltaic actions in Sn and Pb based perovskite solar cells." *Nano energy 38*, 297-303, 2017.
2. **Jia Zhang**, Jiajun Qin, Miaosheng Wang, Yujie Bai, Han Zou, Jong Kahk Keum, Runming Tao et al. "Uniform permutation of quasi-2D perovskites by vacuum poling for efficient, high-fill-factor solar cells." *Joule 3*, 3061-3071, 2019.
3. **Jia Zhang**, Xixiang Zhu, Miaosheng Wang, and Bin Hu. "Establishing charge-transfer excitons in 2D perovskite heterostructures." *Nature communications 11*, 2618, 2020.
4. **Jia Zhang**, Jiajun Qin, Ting Wu, and Bin Hu. "Doping Induced Orbit-orbit Interaction between Excitons while Enhancing Photovoltaic Performance in Tin Perovskite Solar Cells." *The Journal of Physical Chemistry Letters 11*, 6996-7001, 2020.
5. **Jia Zhang**, and Bin Hu. "Revealing photoinduced bulk polarization and spin-orbit coupling effects in high-efficiency 2D/3D Pb–Sn alloyed perovskite solar cells." *Nano Energy 76,* 104999, 2020.
6. **Jia Zhang**, Hsinhan Tsai, Wanyi Nie, and Bin Hu. " Enabling AC electroluminescence in quasi-2D perovskites by uniformly arranging different-n-value nanoplates to allow bidirectional charge transport." *Nano Energy 79*, 105413, 2021.
7. Jiantao Li*, Ting Wu*, **Jia Zhang***, Stefan Haacke, Feng Teng, and Bin Hu. "Exploring Light Polarization Effects of Photovoltaic Actions in Organic-Inorganic Hybrid Perovskites with Asymmetric and Symmetric Unit Structures." *ACS Applied Materials & Interfaces 12*, 38054-38060, 2020.
8. Jiajun Qin, **Jia Zhang**, Yujie Bai, Shengbo Ma, Miaosheng Wang, Hengxing Xu, Matthew Loyd, Yiqiang Zhan, Xiaoyuan Hou, and Bin Hu. "Enabling self-passivation by attaching small grains on surfaces of large grains toward high-performance perovskite LEDs." *iScience 19*, 378-387, 2019.
9. Ting Wu, Liam Collins, **Jia Zhang**, Pei-Ying Lin, Mahshid Ahmadi, Stephen Jesse, and Bin Hu. "Photoinduced bulk polarization and its effects on photovoltaic actions in perovskite solar cells." *ACS nano 11*, 11542-11549, 2017.

10. Miaosheng Wang, Han Zou, **Jia Zhang**, Ting Wu, Hengxing Xu, Stefan Haacke, and Bin Hu. "Extremely Long Spin Lifetime of Light-Emitting States in Quasi-2D Perovskites through Orbit–Orbit Interaction." *The Journal of Physical Chemistry Letters 11*, 3647-3652, 2020.
11. Yixuan Dou, Miaosheng Wang, **Jia Zhang**, Hengxing Xu, and Bin Hu. "Identifying Photoinduced Dipolar Polarization and Orbit–Orbit Interaction between Excitons in Organic–Inorganic Hybrid Perovskites." *Advanced Functional Materials 30*, 2003476, 2020.
12. Yujie Bai, Jiajun Qin, Lei Shi, **Jia Zhang**, Miaosheng Wang, Yiqiang Zhan, Han Zou et al. "Amplified Spontaneous Emission Realized by Cogrowing Large/Small Grains with Self-Passivating Defects and Aligning Transition Dipoles." *Advanced Optical Materials 7*, 1900345, 2019.
13. Xixiang Zhu, Hengxing Xu, Yongtao Liu, **Jia Zhang**, Miaosheng Wang, Ilia N. Ivanov, Olga S. Ovchinnikova, and Bin Hu. "Two-Photon Up-Conversion Photoluminescence Realized through Spatially Extended Gap States in Quasi-2D Perovskite Films." *Advanced Materials 31*, 1901240, 2019.
14. Mahshid Ahmadi, Liam Collins, Alexander Puretzky, **Jia Zhang**, Jong Kahk Keum, Wei Lu, Ilia Ivanov, Sergei V. Kalinin, and Bin Hu. "Exploring anomalous polarization dynamics in organometallic halide perovskites." *Advanced Materials* 30, 1705298, 2018.
15. Yixuan Dou, Hengxing Xu, Yongtao Liu, Miaosheng Wang, **Jia Zhang**, Olga S. Ovchinnikova, and Bin Hu. "Tuning spin-orbit coupling towards enhancing photocurrent in hybrid organic-inorganic perovskites by using mixed organic cations." *Organic Electronics 81*, 105671, 2020.

Vita

Jia Zhang was born in Zhumadian City, Henan Province, China. She received her B.S. in Chemical Engineering and Technology (2015) at East China University of Science and Technology, Shanghai, China. In January 2018, she attended the Department of Materials Science and Engineering at University of Tennessee-Knoxville for his Ph. D degree. Her Ph. D research focuses on device engineering and fundamental physics for perovskite devices, including tin-based halide perovskite solar cells, quasi-2D halide perovskite solar cells, and quasi-2D halide perovskite light emitting devices.